Investigating α-Synuclein Changes in the Olfactory Circuitry and Inflammatory Responses in Mice Nasally Inoculated by a Neurotropic Virus

Karim Zahr Eddin

A thesis submitted to the University of Ottawa in partial fulfillment of the

requirements of the Master of Science degree in Cellular and Molecular Medicine

March 2024

Department of Cellular and Molecular Medicine

Faculty of Medicine

University of Ottawa

Abstract

The importance of the olfactory circuitry in Parkinson disease (PD) is supported by the presence of frequent, prodromal hyposmia and of Lewy inclusion-type pathology (LP) in the olfactory bulb (OB) at an early disease stage. Our team previously published that α-synuclein is highly expressed in the olfactory epithelium (OE) and several groups reported that the protein reduces the impact of bacterial and viral infections. We hypothesized that viral encounters could act as a seeding event that induces changes in α-synuclein metabolism, thereby promoting its aggregation and pathological alterations. In the present study, I sought to investigate the state and modifications of endogenous α-synuclein in C57BL/6 mice nasally inoculated with the Indiana serotype of vesicular stomatitis virus [that expresses green fluorescent protein (VSV-GFP)]. Skull sections of animals at different days post-inoculation (DPIs) were analyzed utilizing immunohistochemical and immunofluorescent microscopy to examine the spatiotemporal progression of VSV-GFP signals and α-synuclein modifications in anterior olfactory structures. Immunoreactivity was quantified to probe for morphological changes in glia. This, to further understand the degree of inflammation and juxtapose it to the viral burden in different regions of the brain. Further, microscopic co-localization studies were carried out to elucidate the nature of α-synuclein distribution during infection, including testing for its aggregation. Immunoblotting of brain homogenates was also employed to gauge any quantitative differences in the total amounts of α-synuclein between mock-treated and virus-infected animals.

I found that mice showed variable, but progressively stronger reactivity for VSV-GFP along the olfactory circuitry with sequential involvement of more caudal brain structures, such as the cerebellum and midbrain. This occurred at different days post-inoculation, with viral titers peaking at day 2 post inoculation (DPI) in the anatomical regions analyzed, and with titer

fluctuation seen at 6DPI. I found a significant increase in glial reactivity in the olfactory epithelium and bulb between days 2 and 10 post-inoculation, peaking at 6DPI for microglia and 10DPI for astrocytes; further, α-synuclein reactivity overlapped partially with viral proteins in some axons of olfactory sensory neurons and synapses of olfactory bulb glomeruli, i.e., at rostral points of entry into the mouse brain. I found pathological modifications of α-synuclein comprising Ser129 phosphorylation and co-labeling with the scaffolding protein p62; further, α-synuclein aggregates could be observed in extra- as well as intracranial neurons at 6DPI, albeit with considerable variability. Affected sites included olfactory sensory neurons in the olfactory epithelium, glomeruli, and juxtaglomerular cells, and in mitral cells of the olfactory bulb. Finally, the amount of endogenously expressed, total α-synuclein was increased in 6DPI mice compared to mock-treated animals.

In summary, singular nasal inoculation with VSV-GFP of adult mice generated a progressive – but variable – infection in the rhinencephalon (and more caudal brain structures), which was accompanied by robust microglial and astrocytic responses. In parallel, this led to the rare formation of murine α-synuclein aggregates within olfactory sensory neurons, alongside positive reactivity for Ser129-phosphorylated-α-synuclein in glomeruli and mitral cells, and the detection of p62 reactivity at 6DPI. Future studies will determine whether these aggregates are transient, whether they have the capacity to grow in size over time within the cell (or are degraded or sloughed off during epithelial renewal), whether they promote neural death at the same site or whether they are propagated to other areas of the brain.

Acknowledgements

I would like to express my heartfelt gratitude to my supervisor, Dr. Michael Schlossmacher, for his unwavering guidance and invaluable support throughout my studies. Your mentorship has been pivotal in my growth, and I truly appreciate your equal dedication to both my personal and this project's success. I would also like to extend my gratitude to my co-supervisor, Dr. John Woulfe, for sharing his unparalleled expertise with me and bringing forth indispensable contributions to the maturation of this project. To Dr. Julianna Tomlinson, a mentor of comparable significance, your highly prized scientific insights and positive outlook since my start helped shape and materialize this project in numerous ways. To Dr. Earl Brown, your repertoire of knowledge on all virology and immunology matters related to this project and willingness to help are genuinely appreciated. I am profoundly thankful for the opportunity to learn from such exceptional mentors; thank you all for the scientist I am today.

To my friends and colleagues at the Schlossmacher lab, thank you for sharing your skills, experiences, and laughs with me; those were instrumental in the success of this project.

To my father and sister, thank you for being a pillar to my success and a source of unfaltering support. To my mother, you always realized potential in me and urged me to become a better version of myself. I attribute all of what I have accomplished thus far to you and your teachings. Thank you for loving me for who I am. I wish I can give you the world.

To the memory of my aunt Rasha and grandmother Nabiha, this work is dedicated to you. You have always shown pride in me, and I will continue to carry you with me in my heart.

To Farah, the early chapters of my journey would not have been the same without your unconditional love and compassion. Thank you for staying true to me through thick and thin.

To Biseh and Hazel, thank you for evermore being a solid emotional support system. Your presence brings pure joy to my heart and never fails to brighten my days.

To myself, for persevering and realizing that all cages are mental; your past self is proud of where you are now.

Thank you to the funders of this work, the Canadian Institute of Health Research (CHIR), Aligning Science Across Parkinson (ASAP), and the Dave and Jill Hogg Family Fellowship under the Parkinson Research Consortium (PRC). Your dedication to supporting us researchers is truly admirable and well appreciated.

Table of Contents

Abbreviations Used in Text

AD	Alzheimer's Disease
CBM	Cerebellum
CE	Cortex
CN-1	Cranial Nerve-1
CNS	Central Nervous System
DA	Dopamine
DLB	Dementia with Lewy Bodies
DRG	Dorsal Root Ganglia
ENS	Enteric Nervous System
ER	Endoplasmic Reticulum
GFP	Green Fluorescent Protein
GL	Glomerular Layer
HB	Hemibrain
HIV	Human Immunodeficiency Virus
HPC	Hippocampus
l-DOPA	Levodopa
IN	Indiana Serotype
LB	Lewy Body
LBD	Lewy Body Disease
LN	Lewy Neurites
LP	Lewy Pathology
MLD_{50}	Median Lethal Dose

NFTs	Neurofibrillary Tangles
NJ	New Jersey Serotype
OB	Olfactory Bulb
OE	Olfactory Epithelium
OSN	Olfactory Sensory Neuron
PD	Parkinson Disease
PCX	Piriform Cortex
PPX	Pramipexole
PRR	Pattern Recognition Receptors
PTMs	Post Translational Modifications
RT	Room Temperature
Th	Thalamus
TH	Tyrosine Hydroxylase
SN	Solitary Nucleus
SNpc	Substantia Nigra Pars Compacta
VSV	Vesicular Stomatitis Virus
WNV	West Nile Virus
WT	Wildtype

List of Tables

List of Figures

Introduction

Parkinson Disease

Parkinson disease (PD) is classified as a neurodegenerative disorder of the central nervous system (CNS) that is both progressive and incurable (Twelves et al., 2003). It is grouped into familial and sporadic forms, both of which are characterized neuropathologically by the degeneration and impairment of brain cells in the *Substantia nigra pars compacta* (SNpc), namely dopaminergic neurons, and the subsequent loss of dopamine (DA) levels – an important messenger used in communication between neurons to facilitate movements, amongst others (Kalia and Lang, 2015). This chemical imbalance causes physical symptoms that generate the typical motor characteristics of PD, such as tremor, rigidity, bradykinesia, and postural instability (Braak et al., 2003).

On the neuropathological level, typical late-onset PD involves the development of Lewy bodies (LBs) and Lewy neurites (LNs) in perikaryal and axoplasm compartments, respectively (Lewy J., 1994; Duda et al., 2000; Del Tredici and Braak., 2000-2013). These pathological hallmarks contain abnormal deposits of α-synuclein protein; a predominantly presynaptic protein that regulates synaptic vesicle trafficking but also happens to be implicated in hematological and innate immune functions (Scherzer et al., PNAS 2008; Maroteaux et al., 1988; Spillantini et al., 1997; Murphy et al., 2000; Burré et al., 2010; Vargas et al., 2014; Logan et al., 2017; Atias et al., 2019). At autopsy, the death of dopaminergic neurons in clinically diagnosed PD cases is associated at a rate of >85 % with aggregates of α-synuclein protein that build up in the brain in areas involved in movement control and cognition; the differential diagnosis of typical PD includes ‘secondary, drug-induced (pseudo) parkinsonism’ and DA-responsive dystonia cases

(Kramer and Schulz-Schaeffer., 2007; Schulz-Schaeffer., 2010; Kalia and Lang, 2015). Whether Lewy-type aggregates cause neural death seen in post-mortem patients is not clear yet, however.

Two decades ago, Braak and colleagues (2003) offered a novel staging theory for PD and prior to that for Alzheimer's disease (AD). In the latter, neurofibrillary tangles (NFTs) comprised of aggregated and hyperphosphorylated tau protein are considered one of two hallmark lesions of the disease (Braak et al., 2003; Bennett et al., 2004). Essentially, cross-sectional microscopy was used to classify the degree of pathology in AD; the authors then extended it to include PD-related pathology as well. There, the classification of two neurodegenerative diseases was grouped into six distinct stages of disease progression in each – summarized in **Table 1** below. This elegant model of staging delineated *post-mortem* applied at once to both the research setting and the in-clinic diagnosis of AD and PD (Braak et al., 2003). This group put forward the ground-breaking notion, at the time, that the neuropathology associated with PD begins when a foreign agent enters the body via the nose or gastrointestinal system and travels from there into the CNS. Consequently, other studies and reports would come out to confirm that the severity of clinically observed symptoms matched the proposed staging and spread of Lewy Pathology (LP), where the Braak model is now recognized to fit 87-90% of all patients (Rietdijk et al., 2017).

Stage 1	medulla oblongata	Lesions in the dorsal IX/X motor nucleus and/or intermediate reticular zone
Stage 2	medulla oblongata and pontine tegmentum	Pathology of stage 1 plus lesions in caudal raphe nuclei, gigantocellular reticular nucleus, and coeruleus–subcoeruleus complex
Stage 3	midbrain	Pathology of stage 2 plus midbrain lesions, in particular in the pars compacta of the substantia nigra
Stage 4	basal prosencephalon and mesocortex	Pathology of stage 3 plus prosencephalic lesions. Cortical involvement is confined to the temporal mesocortex (transentorhinal region) and allocortex (CA2-plexus). The neocortex is unaffected
Stage 5	neocortex	Pathology of stage 4 plus lesions in high order sensory association areas of the neocortex and prefrontal neocortex
Stage 6	neocortex	Pathology of stage 5 plus lesions in first order sensory association areas of the neocortex and premotor areas, occasionally mild changes in primary sensory areas and the primary motor field

Table 1: Stages in the Evolution of PD-related CNS Pathology. Later, stage "0" was added to reflect pathology observed in the olfactory bulb and gut. Classification obtained from (Braak et al., 2003).

A few years after proposing this staging theory, Hawkes et al., (2007) had it updated and introduced the 'dual-hit' hypothesis. Succinctly, they hypothesized that the initial events leading to the development of PD may be environmental in nature - with an emphasis on viral microbes – whereby unknown pathogens (or neurotoxicants) gain access to the brain through the stomach and the nose. Importantly, recent research on two post-mortem datasets of Lewy body disease (LBD) cases at relatively early and mild stages confirmed this, but also offered more insight into the pathological initiation of this process. Borghammer et al., (2022) found that pathology concerning α-synuclein was centered either on the enteric nervous system (ENS) or the olfactory bulb at any given time, and rarely concomitantly. Despite this, the Braak and Del Tredici staging concept (Hawkes et al., 2007) is supported by numerous clinical features and diagnoses that are associated with the sequential progression of LP (Abbott et al., 2001; Abbott et al., 2005; Ross et al., 2005)

To this day, treatment of PD is supportive and aimed at ameliorating motor symptoms in the absence of understanding its underlying cause(s); said therapies include drugs such as levodopa (l-DOPA), pramipexole, and ropinirole (Rizek et al., 2016), as well as neurosurgical

interventions, such as by deep brain stimulation of select targets in the CNS. This makes deciphering the molecular mechanisms by which this disease arises of utmost importance. Consequently, this should enable the development of therapies that can modify the course of the disease. Targeted interventions should account for the role of environmental factors (and their relative risk contribution), mechanisms in initial disease development, and/or its progression (Schlossmacher et al., 2017).

The Epidemiology of Parkinson Disease

Parkinson disease affects three percent of the population worldwide during elder age, making it the second most common neurodegenerative disease with more than 10 million people suffering from PD worldwide and thousands of cases going undetected (Hirsch et al., 2016). While the incidence of PD increases with age, an estimated four percent of people with PD are diagnosed before the age of fifty (Reeve et al., 2014). Gender differences are of particular importance in the emergence of PD, and they translate into a 3:2 ratio of males to females with a more delayed onset in females (Miller et al., 2010). Numerous genetic mutations and risk factors are associated with the emergence of PD, including the formation of free radicals, certain environmental toxins, and oxidative stress (Zhou et al., 2009; Logroscino, G., 2005). Family history is a risk factor for PD and the relative risk in first-degree relatives of PD cases increases by approximately two- to three-fold compared to non-relatives with familial forms of PD accounting for 5%–15% of total cases (Kaur et al., 2019). Furthermore, there are multiple genes of different function whose mutations are linked to PD such as in *SNCA, PRKN, LRRK2*, and *PINK1* (Kaur et al., 2019). This essentially points to the multifactorial nature of PD where genetic effects converge with environmental effects and contribute to the development of the disease. This interplay between nature and nurture factors resulted in shedding more light on

prodromal symptoms, including olfactory dysfunction, anxiety, constipation, mood disorders, and REM-sleep behaviour disorder (Grosch et al., 2016). In monogenetic, recessive forms of PD, olfactory dysfunction is rarely observed in mutant gene carriers; it is also less frequently present in those that exhibit the motor phenotype in the context of a *LRRK2* mutation. Nevertheless, olfactory dysfunction could be dependent on other co-factors, which are not only genetic in nature, but also on a history of infections or neurotoxicant exposure (Doty, RL., 2013*)*.

α-Synuclein: An Overview

α-Synuclein is a small 14-15 kDa protein that is variably expressed in the body but is predominantly found in neuronal tissue (Alderson and Markley., 2013). It was initially thought to be solely in the form of free monomers in its natural state, forming α-helices in order to bind lipid membranes (Stefanis, 2012). Interestingly, emerging evidence suggests that α-synuclein occurs in the cytosol of neurons and non-neuronal cells in substantial part as metastable tetramers and related oligomers (Selkoe et al., 2014). In humans, this widely conserved protein is encoded by the *SNCA* gene and is crucial for the regulation of synaptic vesicle trafficking and the release of inter-synaptic neurotransmitters (Maroteaux et al., 1988; Murphy et al., 2000; Burré et al., 2010; Stefanis, 2012; Vargas et al., 2014; Logan et al., 2017; Atias et al., 2019). While α-synuclein is mainly found in brain regions involved in regulating movement, it can also be found in smaller amounts in other parts of the body such as the gut and muscles (Baltic et al., 2004). The abundant presence of α-synuclein in presynaptic terminals of neurons, especially in the adult cortex (CE), hippocampus (HPC) and cerebellum (CBM), assists with the release of neurotransmitters (Meade et al., 2019). Recent evidence suggests that *SNCA* has a neuroprotective effect by limiting the impact of several apoptosis-inducing stimuli and pathways and thus promoting host survival including in the context of select microbial infections

(Tomlinson et al., 2017; Meade et al., 2019). Structurally, α-synuclein is a soluble, tetramerically arranged protein that naturally resists aggregation; however, in pathological conditions (i.e., PD), α-synuclein aggregates to form insoluble fibrils, which drive the formation of LBs in the cytoplasm that displace other cell components (Outeiro et al., 2019). Under normal conditions, the equilibrium between unfolded and helically folded tetramers of α-synuclein is maintained. The reduction in the tetramer-to-monomer ratio and the increase in the level of unfolded α-synuclein monomers favor its aggregation (Selkoe et al., 2014; Gómez-Benito et al., 2020). This pathological event is considered key in the progression of PD as aggregates are postulated to constitute the mechanical basis of neuronal degeneration seen in the development of this disease (Grosch et al., 2016).

α-Synuclein in the Context of Parkinson Disease and Inflammation

Since Parkinson disease is characterized by the loss of DA neurons and the formation of LBs and LNs comprised mainly of abnormally folded and phosphorylated *α*-synuclein, the aggregation of α-synuclein – which could be attributed to *SNCA* gene mutations in the monogenic and rare familial forms of this disease – is linked to the dysfunction and degeneration of neurons in PD (Visanji et al., 2019; Henderson et al., 2019). Moreover, the development of the LBs in different parts of the brain is believed to be correlated with the appearance of non-motor symptoms in people with PD in early stages of the disease, such as hyposmia and constipation, where α-synuclein inclusions were seen in the olfactory bulb and the gut, respectively (Henderson et al., 2019; Braak et al., 2004). The p.A53T mutation, for instance, is associated with early onset PD due to its effect on the half-life of α-synuclein (Tan and Skipper, 2007), its rate of aggregation, and possibly lesser ability for tetramer formation. On the other hand, the p.E46K mutation was found to cause severe parkinsonism with a large number of LBs.

Interestingly, both these mutations, along with other known point mutations, such as p.H50Q and p.G51D, alter α-synuclein structure, which facilitates its aggregation (Tan and Skipper, 2007). One of the major pathological hallmarks of PD is thought to be the serine 129 residue phosphorylation of the α-synuclein molecule (Tan and Skipper, 2007; Stefanis, 2012). A recent study reported that 90% of α-synuclein is phosphorylated in the brain of patients with PD while only 4% of α-synuclein is phosphorylated in healthy brains (Oueslati, 2016). Over the past few years, there have been controversial theories as to whether this phosphorylation event initiates the aggregation of α-synuclein or merely marks toxic variants of α-synuclein for degradation via lysosomal autophagy pathways**,** but recent evidence suggests that this event only regulates the degradation of α-synuclein (Oueslati, 2016). To this date, the etiology of synucleinopathies and what triggers their abnormal aggregation in the context of PD and other neurodegenerative diseases remain not entirely understood (Visanji et al., 2019). It has been hypothesized that a selective vulnerability of certain neuronal populations to infection and subsequent inflammation could contribute to the propagation of α-synuclein; however, it is unclear whether the aggregation and accumulation of α-synuclein is a cause or a consequence of inflammation (Visanji et al., 2019).

Recent studies propose a positive feedback loop between α-synuclein accumulation and inflammation, where the latter is detected by the activation of microglia (Masliah et al., 2000; Spencer et al., 2017; Olanow et al., 2019). It is thought that certain toxic cytokines are released during inflammation, which induce the misfolding of α-synuclein and allows for its aggregation (Olanow et al., 2019). This points to the interplay and overlap between these two phenomena which play key roles in the pathogenesis of PD. In other words, the extent to which the immune system reacts and its efficiency in clearing an infection are both important factors in the

modulation of α-synuclein-pathology spreading observed in PD as was recently proposed by Earls et al., (2020). Furthermore, it has been shown, including by the Schlossmacher lab, that α-synuclein plays a role in innate host defence to modify the outcome of infections (Beatman et al., 2016; Tomlinson et al., 2017). This was based on the finding that *Snca*-null mice were more vulnerable to lethal outcomes of a viral encephalitis as opposed to wildtype (WT) littermates (Beatman et al., 2016; Tomlinson et al., 2017); conversely, endogenous WT α-synuclein lowered the viral titers measured in the brains of infected mice, limited viral growth, and modulated subsequent neuronal injury measured by caspase-3 activity when compared to their *Snca*-KO counterparts (Beatman et al., 2016). Not only was the expression of α-synuclein shown to increase in cultured primary mouse striatal neurons when infected with WNV ((West Nile Virus; a neurotropic, single stranded human pathogen RNA virus that is the causative agent of West Nile fever and encephalitis (Colpitts et al., 2012)), but it was also reported to co-localize with viral particles in the perinuclear space and alter endoplasmic reticulum (ER)-stress signaling, which has been known to be involved in the pathogenesis of various diseases, particularly neurodegenerative disorders such as PD (Beatman et al., 2016).

Furthermore, strains of highly pathogenic H5N1 and H1N1 influenza A viruses were reported to cause neuroinflammation in the brain and neuronal injury *in vivo*, leading to the loss of dopaminergic neurons in the SNpc, motor deficits and α-synuclein aggregation in the midbrain (Jang et al., 2009). Aggregates of α-synuclein were also seen in human mesencephalic cells and immunodeficient mice when infected with the H1N1 influenza A virus (Rita et al., 2020). These viruses are known to disrupt selective cellular homeostasis and proteostasis mechanisms, such as the autophagosome formation and ER signaling, which ultimately induces the formation of clumps of misfolded neurodegeneration-related proteins, including α-synuclein,

which, in turn, initiates a pattern of spreading out in a prion-like fashion (Marques et al., 2019; Rita et al., 2020). Of interest, and relevant to research in the Schlossmacher lab, both of the aforementioned RNA viruses were delivered through a nasal inoculation (i.n.) at a predetermined LD_{50}, where pathogens are both inhaled and swallowed. Staining with specific anti-viral antibodies enabled the authors to visualize the viral spread within different structures in a spatiotemporal manner post inoculation (Jang et al., 2009; Rita et al., 2020). Interestingly, although these viruses are affecting mostly peripheral organs and exert their main effects in the respiratory system, the travel of these viruses from the periphery to the CNS and higher levels of the neuroaxis was shown to occur through the ENS and the dorsal root ganglia (DRG); in the former scenario viral particles were transported via innervation by the vagus nerve to the brainstem's solitary nucleus (SN) and through olfactory nerve axons from the nasal cavity to the olfactory bulb (Tulisiak et al., 2019). Compellingly, this is a route consistent with the stereotypical fashion of LP expansion in PD suggested by Braak and colleagues almost two decades ago (Braak et al., 2003). The work that has been done thus far to describe the transport and the entry routes of Influenza A viruses into the CNS by the two teams shed more light on the presence of neurodegeneration-linked phenotypes, such as related to α-synuclein (Jang et al., 2009; Rita et al., 2020). This body of work illustrated how infections – such as those caused by RNA viruses – may be triggers of α-synuclein dysregulation, as initiated at the host's epithelial point of entry (Tulisiak et al., 2019).

α-Synuclein Displays Some AMP Properties

Recent discoveries have shed light on the protective effect of endogenous α-synuclein in brain-penetrant viral infections, such as HSV, WNV, and reovirus, serotype-3 Dearing (T3D) (Bu et al., 2015; Beatman et al., 2016; Tomlinson et al., 2017), along with the heightened

expression of α-synuclein in response to an infection (Beatman et al., 2016). Abundant expression of this protein in both humans and rodents has been shown at both the presynaptic and nuclear locations (Schasser et al., 2019), along with its ability of modulating virus-induced stress signaling (Beatman et al., 2016). It was hypothesized whether α-synuclein possesses anti-microbial peptide properties (AMP) and is part of the first line of defence against pathogens (Tulisiak et al., 2019). This concept is supported by the fact that α-synuclein has the potential to aggregate and form oligomeric and fibrillar species under certain conditions (genetic predisposition, metabolic perturbations, cellular aging, etc.) leading to a proteinopathy, including certain forms of amyloidosis, which is a feature of proteins acting as natural AMPs (Wilhelm et al., 2014; Moir et al., 2018). This particularly makes sense in the CNS, where the immune response is limited in terms of its adaptive properties, and the innate immune response is critical in combating infections caused by bacterial, viral or fungus assaults (Ransohoff and Brown., 2012).

It is generally agreed that AMPs have a wide range of inhibitory effects against pathogens and exert their anti-pathogenic and immunomodulatory effects by disrupting the host's membrane and affecting the viral trafficking within cells (Park et al., 2016). AMPs, in the broad sense, have also been reported to be modulators of T-cells, macrophage and dendritic cells recruitment to sites of infection, wound healers and angiogenesis aiders, differentiators of dendritic cells, inductors of the production of pro-inflammatory cytokines by macrophages, mast cells, and keratinocytes, and regulators of cell death pathways (Diamond et al., 2009). To date, it remains unclear whether α-synuclein functions in any – or in a combination– of these mechanisms to mitigate infection.

Activated Microglia and the Promotion of α-Synuclein Pathology

As briefly demonstrated in previous sections, the misfolding of α-synuclein and the sequalae of events leading to its pathogenic aggregation has been the topic of study for many. One of the postulated mechanisms for its aggregation is linked to microglial activation (Bassil et al., 2016; Sampson et al., 2016; Wang et al., 2016). The general consensus amongst those studies is that the different cytokines released from microglia upon activation in inflammation initiates the misfolding of neurodegenerative-implicated proteins, with α-synuclein being one of them (Allen Reish and Standaert, 2015; Su and Zhou, 2021). Of relevance in this context, several investigators have explored whether WT α-synuclein, or metabolites and/or aggregates of it, could promote transsynaptic pathology, as informed by neuropathological studies of PD patients who had received intra-striatal transplants of human fetal DA cells (Freed et al., 2001; Olanow et al., 2003). Interestingly, Lewy pathology was discovered in the cell bodies and axoplasm of transplanted neurons of these PD patients, but only after >14 years post transplantation (Kordower et al., 2008a; Li et al., 2008). Subsequent years of research have further added to the concept of a "prion-like nature of misfolded α-synuclein" (Olanow and Brundin, 2013), which was hypothesized as the mechanism by which the aggregated and abnormal α-synuclein is spreading from the diseased brain regions of patients into the healthy and newly transplanted dopaminergic neuronal population. Importantly, no pathological staining of α-synuclein (and associated microglial reactivity) was observed at earlier time-points, as typical pathology was only evident >14-16 years post transplantation; there, it had characteristic LB staining similar to what was seen from the SNpc of the same patients (Olanow et al., 2019). These findings raised the issue that the gradual increase of α-synuclein pathology in transplant recipients may have been linked to a prionoid spread of misfolded protein and to chronic inflammation, as indicated by characteristic activated microglia and consequent cytokine changes (Makaetova-Ladinska et

al., 2000; Masliah et al., 2000; Olanow et al., 2019). An alternative interpretation is that over the course of >14 years, an unknown mechanism promoting PD pathology – other thancell-to-cell spreading of misfolded α-synuclein from host cells itself – caused LP formation in grafted cells.

Post-translational Modifications in α-Synuclein: Physiological or a Synucleinopathy?

While Oueslati (2016) in a previous review compiled evidence suggesting that the post-translational modification of phosphorylation of α-synuclein at Serine129 plays a critical role in the pathological assembly of the normal protein, LB formation, and neuronal degeneration, two recent studies offered great insight into this phenomenon and claimed that the phosphorylation event is a neurotransmitter modulator; in other words, neuronal activity triggers the phosphorylation of α-synuclein at Serine129 (Parra-Rivas et al., 2022; Ramalingam et al., 2023). For so long, it has been thought that phosphorylated α-synuclein is a viable and reliable marker to detect synucleinopathy, based on the notion, but also the undeniable fact, that p-S129syn was found in the intraneuronal assemblies, termed LBs, in synucleinopathies and constituted their major component, akin to p-tau and other misfolded proteins in other disorders (Fujiwara et al., 2002; Anderson et al., 2006; Oueslati et al., 2010).

There has also been some controversy over the years on whether the phosphorylation of α-synuclein is in essence neurotoxic, stemming from the observation that it is always detected in assemblies of LBs and LNs, constituting a consistent pathological feature in post-mortem brains of patients with PD and dementia with Lewy bodies (DLB) (Fujiwara et al., 2002; Anderson et al., 2006; Oueslati et al., 2010). Despite that, more and more research has been providing tangible evidence that phosphorylation of α-synuclein could be in fact a protective mechanism deployed by the neuronal milieu to sequester the toxicity of misfolded and aggregated α-synuclein (Jankowsky et al., 2005; Lee et al., 2011; Ghanem et al., 2022). Furthermore, Parra-

Rivas (2022) and Ramalingam (2023) have aided in partially settling the debate in regard to α-synuclein being entirely cyto- and neurotoxic and mainly being found in LBs of degenerating neurons. In fact, and despite the general scarcity of decent p-synuclein antibodies that are highly specific and yield consistent and reproducible results with little-to-no background staining, especially when working with endogenous α-synuclein in rodents (Delic et al., 2019; Lashuel et al., 2022), the authors were able to reach one very similar and critical finding: p-S129syn seemed to be positively correlated with synaptic plasticity in mice living in an enriched environment, but also in cultured hippocampal and cortical neurons, where action potentials appeared to boost p-S129syn signal (Ramalingam et al., 2023). On the other hand, Parra-Rivas (2022) demonstrated how presynaptic p-S129syn stabilized the C-terminus of normal α-synuclein, allowing it to bind vesicles across the synaptic cleft and thus boost neuronal activity.

Furthermore, the ubiquitin-proteasomal-system (UPS) and autophagy-lysosomal pathways have been shown to be involved in the homeostasis and degradation of abnormal of α-synuclein, which constitutes the rationale of looking into clearance of this protein using markers for both systems, such as p62 that is involved in the UPS pathway (Webb et al., 2003; Pan et al., 2008; Ebrahimi-Fakhari et alk., 2011).The relationship between α-synuclein and p62 (also known as sequestosome-1 or SQSTM1) is significant in the context of PD and other synucleinopathies; p62 is a multifunctional protein that plays a crucial role in cellular quality control processes, including autophagy and the clearance of protein aggregates (Liu et al., 2016). Briefly, the p62 cargo protein has been shown to interact with α-synuclein, and this interaction is believed to contribute to the formation and clearance of α-synuclein aggregates (Watanabe et al., 2012). This interaction is borne when p62 binds to α-synuclein and targets it for degradation through the autophagy-lysosome pathway, which is responsible for removing damaged or

misfolded proteins and cellular components. Dysfunction in this clearance process can lead to the accumulation of α-synuclein aggregates, a hallmark of synucleinopathies like PD (Watanabe et al., 2012). Thus, and since p62 acts as a bridge between α-synuclein aggregates and the autophagy-lysosome system, facilitating the clearance of these toxic protein accumulations, the readout of p62 activity in relation to α-synuclein and infection has gained importance in experimental disease modeling.

Vesicular Stomatitis Virus (VSV) as an Infectious Neurotropic Pathogen

VSV is a prototypic, non-segmented negative sense RNA virus (order mononegavirales, family rhabdoviridae) that comprises five gene products encoded by the 11-kb VSV genome: nucleocapsid protein (N), phosphoprotein (P), matrix protein (M), glycoprotein (G), and large polymerase (L) (Walker et al., 2016). All 5 gene proteins assemble to create an enveloped, bullet-shaped virion that measures approximately 185 nm × 75 nm (Ge et al., 2010; Hastie et al., 2014). VSV's broad cell tropism, relative independence on cell cycle, rapid replication, high virus yields, and small, easily manipulated genome make it a popular model virus for many basic research applications (Bukreyev et al., 2006; Hastie et al., 2014). VSV has two major serotypes: Indiana (IN) and New Jersey (NJ), both of which possess neurotropic features (Hansen et al., 1985; Drolet et al., 2005). The IN serotype is the one used for the purposes of this project as well as all previous work in the Schlossmacher lab involving VSV leading to this project.

Studies generally focus on the nasal injection of VSV into rodents due mainly to VSV's ability to cause experimental encephalitis, but also because directly injecting it into the thalamus (Th) or cerebellum (CBM) is fatal in mice (Johnson et al., 2007; Detje et al., 2009). In C57BL/6J mice, VSV is capable of infecting the OE and spreading into deeper brain structures, hijacking olfactory sensory neurons (OSNs), their axons, and bundles of cranial nerve 1 (CN-1) traversing

through the OE (Huneycutt et al., 1994) giving rise to a moderate to severe and, in some cases, lethal encephalitis, rendering mice in a moribund state (i.e., humane endpoint). VSV tropism is greatly determined by cellular innate antiviral responses, especially those associated with the type I interferon (IFN-α and IFN-β) signaling; VSV can be detected by both cell surface and endosomal pattern recognition receptors (PRR) (Georgel et al., 2007). Interestingly, different cell types were shown to differentially express various components of this type 1 interferon pathway, which may affect their susceptibility to VSV infection (Oritani et al., 2001; Hardy et al., 2004; Hastie et al., 2014).

Importantly in this context and relevant to our project, the recorded behaviour of VSV as a neurotropic virus makes it a suitable experimental tool not only to look at its direct effects in terms of inflammation and downstream modulations of α-synuclein in the olfactory circuitry – one of two main initiation spots for observed pathology in PD – but also because it matches the suggested disease progression stages proposed by Hawkes et al. (2007) in their dual-hit hypothesis, i.e., initiation in the olfactory epithelium, olfactory bulb, enteric and vagus nerves and spreading in a temporal fashion into connected regions of the brain (Huneycutt et al., 1994).

Rationale and Hypothesis

Our research focuses on testing the Hawkes et al idea that an RNA virus-induced infection leading to encephalitis promotes the initiation of PD-like pathology, both at important sites in the brain that are known to show neuropathology in post-mortem PD tissue, such as the olfactory bulb, and with post-translational modifications of α-synuclein that are typically seen in synucleinopathies, such as PD. The Schlossmacher team has published that α-synuclein is highly expressed in the neurons within the olfactory epithelium and that α-synuclein helps to protect mice from nasally acquired viral infections (Tomlinson et al., 2017).

Therefore, I **hypothesized** that microbial encounters, specifically viral infections, can act as seeding events that induce changes in α-synuclein metabolism (such as from steady-state alterations to posttranslational modifications), leading to changes in its functions and, by extension, accumulation of oligomeric, pre-amyloid species. Further, this spread of a disease process involves inflammation and neural injury from the nasal epithelium along the olfactory circuitry and onward into deeper regions of the brain.

To test it, this project had three different, complementary *objectives*:

- To track the progression and infiltration of VSV-GFP from the most rostral olfactory structures into diverse brain regions and to assess the viral burden in distinct anatomical regions of infected animals.
- To capture concurrent neuroinflammatory changes, as caused by VSV-GFP invasion (or signaling thereof), starting in the olfactory epithelium along the olfactory tract into deeper brain regions. This, to quantify the extent of pathology in mice, as indicated by key morphological and phenotypical changes of glia.
- To study the possible link between VSV-GFP infection and induced α-synuclein pathological alterations, as monitored by post-translational modifications and changes in α-synuclein expression levels, by utilizing immunochemical and biochemical techniques, in virally infected animals versus mock-treated littermates.

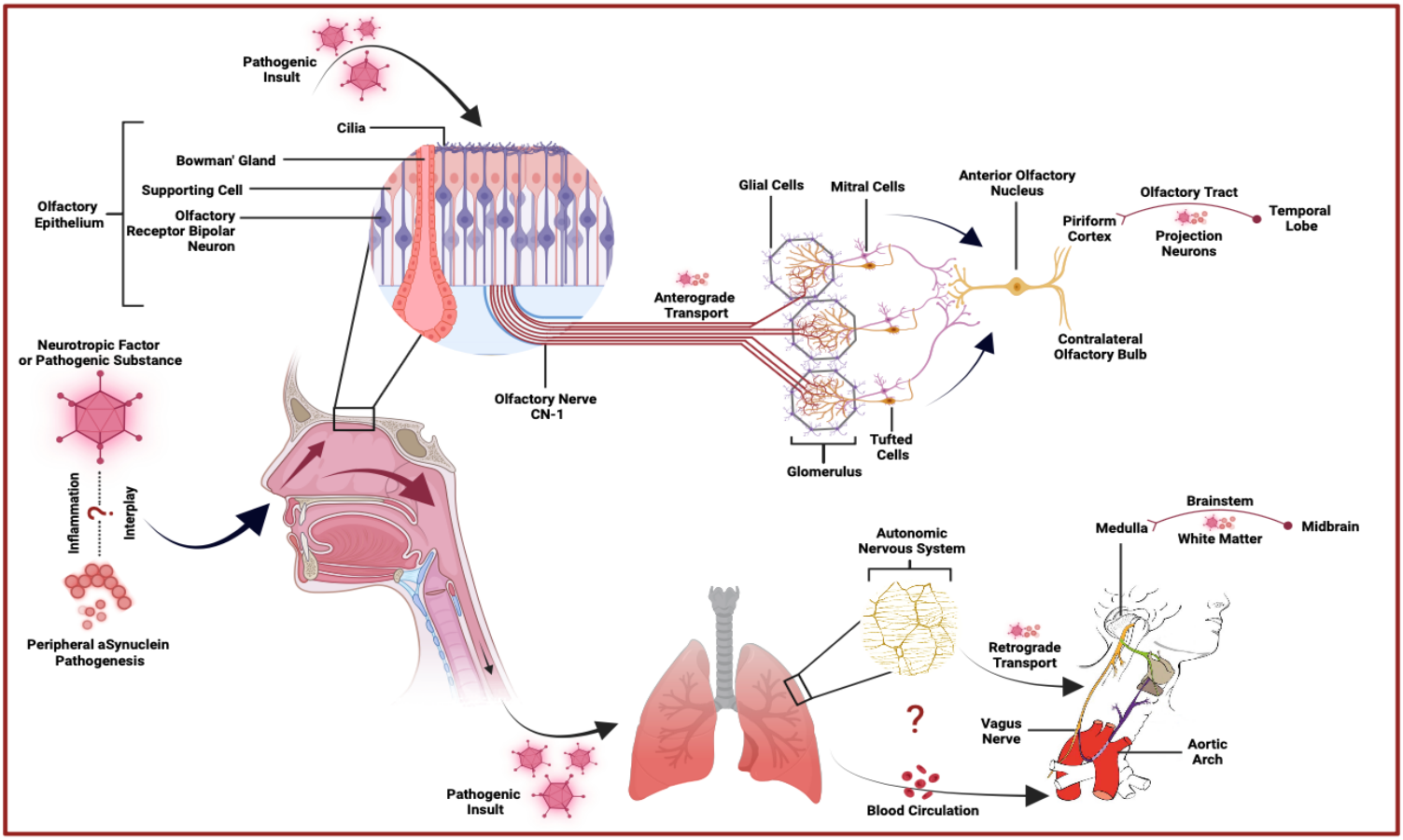

Figure 1: Routes of Postulated Vesicular Stomatitis Virus Entry into the Brain Following Nasal Inoculation with Possible Sites of α-Synuclein Aggregation in Infected Anatomical Structures along the Olfactory Circuitry as well as via the Vagus Nerve.

Materials and Methods

Animal model

All mice utilized for this study were bred on a C57bl/6J background (Jackson Laboratories) and were of adult age (6-11 weeks), weaned approximately two weeks post birth and housed in single cage housings containing 2-5 mice. Males and females included in this study were separated and *Snca* knockout mice were kept apart from their wildtype littermates. All mice had access to water and food at all times (*ad libitum*) and kept on a 12-hour light/ dark cycle. Mice of the wildtype genotype were maintained by Dr. Q. Jiang and included both males and females, whereas mice of the *Snca* KO genotype were all females and maintained by Dr. J. Coulombe. All infections were performed in a containment level 2 biohazard facility authorized and approved by the University of Ottawa and The Ottawa Hospital Research Institute's specialized safety entities. Experiments were performed under the guidelines of the Canadian Councils on Animal Care and approved by the Ethics Board of the Animal Care Committee at the University of Ottawa.

Nasal Infection with Vesicular Stomatitis Virus Expressing GFP (VSV-GFP)

Clonally purified Vesicular Stomatitis Virus of the Indiana serotype, known to cause neuronal lethal toxicity and severe encephalitis, was the choice for the infectious paradigm used throughout this study. Original stocks of VSV-GFP were prepared by Dr. E. Brown (University of Ottawa) and aliquots of 10^8 PFU of virus were stored at -80^{o}C. Adult mice were nasally inoculated with $3x10^3$ plaque-forming units (PFU) VSV-GFP diluted in 50uL of PBS following anesthesia using 3% isoflurane at 1L/m for 1 minute. Mock mice were also anesthetized using the same formula and administered 50uL of PBS into their nostrils. The dosage of VSV-GFP is

predetermined as LD_{50} from previous studies performed by our lab using this paradigm model. Mice of the wildtype genotype aged 8-11 weeks – titled hereafter as the main cohort – were a total of 25 and are summarized in **table 2** in the appendix according to their sacrifice time-point, genetic background, sex, treatment, and subsequent intended processing of the tissue. An additional cohort – titled hereafter as the symmetry cohort – included adult mice aged 11-13 weeks infected similarly with the WT Indiana strain of VSV-GFP. The purpose of this cohort was to report on any right vs. left side and different anatomical regions of the brain in regard to viral concentration and localization and is summarized in **table 4** in the appendix in a similar fashion to the main cohort in addition to the anatomical region excised and examined. All mice were monitored daily starting one day post-inoculation (1DPI) for any signs of sickness that may indicate an endpoint. The classification of disease score according to observed disease phenotype is classified in **table 5** in the appendix as to which phenotype is considered a humane endpoint for the animal showing that phenotype. At the $3x10^3$ PFU dose of VSV-GFP used, mice are expected to start showing signs of sickness that are observable phenotypically, if any, on day 6 post-inoculation. One mouse only of the 10DPI group (F1-202) showed signs of mild hindlimb paralysis on the left side on day 7PI and worsening on day 10PI. However, no mice showed severe signs of sickness and deterioration (i.e., a score of 4 according to **table 4**) and warranted for an early humane sacrifice. All animals fulfilled their intended disease course and were sacrificed at the pre-planned timepoint.

Tissue Preparation - Immunohistochemistry and Indirect Immunofluorescence

Adult mice aged 8-11 weeks belonging to the main cohort were sacrificed at predetermined timepoints: 2-, 4-, 6-, and 10-days post-inoculation. The main cohort and *Snca*-

KO mice were similarly processed for immunohistochemical and indirect immunofluorescence analysis, and subsequent quantification of carefully selected immune cells phenotypical parameters. Mice were euthanized at the end of each disease course (group specific) by administering Euthanyl intraperitoneally followed by the flushing of 10 mL of PBS using a cardiac puncture to remove blood from the collected whole heads in a cardiac perfusion fashion. Whole head mounts – or skulls – were separated according to a method devised by the Schlossmacher lab in 2017, coined holocranohistochemistry (Tomlinson et al., 2017), which enables the visualization and the study of the intact olfactory system and associated nerves of the central nervous system (e.g., cranial nerve-1) which essentially enables the studying of α-synuclein in anterior olfactory anatomical structures such as the olfactory epithelium, ethmoid sinuses, lamina propria, the nasal cavity, and olfactory sensory neurons. To fix tissue, 10 mL of 10% formalin (Fisher Scientific, Ottawa, ON, Canada) was pumped in following PBS via the cardiac puncture. The heads were obtained through decapitation, after which the scalp was removed. Subsequently, the heads were immersed in 10% formalin and fixed for 48 hours at a temperature of 4 °C. They were then transferred to 70% ethanol for temporary storage, which lasted for a period of 1 to 10 days. To soften the skull bone, heads were submerged in 12.5% formic acid for 5 days, and afterwards, they were rinsed with running tap water for approximately 2 to 3 hours. The tissue specimens were dehydrated using a sequential process involving immersion in ethanol of increasing concentrations: 60%, 70%, 80%, and 90% for 1 hour each, followed by 100% ethanol for 4 hours total. Subsequently, the heads underwent two 1-hour submersions in xylene/toluene and were finally immersed in paraffin solutions for 4 hours before embedding. The paraffin-embedded blocks were cut into serial sections, starting from the midline, and branching out, with each section measuring 5 μm in thickness. These sections were

then placed onto glass slides for mounting. The mounted head sections were subsequently dried at a temperature of 37°C for a period of 48 hours. Due to the bone-rich nature of the whole head mounts, although decalcified using formic acid, an extra step of heating up the mounted skull sections on charged slides was deployed. Slides were heated overnight at 37ºC and at 58ºC for 30 minutes prior to commencing with the immunohistological staining protocol. This step has proven to help with the adherence of the tissue on the slide and the drying out of any trapped or condensed water droplets that might have built up under the tissue causing the tissue to fall off while processing for staining.

Immunohistochemistry and Indirect Immunofluorescence

The slides of whole head mounts underwent a rehydration and deparaffinization process, starting with 3x5 minutes in Citrisolv (Decon Labs, Inc., King of Prussia, PA, USA; 1601) and involving a subsequent series of gradual washes of 2x1 minutes in 100% ethanol, 95% ethanol, 75% ethanol, and 50% ethanol, ending with 2x1 minutes of rehydrating in pure ddH_2O. To inhibit endogenous peroxidase activity, 10% hydrogen peroxide (Sigma-Aldrich, Co., St. Louis, MO, USA; 216763-100ML) was diluted in methanol with which sections were treated for 10 minutes. When processing slides for indirect immunofluorescence, this step was skipped due to the nature of the detection system and the unnecessity of quenching peroxidase activity. Antigen retrieval was performed to restore antigens and unmask epitopes affected by fixation by heating up the slides to 92-95ºC in 10X Sodium Citrate Buffer solution of pH 6.0 diluted in ddH_2O to 1X and a 10mM solution (Invitrogen, Carlsbad, CA; 92008) in a water bath for 15 minutes followed by a cooling down period of 30 minutes at room temperature. The use of the water bath instead of a conventional microwave or a pressure cooker was devised due to the nature of the ossified

bone of the skull mounts which interferes with an optimal adherence of tissue to the charged slides. This workaround helped preserve the delicate tissue and decreased the chances of tissue falling off the slide or folding on itself by eliminating the vigorous boiling. Of note, no alternative antigen retrieval methods (i.e., chemical-induced antigen retrieval or heat-induced antigen retrieval of a different pH buffer) were necessary. In order to block non-specific binding, the slides were incubated in 10% goat serum (Vector Laboratories, Burlingame, CA, USA; S-1000) for 30 minutes at room temperature, and the choice of goat serum as a blocking reagent was appropriate since the host of all secondaries used in this project was goat. Subsequently, the slides underwent the following standardized steps for both IHC and IIF: 1) overnight incubation with the primary antibody (as listed in Appendix, **table 5**) at 4°C followed by 3x5 minutes washes of PBS; 2) 90-minute incubation at room temperature with either a biotinylated or a fluorophore conjugated appropriate secondary antibody in a dark chamber for IHC [1:225], or IIF [1:200], respectively, and geared at the host species of the primary used (as listed in the Appendix, **table 6**) followed by 3x5 minutes washes in PBS. For IIF, sections were then incubated for 5 minutes in an autofluorescence eliminator reagent (Millipore Sigma, Burlington, MA, USA; 2160), then washed off with 3x1 minute of 70% ethanol. Sections were finally treated with Vectashield: a mounting medium for fluorescence with DAPI (Vector Laboratories, Burlingame, CA, USA; 94010), cover slipped with a #1.5 thickness cover (Fisher Scientific, Pittsburgh, PA 15275), and excess mounting medium was blotted off. Commercial transparent nail polish was used to seal the edges of the coverslip and the slides were left to dry in the dark for at least 30 minutes before viewing. For long term storage, slides were kept at 4^{o}C in closed cardboard boxes. For IHC, a 90-minute incubation at room temperature with an ABC-HRP kit (Avidin/biotin complex - horse radish peroxidase; Vector Laboratories, Burlingame, CA, USA;

PK-6100) following the application of the secondary antibody was performed. Development of the slides was achieved by applying 3,3'-diaminobenzidine (DAB; Sigma; D5637-5g) [0.055M] for approximately 3 minutes at room temperature. Counterstaining was performed using Hematoxylin+ (Fischerfinest, Pittsburgh, PA; 15275), followed by reverse dehydration through a sequential series of washes from water to an organic solvent as follows: 3x5 minutes in ddH_2O, 1x1 minute in 50% EtOH, 1x1 minute in 70% EtOH, 1x1 minute in 95% EtOH, 1x1 minute in 100% EtOH, 1x1 minute in 50% EtOH/ 50% Citrisolv, and 1x1 minute in 100% Citrisolv. Finally, the slides were cover-slipped with #1 thickness coverslips (Fisher Scientific, Pittsburgh, PA 15275) and mounted using Permount mounting medium (Fischer Scientific, Fair Lawn, NJ, USA; SP15-100) and left till next day to dry before viewing.

Quantification of Immune Cells Morphological Parameters

The criterion for signal quantification was entirely established, devised, and complied by me, with clarification on some aspects of the program used offered by the CBIA core (RGN 3111 and RGN 4206, 451 Smyth, Faculty of Medicine, University of Ottawa, Ottawa, ON, CA), and the basic functions explained in simple terms in the online-available tutorial by Kristopher Kubow (2019). The purpose of this quantification process was to characterize the inflammatory response and ongoing inflammation elicited by these infected mice in response to the introduced neurotropic virus in measurable and comparable units and look into any potential immune modifications or shortcomings influenced by the lack of α-synuclein in *Snca* KO mice that translated into phenotypical differences compared to their wildtype counterparts. Fiji (ImageJ 2) version 2.14.0 was used to analyze and quantify Z-stack images generated from scanning the whole-head, stained skulls utilizing an axioscanner at x20 at Louise Pelletier Histology Core

(RGN 4145, 451 Smyth, Faculty of Medicine, University of Ottawa, Ottawa, ON, CA), and stored as a czi. file. The Bio-Formats plugin in Fiji (ImageJ 2) version 2.14.0 was used to access the czi. files and scanned images were accessible in the form of complied series, with series 1 being the highest resolution. Throughout my quantification, series 3 was consistently chosen to open files due to the intense load put on the device's RAM by higher series options. The criterion, which can be found in the appendix and is summarized in step-by-step fashion, was used to quantify microglial and astrocytic parameters of interest from infected WT and *Snca* KO mice but also mock mice. Areas of interest included the olfactory epithelium, olfactory bulb, anterior olfactory nucleus, the cerebellum, and the midbrain. In addition to assessing the glial response in chosen areas of interest as whole anatomical regions, a gradient analysis was also performed on representative sections from animals that clearly showed viral presence in one or more of the glomeruli in the glomerular layer. This analysis was performed on four different levels described in **table 8** of the appendix, with the aim of looking for more distinct microglial and astrocytic alterations of the measured parameters in the glomerulus directly impacted by VSV-GFP and gradually increasing the selected area in fixed selection intervals to record the shifting in those measurements, if present, in the immediate but also farther out areas adjacent to those infected glomeruli.

Tissue Preparation – Viral Titering, PFU Analyses, and Western (Immuno) Blots

Adult mice aged 6-11 weeks belonging to the symmetry and main cohort were sacrificed at days 2 and 6 post-inoculation respectively for PFU analysis and immunoblotting. The chosen timepoints were intended to include the peak viral titer in the brain using this viral paradigm corresponding to 2DPI as determined in the past by our lab but also in other studies (Fensterl et

al., 2012; Nair et al., 2014). The later 6DPI timepoint was designed and suggested by Dr. E. Brown as a good readout to investigate the viral concentration after the titer has climaxed and host's immune response has begun deactivating the viral replication. In an identical manner to mice processed for immunohistological studies, mice were euthanized at the end of each disease course (group specific) by administering Euthanyl intraperitoneally followed by the flushing of PBS using a cardiac puncture to remove blood from the collected organs of interest in cardiac perfusion fashion. The brain and olfactory bulbs were collected for animals intended for this analysis. Upon collection, the tissues were immediately frozen at -80^{o}C and set aside for subsequent processing. To prepare the frozen tissue, it was lysed in PBS and homogenized using metal beads and a Magna Lyser machine from Roche, operating at a speed of 7000 for 10 seconds. The dilution in PBS was as follows: 2x the organ weight for hemibrains and hindbrains, and 5x the organ weight for olfactory bulbs; a summary of samples and their respective measurements is found in **table 4** in the appendix. Samples were then rapidly frozen using liquid nitrogen and allowed to thaw on ice, which aids in breaking up the cellular membrane and detecting intracellular viral particles. The thawed lysate was then centrifuged at 5,000 rpm for 10 minutes at 4^{o}C, and resulting supernatants were used for serial dilutions and titering of the virus in respective samples.

Cell Culture

L929 (originally derived from murine subcutaneous connective tissue, ATCC CRL-6364) cells were grown in Eagle's Minimum Essential Medium (Gibco, Grand Island, NY, USA) supplemented with 55 mL of 10% fetal bovine serum (Thermo Fisher Scientific, Gibco), 500 uL B-mercaptoethanol, 500 uL Gentamicin, 5.5 mL L-glutamine (Millipore Sigma). Cells were

incubated in a 5% CO2 humidified incubator at 37ºC.

Assessing the Viral Burden in VSV-GFP Infected Mice

Two days preceding the plaque assay, L929 cells were carefully seeded in 6-well culture plates to ensure they achieved a confluency level of approximately 90% by the infection day. For the plaque assay, the samples were serially diluted in 10-fold fashion starting with 1:10 of the supernatant of the homogenized and centrifuged samples using serum-free Dulbecco's Modification Eagle's Medium (DMEM, Multicell, Wisent Inc.). Subsequently, 100µL of the diluted samples were added as an overlay to each well, where each dilution was done in duplicates as technical replicates. Upon adding the overlay of the viral suspensions, cells were incubated at a temperature of 37°C with 5% CO2 for 1 hour. During this time, the plates were gently rocked every 15 minutes to guarantee an even distribution of the viral suspensions among the cells. Following the incubation period, the viral suspensions were removed, and the cells were then overlaid with 2mL of a mixture consisting of 1% agarose and 2x DMEM (Gibco, Thermo Fisher Scientific) supplemented with 10% FBS at a 1:1 ratio. The overlay was left to solidify in room temperature in the biological safety cabinet before moving them into the incubator; plates were once again incubated at a temperature of 37°C with 5% CO2 for a duration of 24 hours. On the subsequent day, roughly 24 hours from the when the infection was initiated, the cells were fixed in 2mL of Carboy's reagent constituting of a mixture of methanol and acetic acid [1:3] in room temperature for 90 minutes and kept inside the biological safety cabinet. The overlay covering the cells was then gently removed using running tap water, and the cells were stained with a solution of Coomassie blue (consisting of 0.1% Coomassie Brilliant Blue, 20% methanol, and 10% acetic acid) for a period of 30 minutes at room temperature on a

rocker at low speed. Following the staining, the reagent was removed, and the plates were left to dry in room temperature before manually counting the plaques in each well. The titers were calculated using a formula – found below – that accounts for the number of the plaque, the dilution factor, and the homogenization ratio of organ dilution in PBS, and then converted to PFU/g tissue.

PFU/g = (mean number of plaques x homogenizing factor) / D, where 'homogenizing factor' represented the dilatation factor and 'D' was the dilution of the virus. For reference, organ dilutions (or homogenizing factors) were as follow: 2x dilution for hemibrains and hindbrains or 5x dilution for olfactory bulbs, where x2 and x5 the original weight of the organ was added in PBS buffer to the homogenizing snap tube, respectively.

Western Blotting

Organs harvested at 6DPI, including hemibrains and olfactory bulb samples, were flash frozen in liquid nitrogen and kept in -80^{o}C until lysed for processing. Western blots were only performed on hemibrain samples. Olfactory bulbs were omitted due to limited remaining volumes after completing the plaque assay analyses. Lysis was performed using 1x PBS-T buffer (10x PBS diluted in ddH_2O to 1x and 0.1% Tween 20), pH balanced to 7.5, and topped up with ddH_2O up to 100mL and stored in -20^{o}C. The lysates were incubated on ice for 20 minutes and then centrifuged at 20,000 RPM for 20 minutes. To determine protein concentrations, a bicinchoninic acid (BCA) assay kit (ThermoFisher Scientific) was utilized. The protein samples were mixed with a NuPAGE loading buffer (LDS sample buffer 4x, Invitrogen, ThermoFisher Scientific) containing 5% beta-mercaptoethanol and heat-blocked at a temperature of 95°C for 5 minutes to help denature the proteins. Subsequently, the samples were subjected to

electrophoresis and separated under reducing conditions on a 15-well gel, 1.0mm thickness, 10% SDS, 4-12% bis-tris (SDS-PAGE) gel (Invitrogen, ThermoFisher Scientific). The semi-dry transfer of the gel onto polyvinylene difluoride (PVDF) membranes was carried out using the iBlot Blotting System following the manufacturer's instructions (Thermo Scientific). The membranes were fixed by briefly boiling them with 0.4% paraformaldehyde (PFA) in the microwave for 30 seconds to prevent protein detachment and aid in the retention of α-synuclein on the membrane since it's a relatively small protein. Membranes were rinsed using ddH_2O twice and then blocked with 5% fat-free milk in 1x PBST for 1 hour. For the purposes of detecting endogenous α-synuclein in the hemibrains and viral particles, the following primary antibodies were used (also summarized in **table 6** in the appendix): Syn-1 (K0112, BD Biosciences, 1:3000), and VSV (Dr. Earl Brown, 1:6000). Primary antibodies were diluted in 5% fat-free milk for a total volume of 10mL and incubated with the membranes overnight at 4°C on shaker. Membranes were rinsed with ddH_2O and 3 x 5 minutes of PBS-T the next day followed by the addition of horseradish peroxidase-conjugated secondary antibodies (α-mouse, NA93IV, GE Health Care, 1:10000; α-rabbit, NA934V, GE Health Care, 1:10000) also diluted in 5% fat-free milk for 1 hour in room temperature on a shaker. Membranes were then washed using 1x PBS-T for 15 minutes twice. The membranes were then developed using an enhanced chemiluminescence kit (Supersignal West Pico PL, ThermoScientific) for 1 minute in RT and subsequently imaged using the ChemiDoc imaging system (BioRad Laboratories).

Densitometry and Quantification of Immunoblot Bands

Digital images of the Western blots were captured using a chemiluminescent imaging system (ChemiDoc imaging system, BioRad Laboratories), ensuring that the exposure settings

were optimized to avoid overexposed or underexposed bands. Subsequent analysis was conducted using Fiji (ImageJ 2) software version 2.14.0 according to the following established protocol:

- Open scanned image and convert to greyscale.
- Rotate image if blot is not straight.
- Launch image in Fiji (ImageJ 2) software.
- Click on box shape and select region of interest:
    - Press on 1, then click box and move to next region and press 2.
    - Click box and move to next region and press 2.
    - At last region press 3, the pixel graph will display.
- Use the line option to draw a line spanning from the right most bottom point of the curve to the left most bottom point of the curve, ensuring to include as much of the area under the curve (AUC) as possible.
- Use the wand function and click on each AUC.
- Results from each selection representing the AUC will pop up in separate window described as pixel density (pixel/inch).
- Select and copy/paste this into excel file and identify your lanes.
- Divide value obtained from WB by value obtained from densitometry of Ponceau S or actin control = level of protein of interest/total protein.

Values obtained following quantification were normalized according to control stain used and plotted in two separate groups of infected vs. mock-treated mice; appropriate statistical analysis was then performed.

Statistical Analysis

Statistical significance was calculated using ordinary one-way ANOVA (nonparametric) and Mann-Whitney test (unpaired, nonparametric), as indicated in the figure legends. For all statistical analyses, differences were considered significant when a *p*-value was below or equal to 0.05. Statistical analyses were performed using GraphPad Prism 9.0 (GraphPad Software Inc., San Diego, CA, USA).

Results

Localization and Tropism: Progressive Encephalitis Caused by VSV-GFP

To investigate the extent of pathology in brain regions of interest and in different areas of the olfactory tract and determine the severity of the inflammation following a nasally acquired VSV-GFP infection, the tracking of the viral invasion and establishment of viral particles' localization across the studied timepoints were critical to carry out the aforementioned study. Further, the definition of infected areas as per the positive staining of viral proteins helped direct the exploration for pathological modification of α-synuclein (i.e., post-translational modifications) downstream of the viral assault and concurrent inflammatory response.

To accomplish this, adult mice aged 6-11 weeks were inoculated with the mouse-adapted, Indiana strain of VSV-GFP nasally via the nose pad with a median lethal dose (LD_{50}) of $3x10^3$ PFU as determined previously by our lab, where mock animals received PBS through the same route. VSV has been reported to cause encephalitis in mice when inoculated through the nose (Ciavarra et al., 2018) and thus constitutes a suitable model to study the progression of inflammation and its consequences in the brains of mice but also the state of endogenous α-synuclein. Mice were sacrificed at 2 DPI, which has been identified as a time point of peak titer in brain and lung in two independent studies of VSV infection in C57BL/6J mice (Fensterl et al., 2012; Nair et al., 2014). Peak infection, however, inferred by the inflammatory response and the activation of immune cells occurs later in the course of infection, which signified the sacrifice of mice at days 4, 6, and 10PI to further characterize this paradigm in the olfactory circuitry and the associated inflammation. In the main cohort, as shown in **table 2** in the appendix for more details, no mice were declared moribund, and all reached their designated sacrifice timepoint. All non-moribund mice were sacrificed at 10 DPI at the end of the disease course. Since the virus

expressed GFP as it enters the cells and replicates its genome, the use of both anti-VSV and anti-GFP antibodies of different hosts was possible, which complemented and corroborated each other where viral staining was seen.

The holocranohistochemistry technique was utilized throughout this project as it permits the visualization of the olfactory system from the nasal cavity to mitral cells and dopamine-producing interneurons of glomeruli in the olfactory bulb compared to the normal brain extraction method (Tomlinson et al., 2017). Staining of whole-head skulls of mice from the main cohort using anti-VSV and anti-GFP primary antibodies in the sagittal plane allowed for the identification of the topographical distribution of the infiltrating virus and monitoring its progression and travel along different routes across the different planned sacrifice timepoints. It appeared that VSV-GFP consistently infected, and likely also replicated, in the olfactory epithelium early-on in the course of infection before infiltrating into deeper olfactory structures later when introduced nasally, and is spotted prominently in olfactory sensory neurons (OSNs) and in bundles of the first cranial nerve (CN-I) that carry olfaction signals from those neurons in the olfactory epithelium and onto the olfactory cortex in the cerebral cortex, which includes the piriform lobe and the hippocampal formation (Helwany and Bordoni, 2022). The virus was transported along the axonal cytoplasm of the traversing nerve fibers in the olfactory nerve layer (ONL) and across the lamina propria and cribriform plate to reach the bulb's glomeruli, or the glomerular layer (GL), which is the outer layer of the olfactory bulb surrounded by a sheath of glial cells and represents the first synaptic site within the olfactory system, where axonal terminals of CN-I synapse with efferents from periglomerular cells (PGs), mitral cells (MC), and tufted cells (Furudono et al., 2013). At 2DPI, the olfactory epithelium, neurons, supporting cells, and basal cells were infected to varying degrees (**A, figure** 2), and the epithelium displayed a

patchy appearance of positive staining due to localized foci of viral infection. Of note, few-to-no viral antigen-positive cells were observed in the respiratory epithelium (RE) in the nasal turbinates (not shown), characterized by a pseudostratified ciliated columnar epithelia intercepted by goblet cells in the back of the nasal cavity. The invasion of CN-I nerve fibers was seen as soon as day 2PI (**B, figure 2**), however, no positive staining of glomeruli at any level was seen until day 4PI, which alludes to the manipulation of the afferent nerve fibers from the olfactory epithelium into deeper olfactory structures. It has been observed that VSV-GFP spreads transynaptically using both anterograde and retrograde transport from the olfactory bulb to other regions of the brain, using known olfactory connections (Forger et al., 1991; Andersson et al., 1993). Notably, and consistent with the literature of mouse encephalitic invasion of VSV earlier in the disease course of lower brainstem structures (Huneycutt et al., 1994), positive staining using anti-VSV-GFP was seen in some cases in the spinal nucleus of the trigeminal – caudal part (SPVC) (**C, figure 2**), but also subtle staining in the spinal vestibular nucleus (SPIV) (D, figure 2); a cranial nucleus for the vestibular nerve located in the brainstem. This is congruent with reports on the transport of VSV *in vivo* via autonomic nerves of the autonomic nervous system branching from the lungs secondary to swallowing nasal secretions of the virus (Huneycutt et al., 1994).

Starting on day 4PI, positive staining of viral particles was seen in distinct and adjacent glomeruli (**F, figure 2**) in the glomerular layer, indicative of a successful penetration of the virus into the mouse olfactory bulb and consistent with the anterograde transport of VSV-GFP into the brain through the olfactory route, hijacking the axonal terminals of the olfactory sensory neurons that interconnect with other processes in the glomerular junctions. In the olfactory epithelium, extended regions of viral staining, and increased numbers of cells, and more intense labelling of

the olfactory nerve bundles (**E, figure 2**) were observed. Edema and heavy staining of the mucosal lining of the epithelium was also frequently seen, possibly resulting from the disrupted homeostasis in this region or the occurring inflammatory response, or both. No apparent staining past the glomeruli in the bulb was observed in any of the mice belonging to this timepoint group (not shown). Caudal brain regions that were VSV-GFP-positive included the lateral vestibular nucleus and the superior vestibular nucleus (LAV, SUV, respectively) (**H, figure 2**), both of which are superior and more rostral structures of the medulla, indicating a progression of VSV-GFP deeper into the medulla compared to day 2PI. Interestingly, positive staining was also seen in the stratum oriens in field CA2 in the hippocampus (**G, figure 2**) in one of the cases, albeit immunoreactivity of the hippocampal fields and dentate gyrus were reported in the literature by day 7PI when VSV was introduced nasally (Huneycutt et al., 1994; Huneycatt et al., 1994).

At a later timepoint, the 6DPI group retained the viral staining in the epithelium, the afferent nerve fibers, and was consistently detected in the glomeruli (**I and J, figure 2**), but was also interestingly seen in a couple animals in the inner layers of the olfactory bulb (**K, figure 2**) – namely the subependymal layer. Contrary to the infection observed in the glomerular layer on day 4PI, where staining was mostly localized to a pack of neighboring glomeruli, positive glomerular staining in 6DPI animals was more distributed and dispersed, spanning the length of the infected olfactory epithelium at times, accompanied with signs of severe infection and damage to the epithelium, such as the detachment of the outer most mucosal layer of the epithelium in contact with the nasal cavity, the general disorganization and the swelling of the epithelial orientation, and the inconsistent thickening of the epithelium where cells appeared either enlarged or degenerate. The observation of discrete VSV-GFP staining beyond the granule cell layer indicates a complete penetration of viral proteins into the bulb and the possible

advancement past the bulb into deeper and more rostral olfactory structures. Other novel regions where VSV-GFP particles were not seen prior to this timepoint included the cerebellum in the pyramus VIII (PYR VIII) and uvula IX (UVU IX) (**L, figure 2**), where viral staining in two mice was robust and unmistakably present. Since the mock-treated mice were sacrificed alongside the 6DPI group, images of anti-VSV-GFP are taken from similar areas of the brain to showcase the absence of staining in mock-treated mice (**M-P, figure 2**) in comparison with viral positive areas in the 6DPI mice, but also the cleanliness of the background using this antibody under optimized conditions.

Finally, at the latest timepoint in the experimental design of this cohort, the 10DPI group continued to show staining of main olfactory structures seen at previous timepoints (**Q and R, figure 2**), although to a lesser extent, including the inner layers of the olfactory bulb, consistent with the observations in the 6DPI group. Moreover, viral positive staining was also witnessed in the olfactory tubercle inferior to the pyramidal layer (**S, figure 2**), indicating an invasion of the viral insult of the olfactory tract post 6DPI and including 10DPI. The infection of deeper olfactory structures such as the piriform cortex, amygdala, and the entorhinal cortex, although not seen in this cohort, remains possible, with reports of the Indiana serotype of VSV infecting named areas past 7 days post the nasal inoculation (Huneycutt et al., 1994). An interesting brain region – in the context of PD pathogenesis– where VSV-GFP was not seen prior to the 10DPI timepoint was the SNpc in the midbrain (**T, figure 2**). Co-labeling of anti-VSV-GFP and anti-tyrosine hydroxylase (TH) – to label dopaminergic neurons – in a 10DPI mouse (**B, figure 3**) and a direct comparison with the mock (**A, figure 3**) that omitted viral staining in the area served to confirm the exclusive presence of viral proteins in this area and ruled out the possibility of

confusing it with other areas of the midbrain that might obstruct the viewing of the SNpc if cut too medially or laterally.

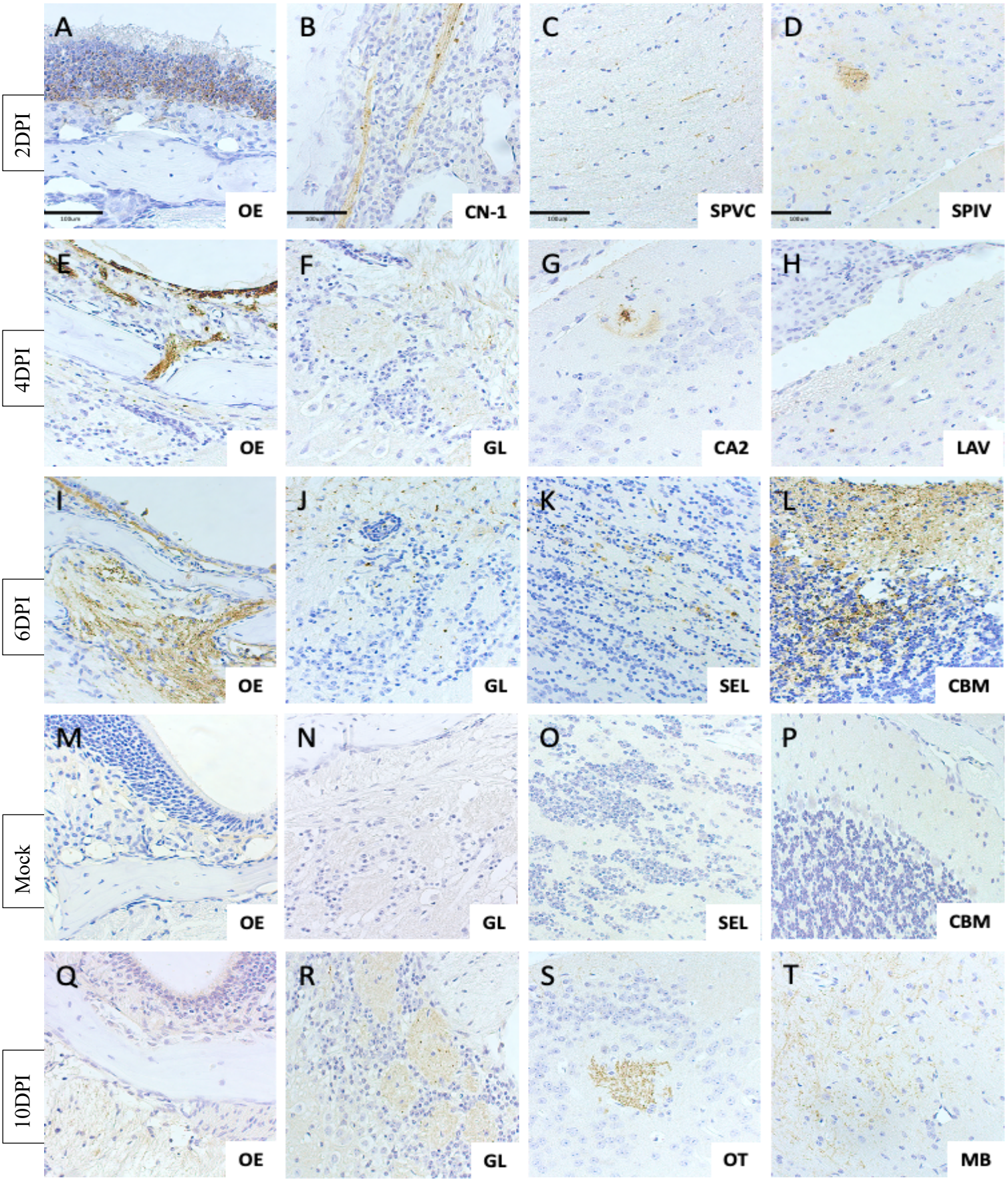
2DPI
4DPI
6DPI
Mock
10DPI
A
OE
B
CN-1
C
SPVC
D
SPIV
E
OE
F
GL
G
CA2
H
LAV
I
OE
J
GL
K
SEL
L
CBM
M
OE
N
GL
O
SEL
P
CBM
Q
OE
R
GL
S
OT
T
MB

Figure 2: The Distribution of Vesicular Stomatitis Virus-Encoded Proteins Reveals the Progressive Nature of Infection and Selective Route of Entry. (A-T) Immunohistochemical (IHC)-developed images illustrating the viral tropism indicated by positive anti-VSV staining in a temporal fashion, highlighting important areas in the course of infection. Notice how the olfactory epithelium remains VSV-GFP-positive throughout the course of infection, while deeper olfactory structures, such as the subependymal layer of the bulb and the olfactory tubercule, and higher encephalic structures, such as the cerebellum and midbrain, do not show positivity until past day 6 of the introduction of VSV-GFP, pointing to the progressive nature and elucidating the selective anterograde and retrograde travel of this virus in the mouse brain. OE: olfactory epithelium; CN-1: cranial nerve 1; SPVC: spinal nucleus of the trigeminal, caudal part; SPIV: spinal vestibular nucleus; GL: Glomeruli; CA2: Hippocampal region; LAV: lateral vestibular nucleus; SEL: Subependymal Layer; CBM: Cerebellum; OT: Olfactory Tract; MB: Midbrain. 2 sections were stained per (n) mouse, where n=21Scale bar: 100um.

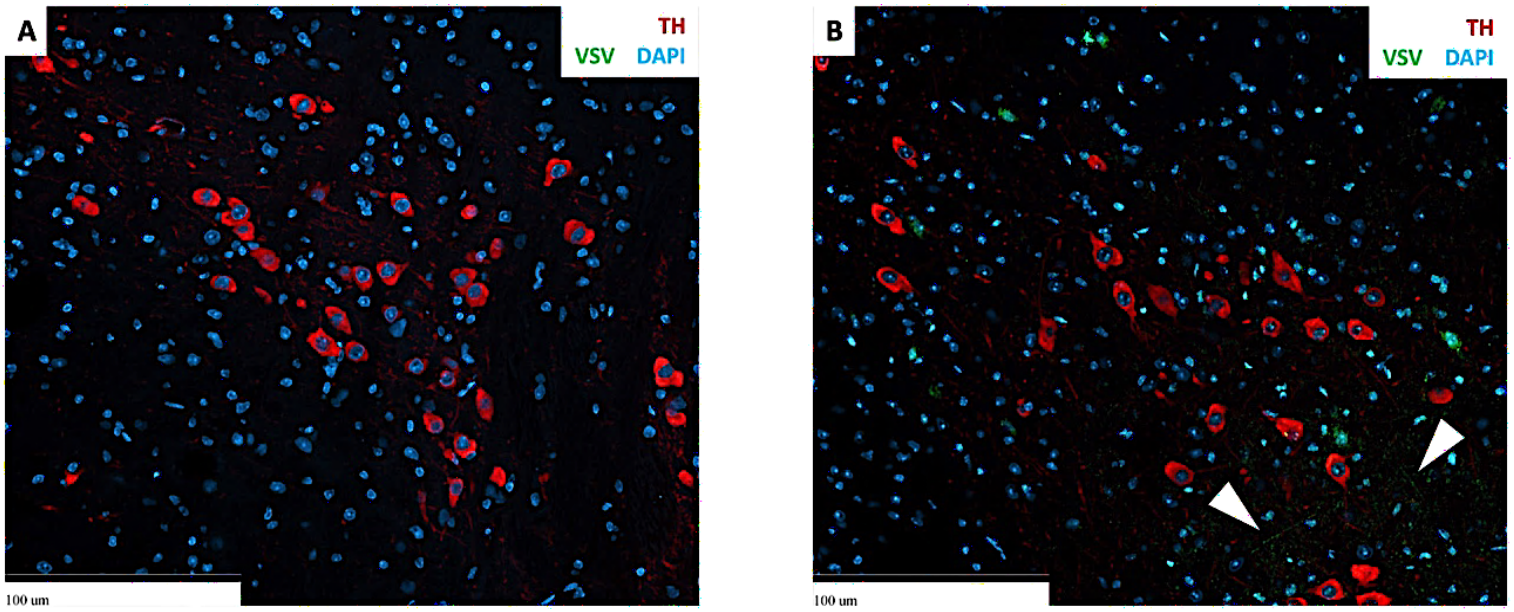

Figure 3: Vesicular Stomatitis Virus Infiltrates an Area of the Substantia Nigra Rich in Dopamine Neurons by Day 10 Post-Inoculation. Indirect immunofluorescence (IIF)-based micrographs of the midbrain area positive for VSV-GFP showcasing TH+ neurons characteristic of the compact part of the substantia nigra in whole-mount skulls of (B) 10DPI mice in comparison with (A) mock-treated mice void of viral reactivity. Notice the tiny filament-like staining pattern in (B) reminiscent of VSV-GFP observed in immunohistochemical development (white arrowheads), confirming the presence of viral proteins within the dopaminergic neuronal population in the substantia nigra pars compacta of the midbrain. 2 sections were stained per (n) mouse, where n=2 Scale bar: 100 um.

Viral Concentration Determination: Viral Titers in Infected Animals are Highly Variable

Quantifying the viral titer in the brains and the olfactory bulbs of infected mice played a vital role in comprehending the pathogenesis and advancement of the VSV-GFP-induced infection. This procedure entailed determining the quantity of virus within the brain and olfactory bulb tissue, of mice sacrificed at 2- and 6DPI, offering valuable insights into the replication and dissemination of the virus throughout the central nervous system and supporting some of the findings established via immunohistological techniques.

As mentioned in the materials and methods section - *Nasal Infection with Vesicular Stomatitis Virus Expressing GFP (VSV-GFP)*, a subsidy of mice aged 8-11 weeks from the main cohort at 6DPI were sacrificed and processed for plaque assaying – and ultimately immunoblotting – alongside their counterpart 6DPI group included also in the main cohort and processed and analyzed immunohistologically. There was a total of 12 samples divided into 8 hemibrains and 4 olfactory bulbs, where the hemibrains included the brain except for the olfactory bulb that was removed surgically. In this subsidy, hemibrains were separated into right and left, and olfactory bulbs were pooled together. It is worth mentioning that the samples excised for this subsidy (i.e., hemibrains and olfactory bulbs) belonged to the same animal, so the plaque assay did not only give a generous idea into the viral concentration in these regions separately at a given timepoint, but also a simple yet insightful comparison between the viral burden in an area into which the virus was introduced (olfactory bulbs), and the rest of the brain (forebrain, midbrain, and hindbrain collectively).

Further, the plaque assay revealed markedly variable viral titers at this timepoint, which is expected since the interferon and immune response to VSV-GFP heightens after 5DPI and the virus begins to be effectively cleared, with most hemibrain samples showing no detectable virus

(i.e., below the detectable threshold limit), which is 200PFU. This does not, however, equate the absolute clearance of viral proteins, because if the immune response were to be artificially altered into deficiency on or after day 6PI when the viral load is undetectable, the probability of the viral concentration increasing again above the detectable threshold would still exist. As it stands, and from the great fluctuation in viral titers observed and the inability to detect a viral load in most hemibrains, it appears that mice by day 6PI were able to handle and bring down the infection by clearing out the infectious particles and decreasing the viral titers, indicating an efficient immune response to the introduced VSV-GFP.

The symmetry cohort was a special cohort of mice designed to measure the infectious VSV-GFP particles at day 2PI, which, as mentioned, is the viral titer peak according to literature using this viral paradigm (Fensterl et al., 2012; Nair et al., 2014), in comparison to the 6DPI group, but also to expand our understanding of the VSV-GFP preference for distinct general anatomical regions and the unilateral vs. bilateral localization of the virus. For that, full brains were surgically removed and divided into either olfactory bulbs and hindbrains, right and left, or kept as full hemispheres, including the olfactory bulb in this case. By doing that, the measuring of viral titers in olfactory bulbs and hindbrain samples belonging to the same animal became possible, which both supported the immunohistological work where positive viral staining was seen in parts of the hindbrain (e.g., the medulla), but also gave insight into which region had a higher infection and viral replication rate. The latter was useful in determining which viral entry route – whether be it the olfactory nerves through the olfaction route or the vagus nerve and autonomic nervous system secondary to swallowing nasal secretions of the inoculated virus – were manipulated to gain access to particular brain regions.

Distinct patterns of viral titer distribution within the mouse brain emerged when the viral burden was assessed in the 6DPI group. Notably, the hemibrain regions exhibited a relatively low viral titer at this specific time point, with 5 out of 8 total samples showing no detectable infectious virus by means of plaque assay (**A, figure 4**). This could be indicative of an ongoing immune response that restricts viral replication and dissemination within these areas. In stark contrast, the olfactory bulbs displayed a notably higher viral titer (**B, figure 4**) compared to the hemibrains. This discrepancy might highlight the olfactory bulbs' role as a primary entry point for VSV-GFP into the central nervous system, thus facilitating its efficient replication and amplification. The differential viral titer between these regions underscores the complex interplay between viral propagation, immune responses, and tissue-specific vulnerabilities at this timepoint in the course of infection, contributing to our understanding of VSV-GFP's neuroinvasive mechanisms.

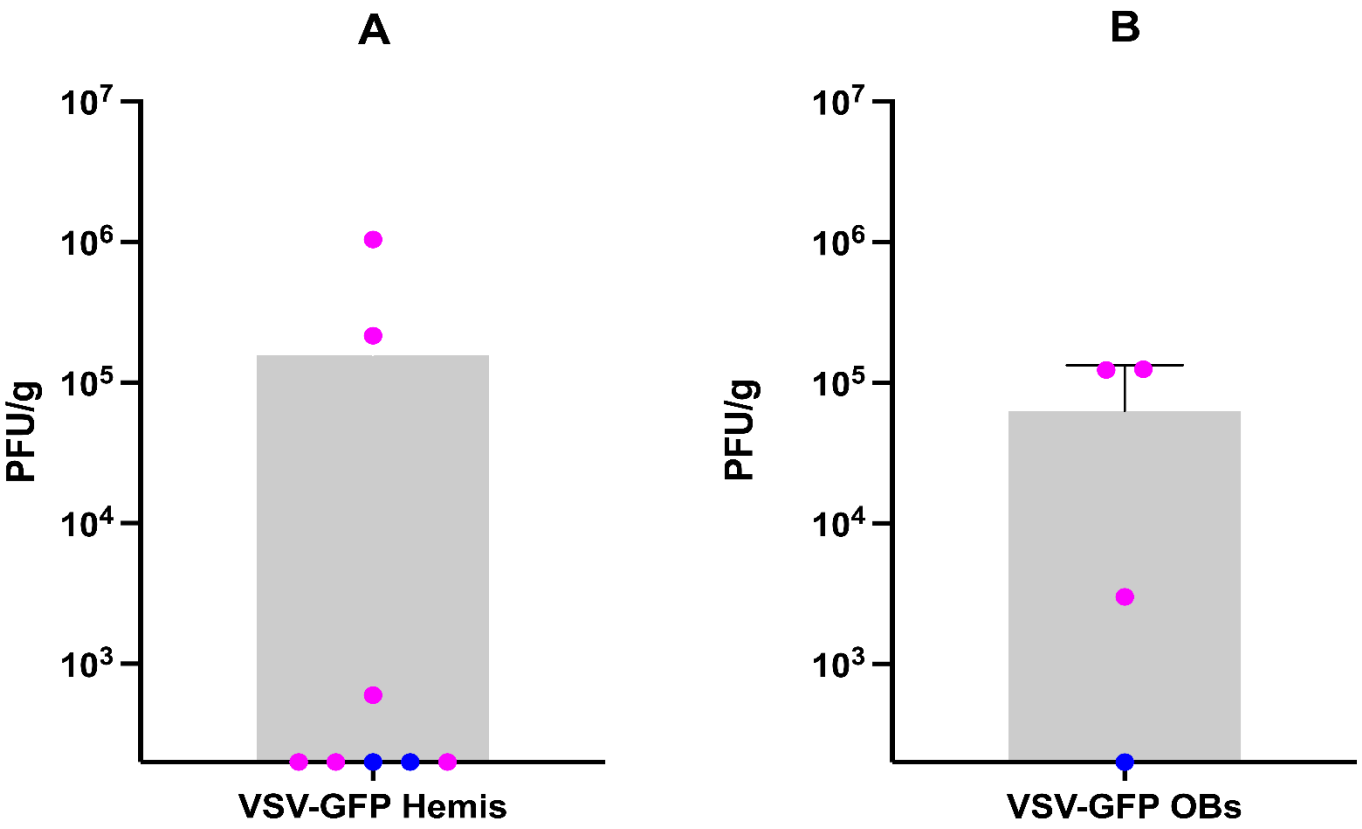

Figure 4: Outcome of Vesicular Stomatitis Virus Infection in Adult Wildtype Mice as Measured by Viral Load at Day 6 Post-inoculation. The viral load of mice infected with the Indiana serotype of VSV-GFP was measured by counting the plaque forming units 6 days post-inoculation in hemibrains (A) and olfactory bulbs (B) at serial dilutions, where each value represents the average of two technical replicates. Data points touching the X-axis constitute samples with no detectable viral titer. Error bars, when available, represent mean viral load ± SD. No analyses were performed on this dataset as different groups were not compared. Color code: magenta, females; blue, males.

As seen in **figure 5**, the olfactory bulbs of infected mice at 2DPI had a significantly higher viral titer than hindbrains of the same mice, congruent with the olfactory route being the main entry route of this virus into the brain and the most accessible given the nasal inoculation model used. The hemibrains of 2DPI mice, including the olfactory bulbs, showed a high viral titer averaging at 10^5 PFU/g, which is an elevation over the viral titer of the hemibrains of the 6DPI mice, where five out of eight samples were below the detectable viral threshold, and the hemibrains that formed plaques had a greatly variable PFU range. In contrast, not only the replication competent VSV-GFP was positive and detectable in all 2DPI hemibrain samples, but it also conveyed a tight range in regard to the viral concentration. Additionally, the viral concentration in the olfactory bulbs of the 6DPI mice was overall lower than the 2DPI group, and undetectable in one animal. The decrease in the overall viral titer, applicable to both olfactory bulbs and whole hemibrains, in 6DPIs versus 2DPI mice is an indication of effective clearance of the virus and an efficient ensuing immune response, both innate and adaptive (Bi et al., 1995), occurring between the 2- and 6DPI timepoints. Further, the unmistakably robust and range-compact viral concentration in the hindbrain of the 2DPI mice – consistent with staining in parts of the medulla at this early timepoint with IHC – supports the involvement of either the vagus nerve, the autonomic nervous system, the circularity system, or a combination of the aforementioned routes in transporting VSV-GFP into the hindbrain, constituting a secondary path of entry to bulb and olfactory route. It is unlikely that VSV-GFP reaches such distant parts of the brain from the olfactory epithelium and bulb in as little as 48 hours, especially when considering the lack of positive staining of viral proteins in the anatomical regions spanning from the olfactory bulb rostrally to the hindbrain caudally at 2DPI. This has also been confirmed in

studies that assessed the topographical infectivity and distribution of VSV in BALB/c mice infected with the same Indiana serotype (Huneycatt et al., 1994).

Plotting of previously assessed regions in a right-versus-left fashion was also performed and presented **in figure 6** to investigate a preference for VSV-GFP to infiltrate and infect anatomical structures or nuclei on one side of the mouse encephalon. There were no significant differences recorded when examining this effect in the olfactory bulbs and hindbrains of 2DPI mice as distinct regions, with both right and left samples displaying very similar PFU counts. The same applied to hemibrains of 2DPI, even with a bigger sample size than standalone bulbs and hindbrains, illustrating that such a preference for VSV-GFP for right- or left-brain structures and/ or routes does not exist, indeed, at this investigated timepoint.

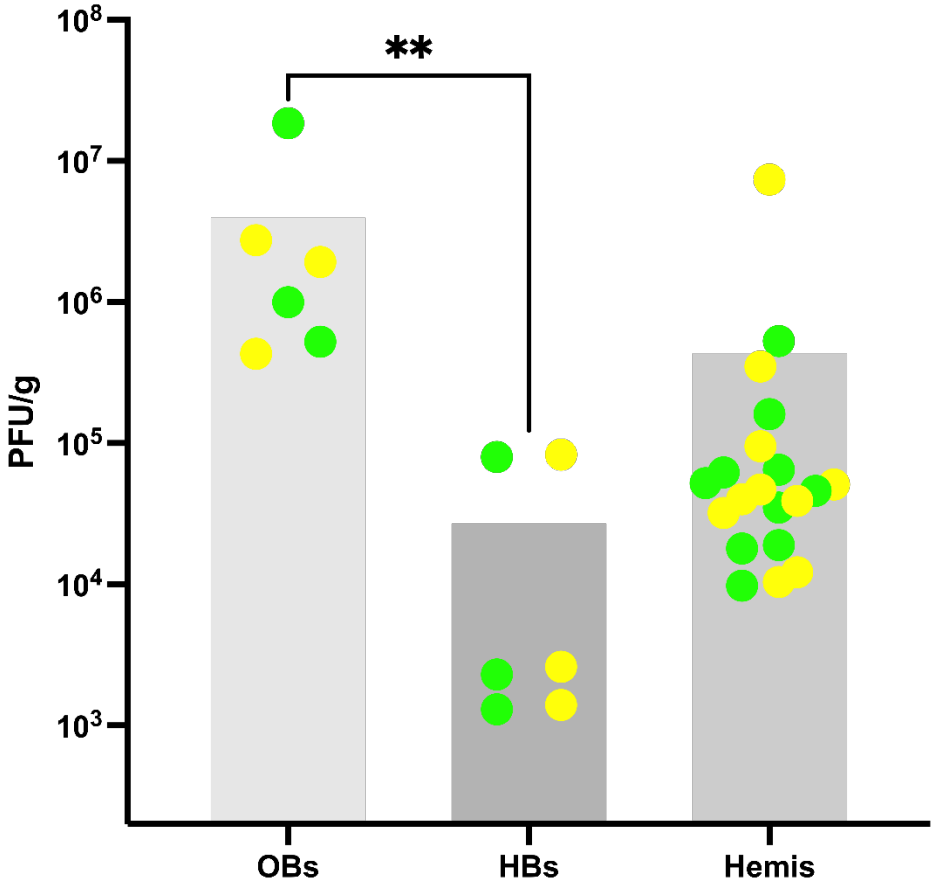

Figure 5: Outcome of Vesicular Stomatitis Virus Infection in Adult Wildtype Mice as Measured by Viral Load at Day 2 Post-inoculation in Distinct Anatomical Regions - Pooled. The viral load of mice infected with the wildtype, Indiana serotype of VSV-GFP was measured by counting the plaque forming units 2 days post-inoculation in olfactory bulbs in the left most column, hindbrains in the middle column, and whole hemibrains in the right most column, at a ranged series of dilutions, where each value represents the average of two technical replicates. Comparisons between the groups was made based on the regional difference in this dataset and not the assessed side (i.e., right vs. left). Data points touching the X-axis, if shown, constitute samples with no detectable viral titer. Error bars, when available, represent mean viral load ± SD. Mann Whitney test was used for statistical analysis between the OBs and HBs groups; two-tailed P value < 0.05 was considered significant. Color code: Green, right side; yellow, left side. All mice used in this cohort were females. OB: Olfactory Bulb, HB: Hindbrain, Hemi: Hemibrain.

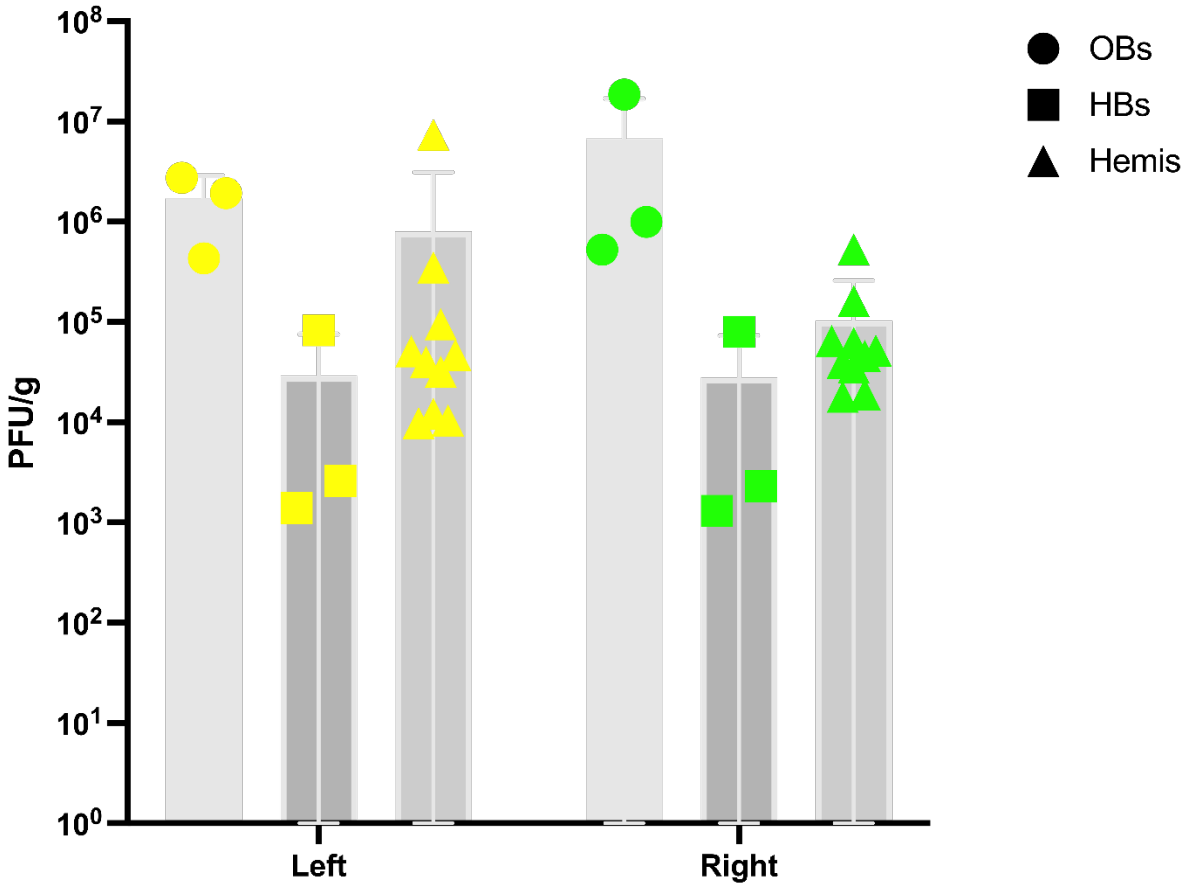

Figure 6: Outcome of Vesicular Stomatitis Virus Infection in Adult Wildtype Mice as Measured by Viral Load at Day 2 Post-inoculation in Distinct Anatomical Regions - Split.
The viral load of mice infected with the wildtype, Indiana serotype of VSV-GFP was measured by counting the plaque forming units 2 days post-inoculation in olfactory bulbs symbolized by a circle, hindbrains symbolized by a square, and whole hemibrains symbolized by a triangle, at a ranged series of dilutions, where each value represents the average of two technical replicates. Comparisons between the groups was made based on both the regional difference in this dataset and the assessed side (i.e., right vs. left), where each group represented by a column was compared to all the other. Data points touching the X-axis, if shown, constitute samples with no detectable viral titer. Error bars, when available, represent mean viral load ± SD.
Color code: Green, right side; yellow, left side. All mice used in this cohort were females. OB: Olfactory Bulb, HB: Hindbrain, Hemi: Hemibrain.

Glial Cell Characterization: Robust Reactivity in Infected Animals

The assessment of the immune response in infected and mock animals was carried out by means of reporting on the morphological state of spanning microglia and resident astrocytes in the mouse brain, characterizing changes of phenotype that these cells undergo in light of the introduced virus nasally. For that, sister sections of whole mounts of skulls were stained and developed via IHC using either anti-IBA1 or anti-GFAP antibodies, to detect microglia and astrocytes, respectively. The two sections selected for assessment per animal and per antibody were cut immediately after the sections processed for VSV-GFP staining, in a serial manner, making for an organized and consistent assessment across all animals, but also limiting the possibility of being too far off from the exact site or structure of infection and thus capturing immune cells that are not directly relevant to the infectious particles in site.

Immunohistochemical stains provided valuable insights into the shifting state of glia in the context of VSV-GFP infection; the staining patterns revealed the spatial distribution of microgliosis and astrogliosis, highlighting areas of viral replication and resultant inflammation within the brain. In addition to revealing the microglial and astroglial visual response, IHC stains also provided a helpful understanding of the correlation between activated microglia and astrocytes and the localization of the virus during the course of infection. The conjunction of VSV-GFP markers, the anti-IBA1, and anti-GFAP antibodies allowed for examining the spatial relationship between viral replication sites and the distribution of responding immune cells in the infected brain tissue, including the olfactory bulb and its immediate olfactory accessories. Experiments of this nature demonstrated a close association between regions of viral replication and the accumulation of activated microglia and astrocytes, suggesting that immune activation of these cells is influenced by the localization of the virus. Furthermore, it was observed,

qualitatively, that the degree of microglial activation varies depending on the viral load within specific brain regions, such as the subependymal layer in the olfactory bulb and the cerebellum of some mice. This observation suggests that the intensity of the immune response could be linked to the amount of virus present, highlighting the correlation between the viral burden and the extent of microglial activation, which constituted the rationale behind quantifying this immune response but specifically the phenotypical changes of those cells in the next section.

Phenotypical specific indicators of microglial activation and the transitioning into an M1 pro-inflammatory state from a resting a state were seen; this included an enlargement of cells' bodies, the adoption of an ameboid overall shape, retraction and thickening of processes, and a general proliferation of microglia that translated to an increased count. Such morphological changes were seen in several areas but were most striking in areas which revealed robust VSV-GFP+ staining in contrast with mock-treated mice. It is also worth mentioning that both the intensity of microglial staining and visual signs of activation appeared to correlate with the amount of viral staining. For example, mice showed variable VSV-GFP+ staining in the epithelium and glomerular layer, where mice exhibiting the more subtle and feeble VSV-GFP+ staining consequently displayed a weaker qualitative microglial response. The quantitative assessment of this qualitative observation was performed and is laid out in the next part.

All infected mice showed signs of microglial activation in the olfactory epithelium regardless of the sacrifice timepoint and even as late as 10DPI, albeit variable, which points to the then ongoing microglial inflammation even after both the resolving of the infection and the initiation of the interferon response against VSV protein starting at day 5PI (Bi et al., 1995), and the apparent decline of viral titers in the brains of infected mice at 6DPI (**A, E, I, M, and Q, figure 7**). Microglial cells in the epithelium appeared to be small, circular or rod-like shape, and dense

across all days, while microglia spotted along the CN-1 nerve bundles appeared to be more elongated and stretched out, both of which looked different from microglia observed in the olfactory bulb. The latter, in infected animals, appeared to adopt an irregular ameboid rounded shape, with thicker and generally shorter processes than their counterparts in uninfected animals. The signal intensity in the cell bodies of microglia also appeared to be higher, taking up more stain and seeming darker under the scope. These shape differences could very much be due to anatomical restrictions in regions observed in, such as the compaction of the stratified olfactory epithelium and the nature of the traversing longitudinal nerve fibers. The olfactory bulb, being a bigger structure, could allow for the typical characteristics of activated microglia – or microglia closely resembling the M1 phenotype – to emerge. This explanation is in agreement with studies reporting on different subtypes of microglia available within the brain, with each subtype displaying intrinsic properties and performing unique functions that are thought to be influenced by the anatomy and physiology of the structure it resides in (Li et al., 2022). This is the reason why both the M state and subtype classification should be considered when studying and profiling microglia exhaustively. In my project, the incorporation of the analysis of different local microglial subtypes was not necessary to characterize the VSV-GFP-influenced glial response, and instead, the studying of various microglial phenotypical and morphological changes that accompany activation, attributed to the plasticity of these cells, was favoured. Thus, and if microglia in the olfactory structures studied specifically belong to different subtypes and are heterogenous by nature, it is comprehensible that microglia will not all display the same changes – or not to the same extent at least – when studied in the context of activation and microgliosis.

The glomeruli showed the strongest IBA1+ staining on 6DPI (**J, figure 7**); the 2DPI group showed minimal reactivity compared to the mock group (not shown), increased considerably to the eye at 4DPI (**F, figure 7**) and appeared to have climaxed at 6DPI and began to drop afterwards as displayed by the 10DPI group (**Q, figure 7**). The inner layer of the olfactory bulb, and especially the granule and subependymal layers showed the greatest reactivity at 6DPI (**K, figure 7**) and to lesser extents on days 4- and 10PI (not shown). Other olfactory structures, such as the anterior olfactory nucleus (not shown), and the olfactory tubercle (**S, figure 7**) displayed signs of microgliosis on and after 6DPI. Other areas where VSV+ /GFP+ staining was seen were also imaged for microglia, incorporated into **figure 7**, and organized in a similar fashion to figure 2 for a direct visual comparison of VSV-GFP presence and the concurrent microglial state. These areas include the spinal nucleus of the trigeminal (**C, figure 7**), the spinal vestibular nucleus (**D, figure 7**), the CA2 hippocampal region (**G, figure 7**), the lateral vestibular nucleus (**H figure 7**), the cerebellum (**L, figure 7**), and the midbrain **(T, figure 7**). The visual reporting of microglia in those areas compared to the mock group suggested one or more signs of microgliosis discussed above. The quantitative assessment and detailed analysis, however, of microglia in the next section was limited to areas of interest in the anterior olfactory circuitry (the olfactory epithelium, the olfactory bulb, and the anterior olfactory nucleus), and a couple regions where VSV-GFP was seen in select animals (the cerebellum and the midbrain) as areas of reference.

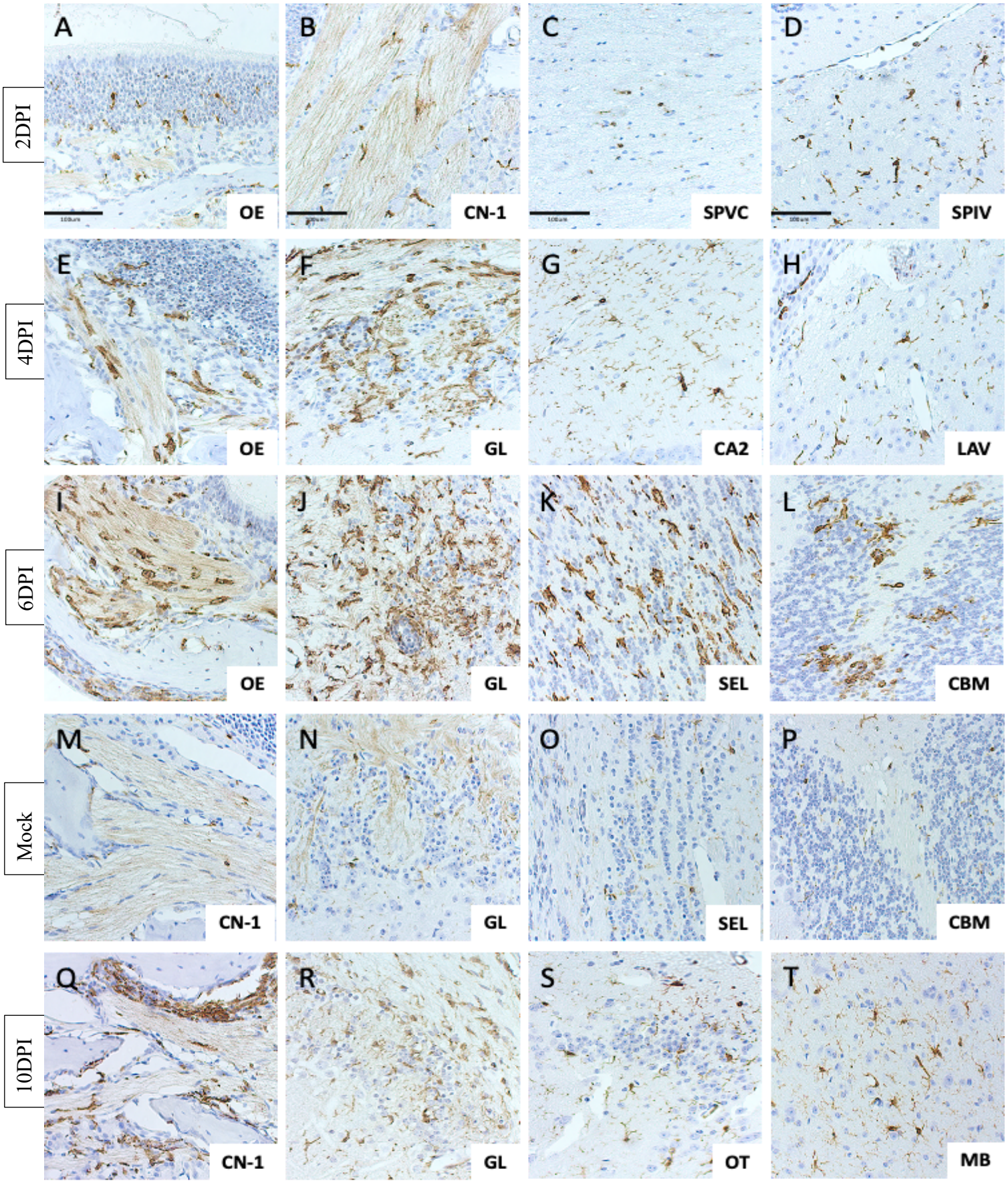
2DPI
A
OE
B
CN-1
C
SPVC
D
SPIV
4DPI
E
OE
F
GL
G
CA2
H
LAV
6DPI
I
OE
J
GL
K
SEL
L
CBM
Mock
M
CN-1
N
GL
O
SEL
P
CBM
10DPI
Q
CN-1
R
GL
S
OT
T
MB

Figure 7: Microglial Cells Display Phenotypical Changes Suggestive of Activation in Infected Mice. Immunohistochemistry (IHC)-based images illustrating the resultant immune response to VSV-GFP infection by resident microglia in whole head mounts of 2, 4, 6, and 10DPI mice. The response elicited by microglia and infiltrating macrophages was monitored using the ionized calcium binding adaptor molecule 1 (IBA1) antibody for the purposes of qualitatively visualizing and subsequently quantifying and analyzing the acute inflammatory response. Note the IBA1+ sheer staining in areas matched with VSV-GFP+ staining, where the amount of staining, but also the rounded and dense morphology of detected microglia, signifies an ongoing inflammation. OE: olfactory epithelium; CN-1: cranial nerve 1; SPVC: spinal nucleus of the trigeminal, caudal part; SPIV: spinal vestibular nucleus; GL: Glomeruli; CA2: Hippocampal region; LAV: lateral vestibular nucleus; SEL: Subependymal Layer; CBM: Cerebellum; OT: Olfactory Tract; MB: Midbrain. 2 sections were stained per (n) mouse, where n=21. Scale bar: 100um.

As with microglia, astrocytes in infected animals also displayed signs of astrocytic activation; a transformation from resting state to a reactive state, or a general shifting from the A2 anti-inflammatory phenotype to the A1 pro-inflammatory phenotype (Sofroniew, 2009; Liddelow et al., 2017). Phenotypical changes that normally accompany the transformation process are the hypertrophy of cellular bodies and extending processes towards the site of injury, resulting in bigger cells that span larger distances and connect with further away astrocytes. In some cases, astrocytes may also undergo proliferation to delineate the extent of the damage, leading to the formation of glial scars (Wang et al., 2018).

The overall shape of stained astrocytes across the cohort was consistent and similar to what is typically observed regardless of the region or structure imaged from. That is, however, not to say that there were no changes reflective of reactive transformation in infected animals. The olfactory epithelium was somewhat scarce in astrocyte in all animals – relative to other assessed areas – whether infected or not (**A, E, I, M, Q, figure 8**). On the other hand, the olfactory nerves were consistently labeled with anti-GFAP and picked up staining indicative of a baseline activity of astrocytes and presence of GFAP in those nerve bundles (**B, figure 8**, only 2DPI shown). Moreover, the staining was evidently stronger in infected animals and astrocytes were more prevalent compared to mock-treated mice, but with no clear distinction to the eye as to whether different groups had different levels or severities of astrocytic reactivity, which further necessitated the quantification of those immune cells in the next section. The glomerular layer of the bulb showed clear astrogliosis and robust staining on day 4- (**F, figure 8**) and especially day 6PI (**J, figure 8**), also congruent with the heightened microglial activity in those animals at those two timepoints.

Astrocytes are seen as decorating glomeruli, forming a sheath surrounding each glomerulus, along with periglomerular cells. In infected animals, most evident on days 4-,6-, and 10PI (**R, figure 8**), this circular sheath appeared more dense and the interconnection between surrounding astrocytes looked more discernible, giving select glomeruli in those sagittal sections the appearance of a disk with an ensheathing dark outlining.

The deeper layers of the olfactory bulb, including the mitral cell layer, the granule cell layer, and the subependymal layer exhibited an interesting sight of dystrophic astrocytes beyond day 4PI compared to mock-treated mice. It is understood in the literature that, under certain pathological conditions, astrocytes can undergo dystrophic changes; dystrophic astrocytes exhibit abnormal morphology and cellular features, including swollen or fragmented cell bodies (Ferrer., 2017; Guo et al., 2022), which is clearly seen in the subependymal layer of a 6DPI mouse when compared to the normal appearance of the astrocytes in the bulb of the mock (**K and O, figure 8**, respectively). This could be attributed to the disrupted neuronal communication and tissue homeostasis in the bulb due to the ongoing neuroinflammatory process. It was unclear, however, why the population of astrocytes past the glomerular layer and deeper into the bulb seemed to be the only one vulnerable to this dystrophic process.

Other olfactory structures, such as the anterior olfactory nucleus (not shown), and the olfactory tubercle (**S, figure 8**) displayed signs of astrogliosis on and after 6DPI. Other areas where VSV+ /GFP+ staining was seen were also imaged for astrocytes, incorporated into **figure 8**, and organized in a similar fashion to **figure 2** for a direct visual comparison of VSV-GFP presence and the concurrent astroglial reactivity. These areas included the spinal nucleus of the trigeminal (**C, figure 8**), the spinal vestibular nucleus (**D, figure 8**), the CA2 hippocampal region (**G, figure 8**), the lateral vestibular nucleus (**H, figure 8**), the cerebellum (**L, figure 8**), and the

midbrain (**T, figure 8**). The visual assessment of astrocytes in those areas compared to mock-treated mice suggested one or more signs of astrogliosis discussed above. The quantitative assessment and detailed analysis, however, of astrocytes in the next section was limited to areas of interest in the anterior olfactory circuitry (the olfactory epithelium, the olfactory bulb and the anterior olfactory nucleus), and those regions where VSV-GFP was seen in select animals, namely the cerebellum and the midbrain, as areas of reference.

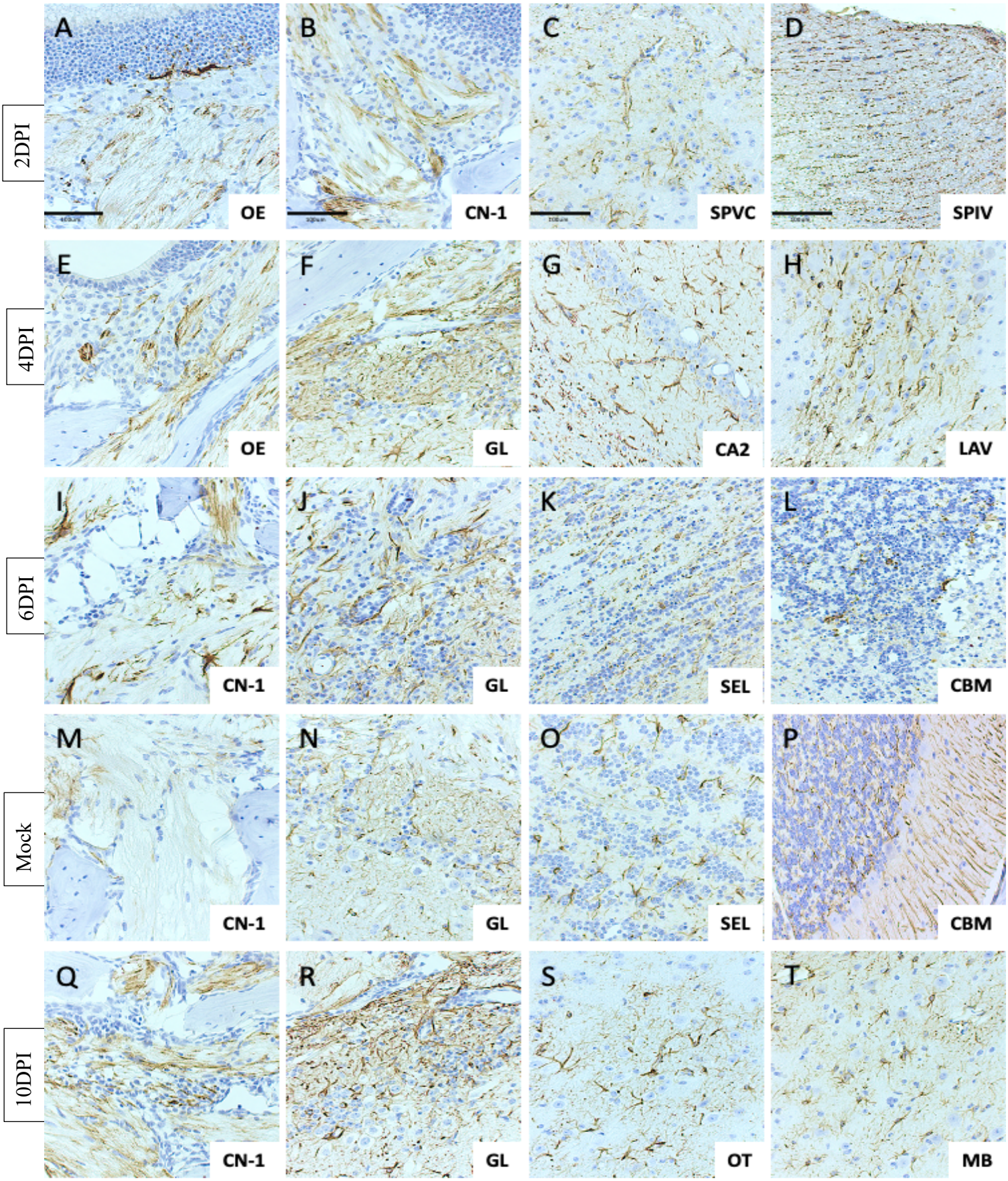
2DPI
4DPI
6DPI
Mock
10DPI
A
OE
B
CN-1
C
SPVC
D
SPIV
E
OE
F
GL
G
CA2
H
LAV
I
CN-1
J
GL
K
SEL
L
CBM
M
CN-1
N
GL
O
SEL
P
CBM
Q
CN-1
R
GL
S
OT
T
MB

Figure 8: Astrocytes Display Phenotypical Alterations Suggestive of Activation in Infected Mice. Immunohistochemistry (IHC)-based images illustrating resultant immune response to VSV-GFP infection by local astrocytic cells in whole head mounts of 2, 4, 6, and 10DPI mice. The response elicited by local astrocytes was monitored using the glial fibrillary acidic protein (GFAP) antibody for the purpose of qualitatively visualizing the acute inflammatory response and preparing sections for subsequent quantitative analyses. Note the GFAP+ sheer staining in areas matched with VSV-GFP+ staining, where the amount of staining, but also the slightly bigger body size and increased cellular perimeter signifies an ongoing inflammation. OE: olfactory epithelium; CN-1: cranial nerve 1; SPVC: spinal nucleus of the trigeminal, caudal part; SPIV: spinal vestibular nucleus; GL: Glomeruli; CA2: Hippocampal region; LAV: lateral vestibular nucleus; SEL: Subependymal Layer; CBM: Cerebellum; OT: Olfactory Tract; MB: Midbrain. 2 sections were stained per (n) mouse, where n=21. Scale bar: 100um.

Glial Cell Quantification: Phenotypical Changes Reveal an Inflammatory State

The criterion used for quantifying immune-cell signal was established, devised, and compiled by me, with clarification on some aspects of the program used offered by the CBIA core (Faculty of Medicine, University of Ottawa), and some basic functions explained in simple terms in the online-available tutorial by Kristopher Kubow (2019). A step-by-step demonstration of the criterion is available in the Appendix.

Areas of interest for quantification of microglia and astrocytes comprised key anterior olfactory structures, such as the olfactory epithelium (OE), olfactory bulb (OB), and anterior olfactory nucleus (AON), where extensive viral reactivity with immunohistochemical stains was recorded. As mentioned, the cerebellum, which is notably an area where VSV breaches and spread as noted in the literature (Huneycutt et al., 1994), also seen in a couple 6DPI mice in my cohort, and the midbrain, as an area of reference, but also due to the fact that it includes the SNpc and its direct link to the pathogenesis of PD (Fearnley and Lees, 1991; Lehéricy et al., 2012; Vaillancourt and Mitchell, 2020), making it an exceedingly relevant area, were included in the quantifications and analysis of the main cohort. The findings were compared and standardized to the mock group of the same cohort before making any conclusions.

The morphological characteristics deemed suitable for the assessment for microglia included the cellular body size (comprising the spanning-out processes), the infiltration of microglia and macrophages indicated by the percent staining of IBA1+ in each area after standardizing to the mock group, as well as the average circularity and solidity of local microglia in the analyzed selection. The rationale behind the choice of these parameters being the numerous reports on the morphological changes associated with a shift towards an M1pro-inflammatory state of microglial cells. It has been shown that microglia, in response to CNS

injury or pathogenic assaults, adopt a bigger, more rounded or ameboid-like solid morphology, where individual reactive cells retract their processes and present thicker ones, and proliferate as part of the microgliosis and ongoing inflammation to control the infection (Fernández-Arjona et al., 2017; Heindl et al., 2018).

For astrocytes, the parameters chosen were the relative body size, the percent of GFAP+ staining in each area standardized to mock sections, and the perimeter, where the latter is defined as the length of a geometric line engulfing the cell body and its processes. Studies have not only shown these parameters to increase in the context of CNS-related injury or pathogen-induced inflammation, but also to increase in a semi-direct proportional manner to the severity of insult or injury, warranting for a reactive astroglial state and an astrogliosis where the neuronal and cellular homeostasis has been disturbed (Wilhelmsson et al., 2006; Escartin et al., 2021).

Starting with olfactory structures, the measurement of the body size of microglia showed a significant increase in all infected animals at all timepoints compared to mock-treated mice, with the 6DPI group showing the highest measurements in all three areas. The increase in size could be described as acute, where a significant hike in microglial size was seen as soon as day 2PI – except for the deeper anterior olfactory nucleus – that kept increasing steadily till it reached what seemed to be the 'climax' or its highest point. The microglial size dropped slightly in the olfactory epithelium and olfactory bulb on day 10PI and significantly in the anterior olfactory nucleus at that timepoint (**A, E, and I, figure 9**). The percent of the area occupied by the IBA1+ signal, after being standardized to the area percent in mock animals, also climbed up significantly in infected mice. It is interesting to note that the significance of increase was robust as soon as 2DPI in the olfactory epithelium (**B, figure 9**), less so in the olfactory bulb of the same timepoint (**F, figure 9**), and was not significantly different in the anterior olfactory nucleus

at this timepoint (**J, figure 9**). This alludes to the proliferation of microglia that is influenced by the presence and infiltration of VSV-GFP, considering how there was heavy VSV-GFP staining in the epithelium at day 2PI evident by IHC, little-to-staining in the bulb, and no positive staining observed in the anterior olfactory nucleus this early in the infectious course. The area percent occupied, like the relative size, seemed to reach its highest value at 6DPI in all areas and decreased at the latest measured timepoint, where the difference between the IBA1+ signal occupation in infected and mock-treated mice becomes insignificantly different at 10DPI in the epithelium. This likely hints at the resolved infected in the olfactory epithelium at this timepoint and the shifting of microglia back towards the M2 anti-inflammatory state. The circularity and solidity values of sampled microglia from the olfactory epithelium and anterior olfactory nucleus seemed to follow a similar trend of increase starting at 2DPI and reaching an all-time high at 6DPI, where a minimal drop in measured values was witnessed afterwards at 10DPI (**D and L, figure 9**). Surprisingly, the measured values of the aforementioned two parameters of resident microglia in the olfactory bulb fluctuate in both directions, recording lower or higher values than mock animals (i.e., less or more circular, **G, figure 9**; less dense or denser, **H, figure 9**). No significance or an apparent trend was seen with the circularity or density parameters of microglia in the olfactory bulb, which could be attributed to either different intrinsic microglial subtypes local to the olfactory bulb, thus displaying different morphological characteristics in response to a neurotropic infection, or simply the sampling area of the olfactory bulb being too big, resulting in the inclusion of microglia that are far off from where VSV-GFP was replicating, and hence did not receive the cue to transform via the various signaling pathways.

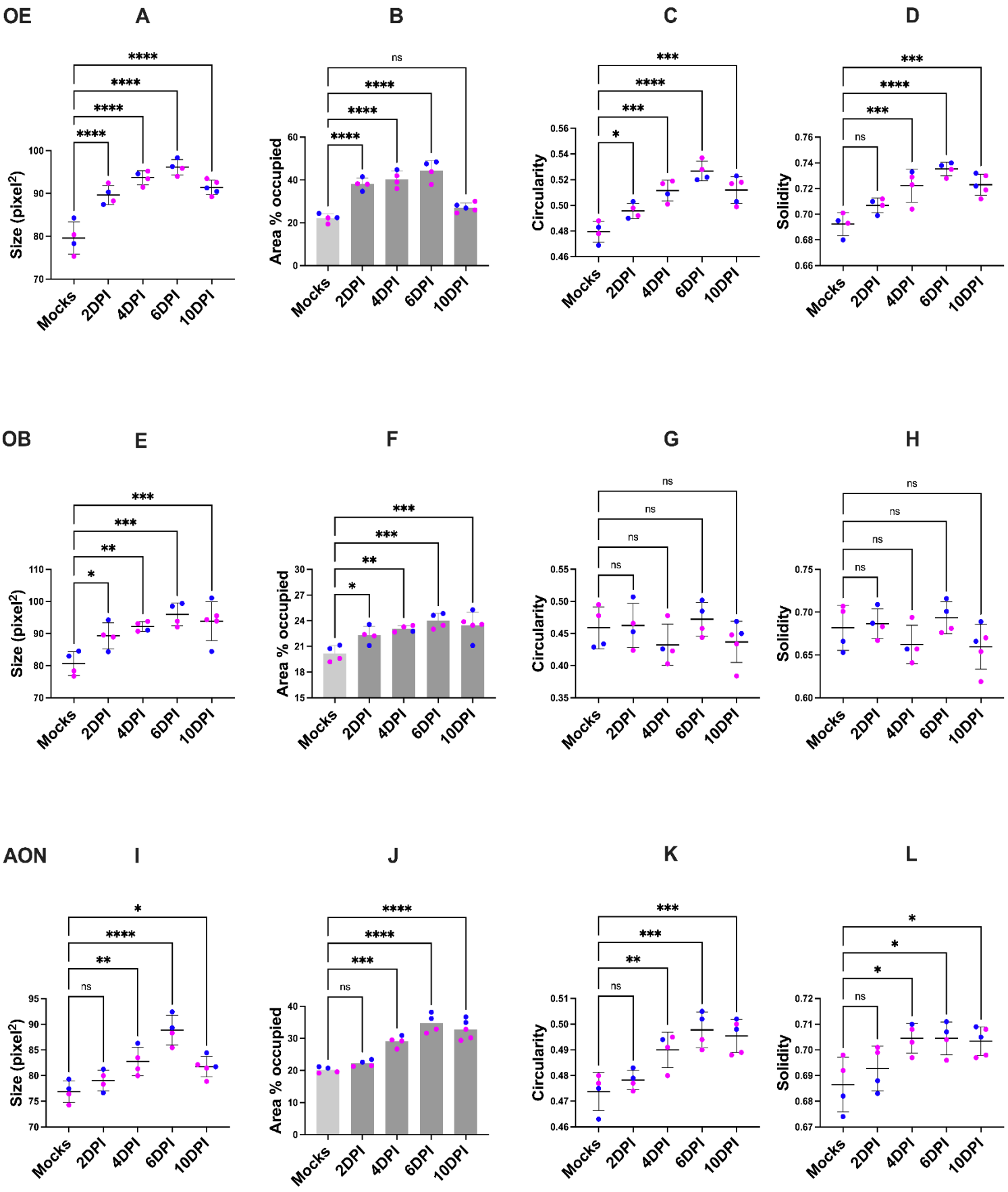
OE
A
B
C
D
OB
E
F
G
H
AON
I
J
K
L
Size (pixel²)
Area % occupied
Circularity
Solidity
Mocks
2DPI
4DPI
6DPI
10DPI
ns

Figure 9: Quantifications of Microglial Phenotypical Parameters in the Rostral Olfactory Structures of Infected Mice Reveal Changes Indicates Activation of those Glial Cells (A-D) Quantifications of microglia from the olfactory epithelium, (E-H) olfactory bulb, and (I-L) anterior olfactory nucleus of all mice belonging to the main cohort, where each data point represents the average of two measurements of the same area selection from two sister section belonging to the same animal. Error bars, when available, represent mean of measurements per group ± SD. Ordinary one-way ANOVA was used for statistical analysis between each of the timepoint groups and mock-treated mice, where P value <0.05 was considered significant. Color code: blue, males; magenta, females. OE: Olfactory Epithelium; OB: Olfactory Bulb; AON: Anterior Olfactory Nucleus.

A gradient analysis was performed on representative sections from animals that clearly showed viral staining in one or more of the glomeruli in the glomerular layer (one animal per timepoint group). This analysis was performed on four different levels identified in **table 8** in the appendix, with the aim of looking for more distinct microglial alterations of the measured parameters, especially circularity and solidity, in the glomerulus directly impacted by VSV-GFP and gradually increasing the selected area in fixed selection intervals to track the shifting of those measurements in the immediate but also farther-out areas adjacent to the infected glomerulus initially selected. Gradient analysis of the size, circularity, and solidity showed the highest values of microglia recorded at level 1and the lowest at level 4, which included microglia distant from the very area of viral impact (**figure 10**). The 6DPI animals were analyzed, and in congruency with the quantification performed on the entire cohort of the size parameter, their sections showed the highest values of all animals analyzed belonging to other timepoints. The spike in circularity and solidity parameters from microglia closest the VSV-GFP staining and in infected microglia indicates that a shifting to the M1 pro-inflammatory state, including an increase in cell size, retraction of processes and adoption of a rounder shape, denser interior, occurred to microglia that were in closest proximity to the virus.

A

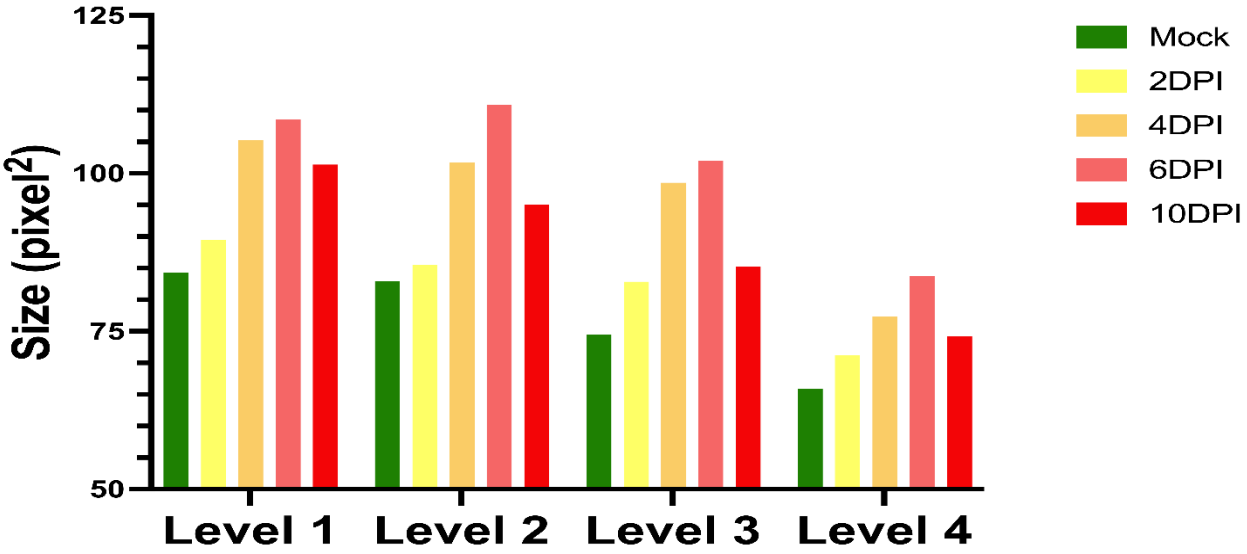
125
100
75
50
Size (pixel²)
Level 1
Level 2
Level 3
Level 4
Mock
2DPI
4DPI
6DPI
10DPI

B

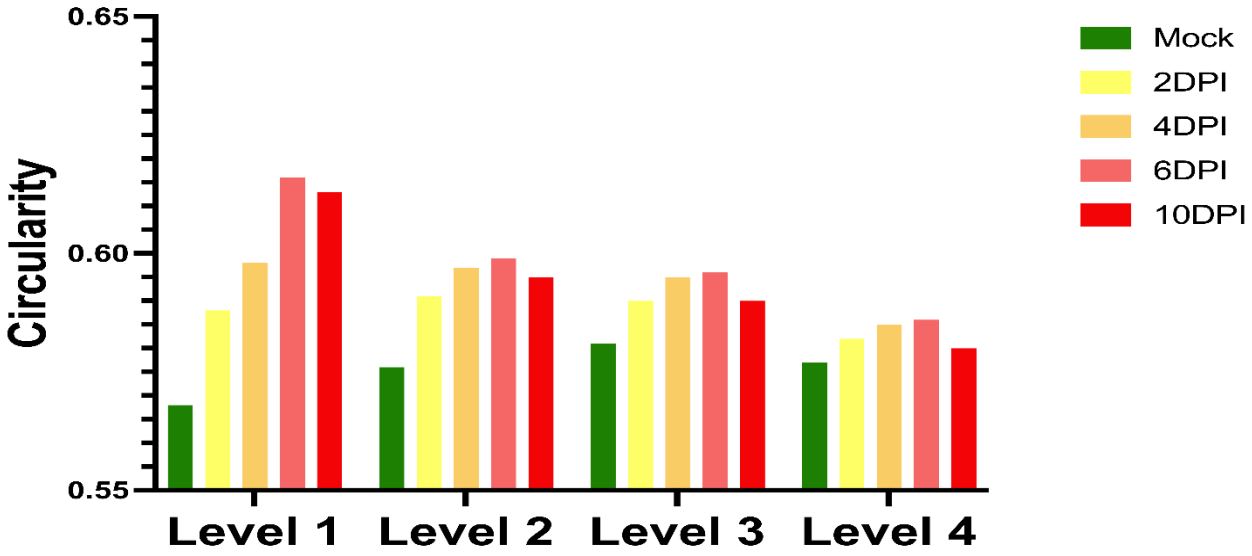
0.65
0.60
0.55
Circularity
Level 1
Level 2
Level 3
Level 4
Mock
2DPI
4DPI
6DPI
10DPI

C

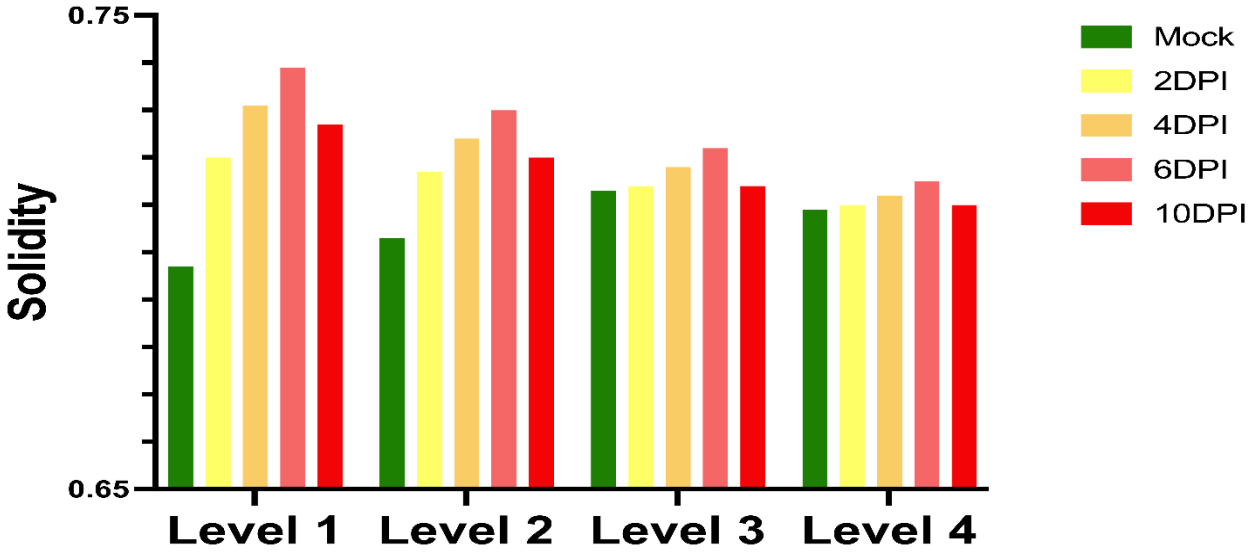
0.75
0.65
Solidity
Level 1
Level 2
Level 3
Level 4
Mock
2DPI
4DPI
6DPI
10DPI

Figure 10: Gradient Analysis of Infected Glomeruli and Proximal Layers of the Olfactory Bulb Displays a Phenotypical Shift in Measured Microglial Parameters in Cells Closest to the Viral Entry Site. The differences seen in the quantified parameters between distinct timepoints appear to be the greatest at Level 1 (virally impacted glomerulus) and decrease gradually as Level 4 (larger selection including deeper layers of the olfactory bulb) is reached. This helps explain the insignificant and fluctuating circularity and solidity measures in the olfactory bulb, which could be influenced by both the heterogeneity of available cell populations in this relatively big area, but also the different state of activation of microglia according to their proximity to infected and virus-housing glomeruli. Each bar represents the average of measurements of 10 different and randomly selected cells. No statistical analysis was performed on this data set.

When analyzing the chosen areas of reference, namely the cerebellum and the midbrain, phenotypical differences were less striking overall. In the cerebellum, a trend of increase was noticed in both the body size and the percent of area occupied by the IBA1+ signal, with those two parameters recording higher values as soon as 2DPI and then plateauing until they drop again at 10DPI (**A and B, figure 11**). This is a little surprising given that VSV+ staining was not seen in the cerebellum prior to 6DPI and is not reported in the literature to venture into the cerebellum before that timepoint either (Huneycutt et al., 1994). It is also worth noting that the two 6DPI animals that showed VSV-GFP+ staining in the cerebellum (**A and B, figure 11**, both males, in blue) showed the highest recorded levels of those two parameters in their group timepoint, with one of them appearing to have the biggest body size in the entire cohort. The circularity and density, however, are insignificantly different, and do not appear to follow either a decrease or increase trend, even for the two male mice of the 6DPI group discussed for the clear impact of VSV-GFP in the cerebellum (**C and D, figure 11**). This could be, similar to what was observed in the olfactory bulb, due to the sampling of the large area of the cerebellum consisting of the three main lobes rather than the one lobe that revealed VSV-GFP+ staining. The selection of the entire cerebellum initially was meant to capture any changes in any of the lobes, rather than limiting it to the anatomical area of the cerebellum where reactivity via IHC was seen.

When the midbrain of the brainstem was selected and quantified for those microglial phenotypical parameters, there appeared to be a significant increase in body size in both days 4- and 6PI that dropped later at 10DPI to levels comparable to that of mock-treated mice (**E, figure 11**). This might indicate that by 10DPI, the infection had been resolved by the immune response and put at bay, and the 10DPI staining of VSV-GFP+ seen via IHC in areas like the substantia

nigra of the midbrain represents residual VSV-GFP proteins that are not replicate-competent or infectious. The area occupied by the IBA1+ signal increased steadily from the 2- to the 6DPI group, albeit insignificantly, and dropped at 10DPI to about the same percent as the mock group (**F, figure 11**). This might indicate a localized proliferation of microglia and microgliosis in specific parts of the midbrain instead of a systemic response throughout the entire mesencephalon. The circularity and solidity parameters from the midbrain did not match the inflammatory profiles indicated by the cell body size and percent of signal occupation observed on days 4- and 6PI especially; the circularity and solidity values fluctuated and appeared to drop compared to mock-treated mice on the aforementioned timepoints, adopting a more irregular shape (**G and H, figure 11**). This could, once again, be attributed to the sampling of the entire midbrain, which is a large anatomical structure, and hence the inclusion of rather more diverse populations of microglia, namely ones that are quiescent and have not received the signal to transform into the activated state.

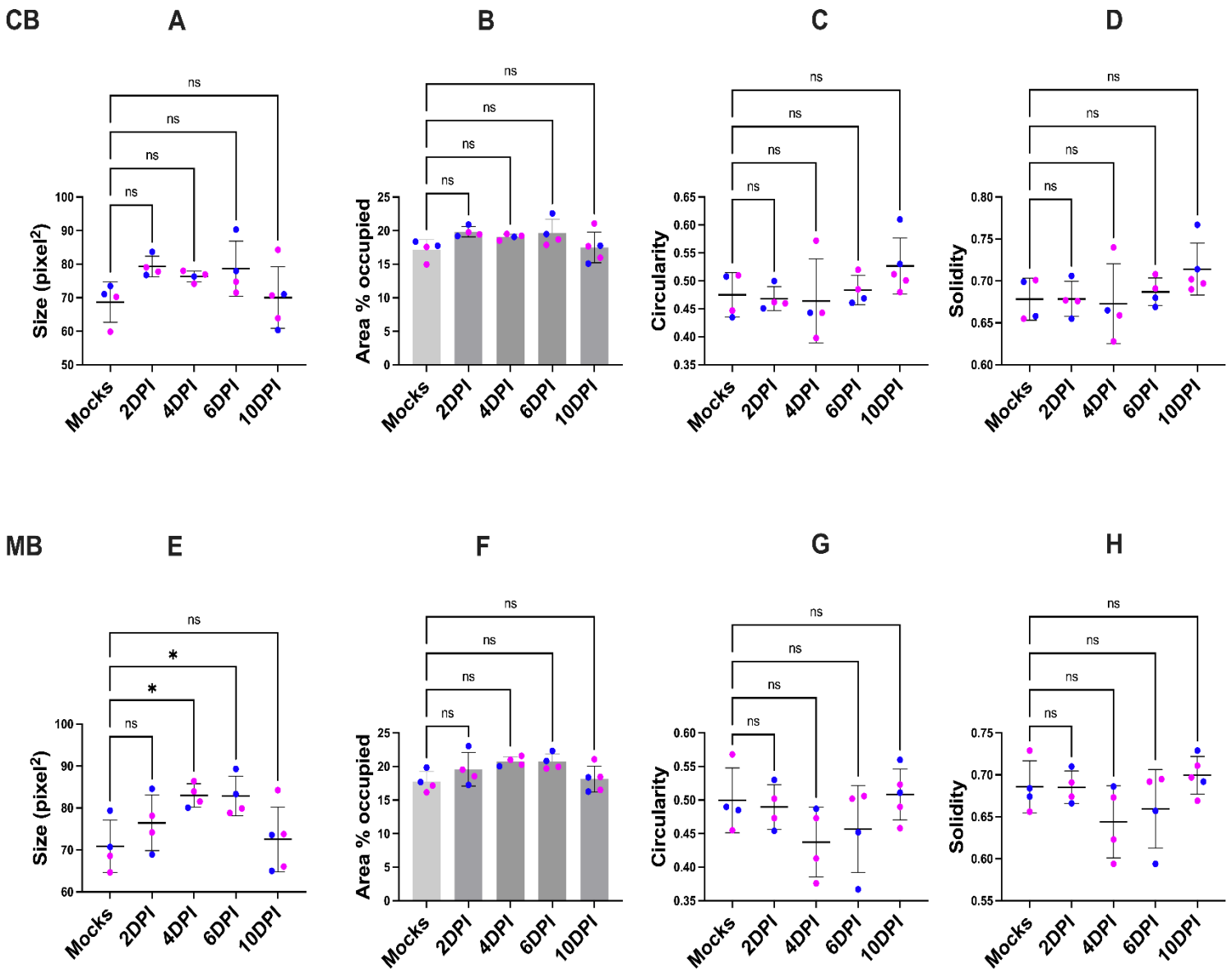

Figure 11: Quantifications of Microglia-Specific Phenotypical Parameters in the Cerebellum and Midbrain of Infected Mice Suggest Activation of those Glial Cells. (A-D) Quantifications of microglia from the cerebellum and (E-H) midbrain of all mice belonging to the main cohort, where each data point represents the average of two measurements of the same area selection from two sister section belonging to the same animal. Error bars, when available, represent mean of measurements per group ± SD. Ordinary one-way ANOVA was used for statistical analysis between each of the timepoint groups and mock-treated animals, where P value <0.05 was considered significant. Color code: blue, males; magenta, females. CB: Cerebellum; MB: Midbrain.

The quantification of astrocytes focused on the body size, the percent of GFAP+ occupation standardized to the mock group, and the perimeter only. This is because the circularity and solidity are not phenotypical alternations known to be linked to different physiological states of astrocytes (Yu et al., 2012; Ben Haim et al., 2015). In the olfactory epithelium, all three parameters displayed an increasing trend starting as early as 2DPI, where recorded values climbed steadily to reach the highest on 10DPI (**A, B, and C, figure 12**). While the body size and perimeter of cells were not significantly different prior to 6DPI, the area percent occupied by GFAP+ was significantly increased at the earlier 4DPI timepoint. This alludes to the overexpression of GFAP by astrocytes, which is linked to the proliferation of astrocytes and the extension of processes (Yang and Wang, 2016). Similarly in the anterior olfactory nucleus, there was a steady trend of increase in all three parameters that started on day 2PI but only reached significance on 6DPI and especially the 10DPI, where the latter timepoint group revealed striking differences in both the body size and perimeter compared to mock-treated mice (**G, H, and I, figure 12**). The shallow increase in measured parameters at 2- and 4DPI that did not reach significance could be attributed to the fact that VSV does not typically venture deep into the anterior olfactory nucleus early on in the infectious course, as described in the viral staining section and in the literature (Huneycutt et al., 1994) but is reflected in spiked up measurements at later timepoints. Interestingly, measurements from the olfactory bulb of infected mice displayed significant differences of bigger values as early as 2DPI (**D, E, and F, figure 12**), although the olfactory bulb as a structure itself is not the first to be impacted by the nasal inoculation of VSV-GFP. This may be caused by local astrocytes to the bulb receiving signaling cues from the olfactory epithelium through the traversing nerve bundles and the shared parenchyma, even when the virus has not made its way into the bulb yet, inducing a reactive

state in those astrocytes that could be described as acute. Alternatively, it could be attributed to different subtypes of astrocytes local to each area quantified from that exert different functions (Sofroniew, 2020). Nonetheless, the steady increase observed in the olfactory epithelium and anterior olfactory nucleus was consistent in the olfactory bulb as well, with reported values seeming to have reached an all-time high at 10DPI. This trajectory of astroglial reactivity is in contrast with microglial activation that tends to start to revert back to normal physiological values past 6DPI in analyzed olfactory structures.

In the cerebellum, significant increases in astroglial size, percent occupation by GFAP+ signal, and perimeter were seen as early as 2- and 4DPI (**A, B, C, figure 13**). On par with assessed olfactory structures, measurements of parameters returned the highest values at 10DPI, signifying a reactive astrogliosis that might still be taking place even after the potential resolve and clearance of active virus in the cerebellum at 10DPI. In the midbrain, however, those very parameters only reached a difference of significance – that is an increase – on day 10PI, with other timepoints fluctuating in a non-significant manner above the calculated average of the mock group (**D, E, and F, figure 13**). Based on these observations, it was conceivable that, since the virus does not visibly propagate in midbrain structures, such as the SNpc for instance, at or before 6DPI, astrocytes as a result do not display morphological or phenotypical changes indicative of an astrogliosis. Taken together, it appeared that astrocytes' reactivity or the general shifting into reactive gliosis in areas assessed was potentially influenced by more than solely positive VSV-GFP staining, such as the olfactory bulb and cerebellum, where no reactivity of viral antigens was seen via IHC in those areas at 2DPI for example, yet a significant hike in quantified astrocytic parameters was recorded.

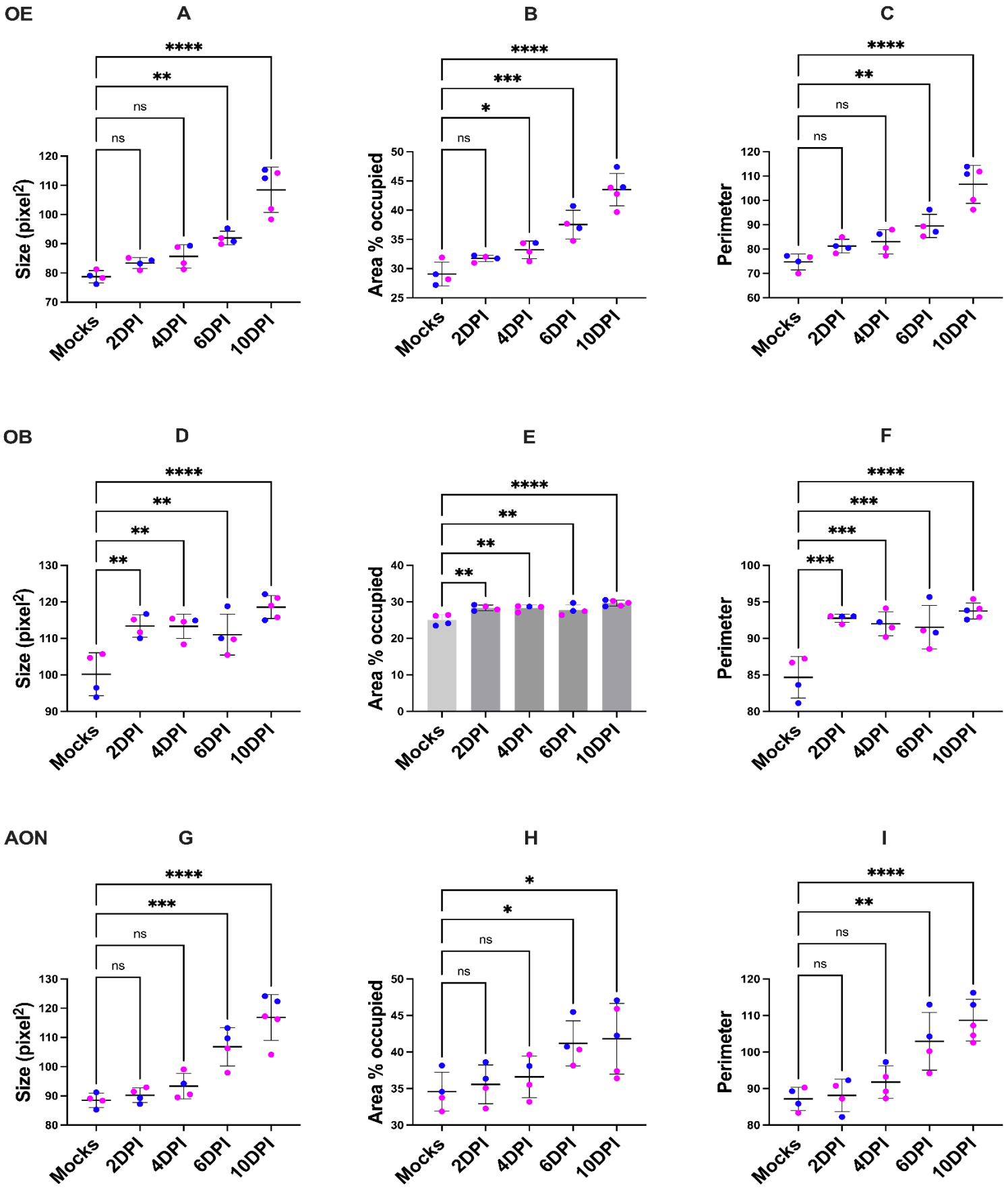
OE
A
B
C
OB
D
E
F
AON
G
H
I
Size (pixel²)
Area % occupied
Perimeter
Mocks
2DPI
4DPI
6DPI
10DPI
ns
*
**
***
****

Figure 12: Quantifications of Astroglia-Specific Phenotypical Parameters in Rostral Olfactory Structures of Infected Mice Suggest Astrocytic Activation. (A-C) Quantifications of astrocytes from the olfactory epithelium, (D-F) olfactory bulb, and (G-I) anterior olfactory nucleus in all mice belonging to the main cohort, where each data point represents the average of two measurements of the same area selection from two sister section belonging to the same animal. Error bars, when available, represent mean of measurements per group ± SD. Ordinary one-way ANOVA was used for statistical analysis between each of the timepoint groups and mock-treated animals, where P value <0.05 was considered significant. Color code: blue, males; magenta, females. OE: Olfactory Epithelium; OB: Olfactory Bulb; AON: Anterior Olfactory Nucleus.

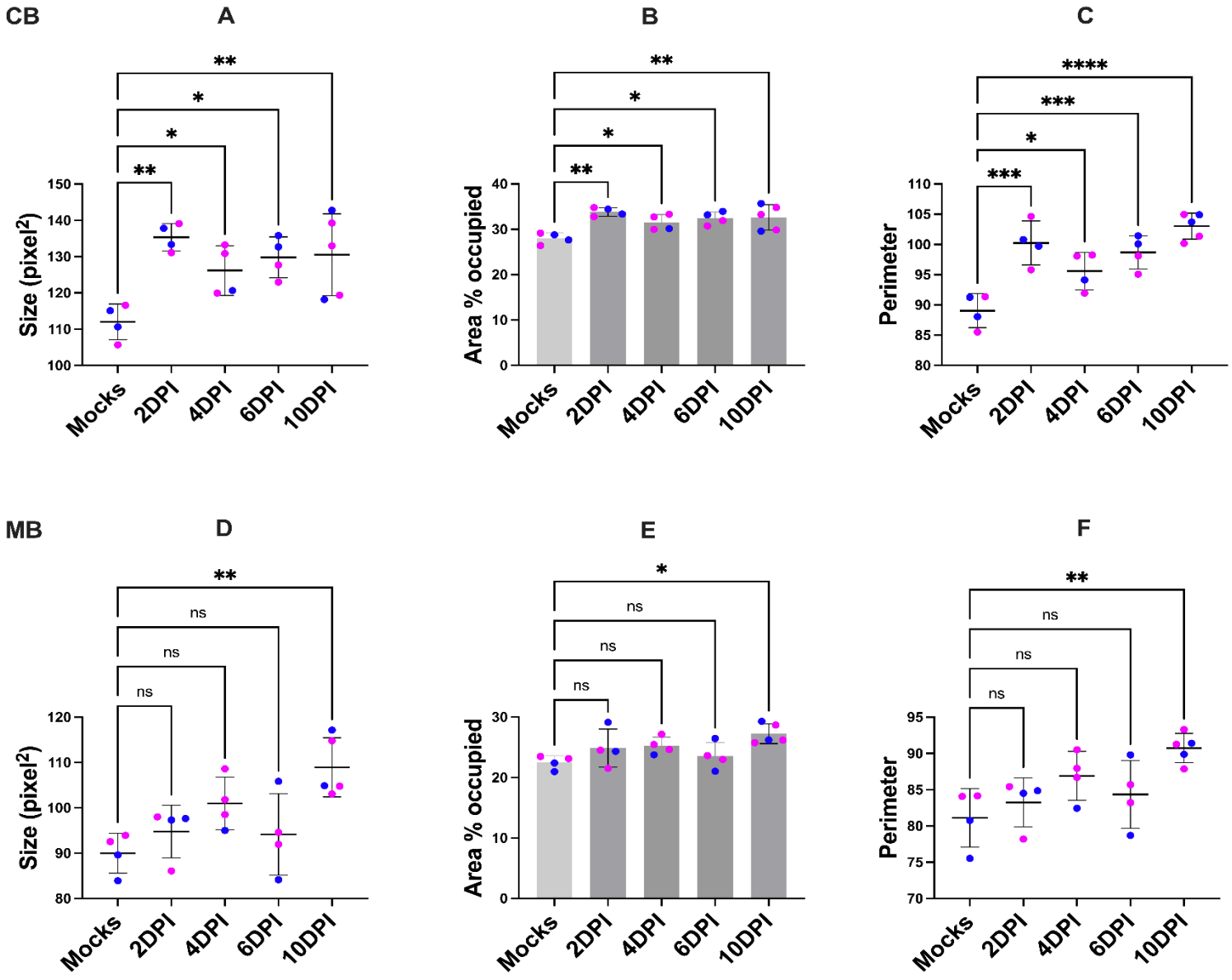

Figure 13: Quantifications of Astroglia-Specific Phenotypical Parameters in the Cerebellum and Midbrain of Infected Mice Suggest Activation of those Glial Cells. (A-C) Quantifications of astrocytes from the cerebellum and (D-F) midbrain of all mice belonging to the main cohort, where each data point represents the average of two measurements of the same area selection from two sister section belonging to the same animal. Error bars, when available, represent mean of measurements per group ± SD. Ordinary one-way ANOVA was used for statistical analysis between each of the timepoint groups and mock-treated animals, where P value <0.05 was considered significant. Color code: blue, males; magenta, females. CB: Cerebellum; MB: Midbrain.

Endogenous Wildtype Mouse α-Synuclein is Prevalent in Anterior Olfactory Structures

α-Synuclein, being a presynaptic protein primarily, has been reported to be widespread and expressed in several regions of the mouse brain, with the highest levels observed in certain structures; the substantia nigra, a region involved in motor control, contains a particularly high concentration of α-synuclein (Taguchi et al., 2019). This protein is primarily localized within SNpc neurons, which play a crucial role in the regulation of movement (Mak et al., 2009). Another region where α-synuclein is highly expressed is the hippocampus, which is essential for learning and memory processes (Taguchi et al., 2014). It is also found in the cerebral cortex, striatum, thalamus, and hypothalamus, among other brain regions, such as the granule cell layer of the cerebellum (Lein et al., 2007; Taguchi et al., 2019). The specific distribution of α-synuclein in these areas suggests its involvement in various physiological functions, including neuronal communication, synaptic function, and neurotransmitter release, while its accumulation or aggregation has been linked to neurodegenerative diseases. Within the olfactory bulb, α-synuclein is observed in several regions, including the glomerular layer, mitral cell layer, and granule cell layer (Ubeda-beñon et al., 2010; Killinger et al., 2023). In the glomerular layer, it is found in the presynaptic terminals of the olfactory sensory neurons, forming connections with mitral and tufted cells. This localization suggests a contribution to the transmission and processing of olfactory information in the mouse olfactory system. It has been shown by our lab, utilizing the holocranohistochemistry technique, that α-synuclein is an abundant constituent within the olfactory epithelium and is primarily located in olfactory sensory neurons, which are responsible for detecting and transmitting odor signals, amongst other cells (Tomlinson et al., 2017). It is particularly concentrated in the nerve terminals of these neurons, where it has long

been proposed to play a role in regulating neurotransmitter release (Bellani et al., 2010; Burré, 2015).

This was replicated in my project via the routine immunohistochemistry staining for α-synuclein in the wildtype brains of mice, both mock and infected, to investigate any qualitative or visual differences in the expression pattern of the unfolded, monomeric α-synuclein in the olfactory epithelium and olfactory bulb and confirm its distribution once again. This was accomplished using the Syn-1 antibody, a commercially available antibody that recognizes mouse, rat, and human wildtype α-synuclein. In accordance with previous work done by Megan Fitzpatrick from our lab and work published by Tomlinson et al., (2017), the expression of α-synuclein in wildtype animals was abundant throughout the brain and similar to what is reported in literature (Li et al., 2002). In anterior olfactory structures, however, as seen in **figure 14**, the expression of α-synuclein appeared to be consistently localized to olfactory sensory neurons in the olfactory epithelium, but also supporting cells and basal progenitor cells in 2- and 6DPI animals (**A and B**, respectively) and mock-treated mice (**C**), both to similar extents. The overall staining observed in the epithelium struck as being a mixture of cytoplasmic and nuclear staining, with dendritic knobs extending to the surface of the epithelium, where the cilia was positively labeled as well. The axonal terminals of olfactory sensory neurons, which come together to form the olfactory nerve bundles or CN-1, were also positively stained (**B**, labeled). These olfactory nerves, upon traveling across the cribriform plate, synapse with dendrites from mitral, tufted, and periglomerular cells surrounding the glomeruli of the bulb (**D**, arrow heads). In the bulb, the expression pattern of α-synuclein appeared to be more diffuse as opposed to the epithelium, both in infected and mock-treated mice, indicative of stable basal expression of the protein in this structure across all cellular populations present in the bulb.

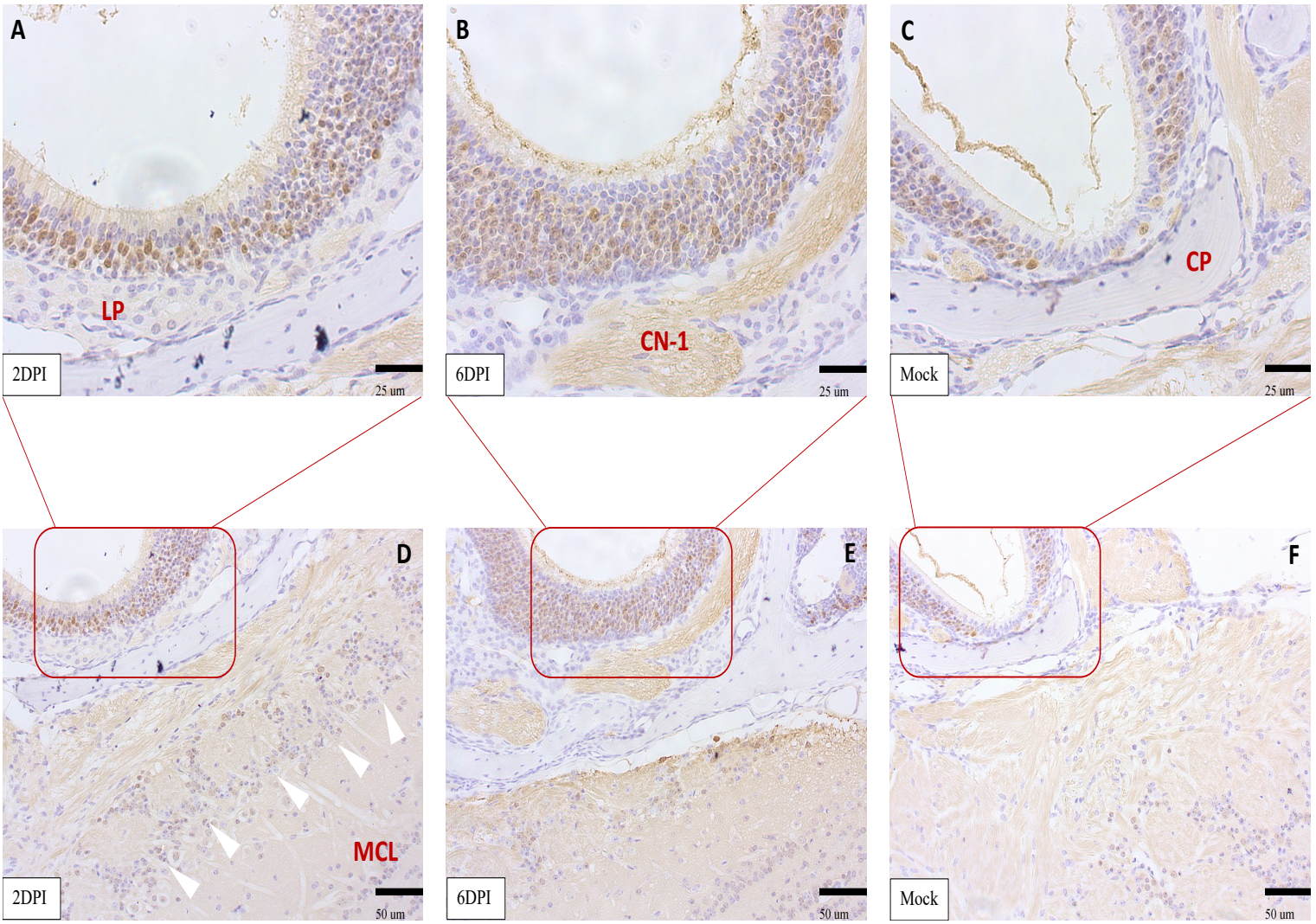

Figure 14: Endogenous α-Synuclein Is an Integral Component of the Olfactory Epithelium and Olfactory Bulb in Wildtype Mice. Example IHC-based, side-by-side images from 2DPI (A and D) and 6DPI (B and E) mice alongside a mock (C and F) showcasing the staining patterns of endogenous α-synuclein in anterior olfactory structures. In the olfactory bulb, α-synuclein shows a diffuse and dispersed staining across the different layers, including the glomerular layer (white arrow heads) surrounded by the heterogenous population of juxtaglomerular neurons and the mitral cell layer (D, E, and F). Insets from the olfactory bulbs captured homing in on the intact olfactory epithelium (A, B, and C) reveal the distribution of α-synuclein within the different cells composing the epithelium**.** It is seen in olfactory sensory neurons, supporting cells, and basal progenitor cells in these mice regardless of the infection status. It is also observed to a lesser extent in the lamina propria, and strongly resides in the nerve bundles of the olfactory sensory neurons (CN-1) traversing the cribriform plate to form synapses in the glomeruli. No qualitative differences were observed in the staining pattern of α-synuclein in these mice. No further quantification was performed. Primary Ab: Syn-1 @ 1:3000. LP: Lamina Propria; CN-1: Cranial Nerve 1; CP: Cribriform Plate; MCL: Mitral Cell Layer. 1 section was stained per (n) mouse, where n=12. Scale bar (A-C): 25um; (D-F): 50um.

α-Synuclein Overlaps with VSV-GFP+ Structures in the Olfactory Epithelium and Glomeruli

The interaction between α-synuclein and RNA neurotropic viruses has been a topic of interest in recent scientific studies. Indeed, studies have indicated that an infection with West Nile Virus (WNV) can lead to increased expression and accumulation of α-synuclein in infected neuronal cells and brain tissues, and similar findings have been reported with the Japanese Encephalitis Virus (JEV) in infected neuronal cells (Beatman et al., 2016). Further, co-localization studies have demonstrated the presence of Influenza A virus IAV viral proteins within α-synuclein-positive neuronal cells in animal models and post-mortem human brain samples (Marreiros et al., 2020). In the context of VSV-GFP, little has been reported on the state of α-synuclein when an infection of the former is underway, and there is no available documentation on the interaction between this conserved neuronal protein and VSV-GFP, if existent, which might in turn influence a myriad of post-translation alterations. Here, I investigated the co-localization of the nasally introduced VSV-GFP and endogenous wildtype α-synuclein in the olfactory epithelium and the olfactory bulb. **Figure 15** showcases bundles of axonal terminals from olfactory sensory neurons in (A) from a representative 2DPI animal, where an overlap of anti-VSV-GFP signal in green and anti- α-synuclein signal in red was observed in a yellow shade. The olfactory nerves are a known route of entry of VSV-GFP into the bulb and deeper olfactory structures as shown previously and reported in the literature, which matches the anatomical distribution of α-synuclein in a normal and healthy physiological state as outlined by the positive staining described in these mice. Hence, α-synuclein is abundantly and readily available in areas of viral infection and this co-localization does not contradict the protein expression profile of α-synuclein.

Another spot of signal co-localization observed was in the glomerular layer of the olfactory bulb in distinct glomeruli where VSV-GFP resides, as specified in staining efforts previously to report on the temporal spread of VSV-GFP in infected mice of the main cohort. The overlap of signal seen in the glomeruli of 6DPI mice (**B, figure 15**) is best described as punctae-like and discrete, resembling the neuronal junctions formed between the axons of olfactory sensory neurons and the dendrites of different cell types. This comes as no surprise when considering the presynaptic primary localization of the neuronal α-synuclein protein and the infection of VSV-GFP of nerve endings and the consequent hijacking of the CN-1 that innervates the olfactory bulb. Hence once again and considering the distribution profile of α-synuclein natively in these structures, if a direct interaction between VSV-GFP and α-synuclein proves to be true, then the aforementioned olfactory structures at which an overlap of signal was observed is understandable. No other olfaction-relevant areas or brain regions were assessed for this phenomenon as the next section on α-synuclein modifications in reference to infection will focus solely on the olfactory epithelium and olfactory bulb, namely the areas of interest in this project but also the purported initiation sites of PD at the early stage.

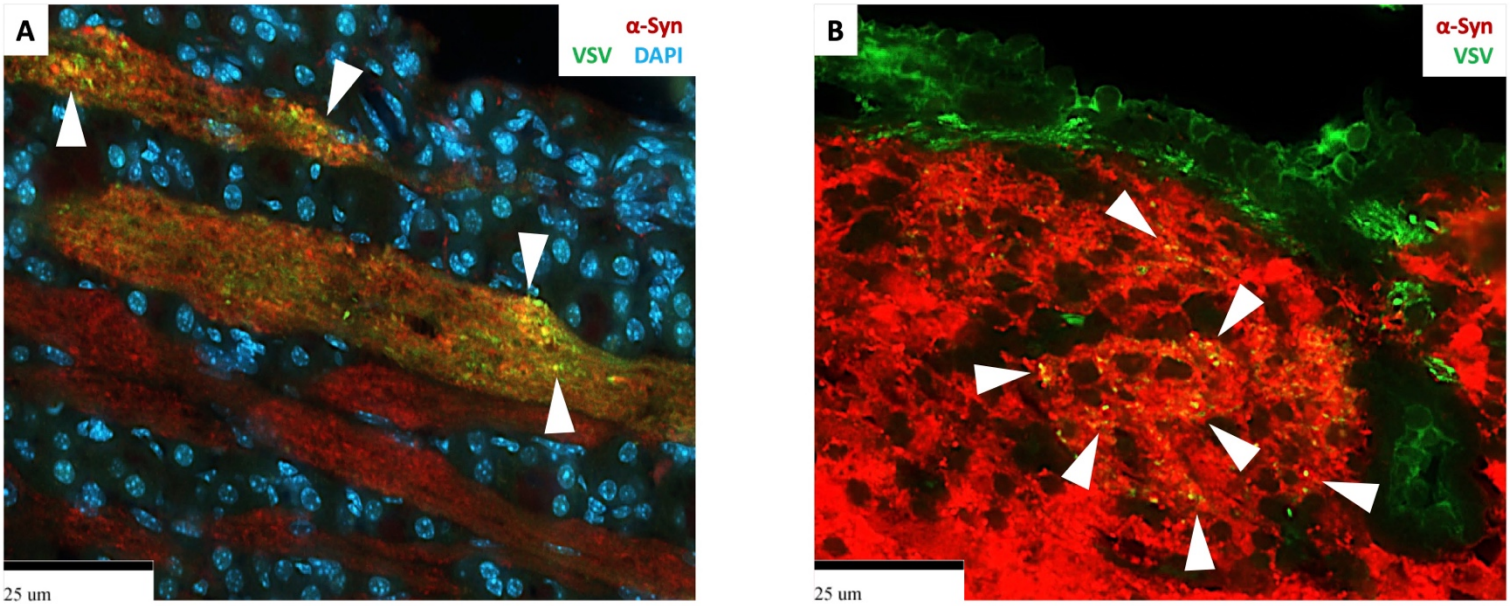

Figure 15*:* Endogenous α-Synuclein Partially Overlaps with Viral Particles at Initial Points of Entry in Anterior Olfactory Structures. Example indirect immunofluorescence (IIF)-based micrographs captured in 2- and 6DPI mice showcasing the olfactory nerve bundles of the olfactory nerve in (A) and axonal terminals localized to the interior of the glomeruli in (B), where an overlap of α-synuclein and VSV-GFP signal (white arrowheads) is observed, alluding to a possible direct interaction and association between the two entities. Two sections were stained per (n) mouse, where n=4. Scale bar: 25um.

VSV-GFP-Induced Post-translational Modifications of Endogenous WT Mouse α-Synuclein

To investigate possible post-translational modifications in a-synuclein induced by VSV-GFP, three primary antibodies generated against α-synuclein were used. Firstly, the anti-phospho-S129-α-synuclein (commercially known as EP136Y), which solely detects α-synuclein phosphorylated at Serine129 and is designed to work in mouse, was used. Secondly, the anti-p62 antibody (or SQSTM1), which targets the autophagosome cargo protein p62 known to interact with polyubiquitinated proteins and facilitate their selective autophagy (Pankiv et al 2007), was used. The relevance of this antibody stems from the reporting on the p62 / SQSTM1-dependent autophagy of ubiquinated and phosphorylated α-synuclein inclusional bodies (Watanabe et al., 2012). Lastly, the anti-aggregated-α-synuclein antibody (referred to as MJFR14642) was used, which is a novel tool that is conformation specific and is able to detect aggregated mouse α-synuclein species as opposed to the numerous other antibodies that were engineered specifically targeting the aggregated forms of human α-synuclein, all of which warranted its use in this project. The investigation of these recognized pathological modifications of α-synuclein was focused on the olfactory epithelium, the glomeruli, and mitral cells of the olfactory bulb, for this project is centered on anterior olfactory structures and cellular population where PD pathology initiates. Mice from the 6DPI timepoint were used to fulfill this quest since viral infiltration and infection of the aforementioned structures was recorded along with a heightened concurrent inflammation and activation of primary glial immune cells. This made the choice of 6DPI mice to explore a plausible link between VSV-GFP-infected olfactory structures and neurons and an increased phosphorylation, degradation, and aggregation of α-synuclein the most suitable amongst all timepoints included in this cohort.

In the olfactory epithelium, under conformable imaging conditions (i.e., consistent exposure, magnification, black and white values in the Zen imagine software), there was no phosphorylation detected in mock and 6DPI animals in any of the cell types as indicated by the absence of the EP1536Y signal when compared to *Snca*-KO controls (**A: *Snca*-KO, B: mock, C: 6DPI, figure 16**). Imaging settings were first adjusted and standardized to the *Snca*-KO mouse, however, both mock-treated mice and 6DPI animals did not reveal any pS129-α-synuclein in any of the cells and olfactory neurons comprising the olfactory epithelium as indicated by the absence of signal in the green channel. Included *Snca*-KO sections omitted any α-synuclein signal in the epithelium compared to the signal seen in the red channel in both the mock and infected mice, illustrating the intrinsic presence of α-synuclein in cellular populations of the olfactory epithelium, most notably the olfactory sensory neurons, and the specificity of the primary antibody used to detect endogenous α-synuclein. Qualitatively, there appeared to be a general increase of α-synuclein signal in the red channel in the infected group in the olfactory epithelium, potentially hinting at either an increased protein expression or a halting of effective degradation in site (n = 2 per treatment group).

Nonetheless, when the phosphorylation of α-synuclein at Ser129 was assessed in the glomeruli, the majority of positive staining – mostly seen as overlap of α-synuclein in the red channel and EP1536Y in the green channel – was detected in 6DPI mice inside the glomerular structure in what seemed to be axonal terminals (**D: *Snca*-KO, E: mock, F: 6DPI, figure 16**). The glomeruli in mock animals showed little-to-no signal at times, and the *Snca*-KO once again omitted signal otherwise generated from the anti-α-synuclein and anti-pS129-α-synuclein entirely. Some subtle staining was also observed in the ensheathing cells surrounding the glomeruli which appeared to have a cytoplasmic localization. Positive staining inside the

glomeruli had the punctae or spot-like appearance, rather than a diffuse or spread-out pattern, congruent with the anatomical nature of the axonal terminals that intersect within the glomeruli. Although no quantification was performed to look into possible significance of these findings, the mock group appeared to have much less overall positive pS129-α-synuclein signal when studying the glomerular layer.

Furthermore, when looking at mitral cells deeper in the olfactory bulb, positive signal, interestingly, was a lot more prevalent compared to that of the glomeruli overall, but especially in 6DPI animals when compared to mock-treated mice (**G: *Snca*-KO, H: mock, I: 6DPI, figure 16**). Positive reactivity resembled a mixture of cytoplasmic staining, but also robust nuclear staining seen especially in the 6DPIs. There were discernible differences between the two groups to the eye, both signal prevalence and intensity wise, where the pS129-α-synuclein signal in the mock-treated mice appeared to be nuclear mostly and less so cytoplasmic. Also, the intensity of α-synuclein signal in the red channel seemed to be stronger and more widespread to the eye in the mitral cell layer in analyzed 6DPI mice in contrast with mock-treated mice. No quantifications of positive signal intensity or pixel count was conducted for an objective analysis (n = 2 per treatment group). Of note, the methodology in assessing results initially was based on the notion that standalone pS129-α-synuclein signal was disregarded as non-specific or background if it did not co-localize with α-synuclein, both in infected and mock-treated mice; however, comparisons with *Snca*-KO mice that omitted any pS129-α-synuclein signal from both the glomeruli and mitral cells urged the revision of this notion. It was ultimately established that the pS129-α-synuclein signal, even if not overlapping with α-synuclein as seen especially in nuclei of mitral cells, was positive and real, considering that it is absent from the knockout control mice and hence sensitive and specific for phosphorylated α-synuclein populations.

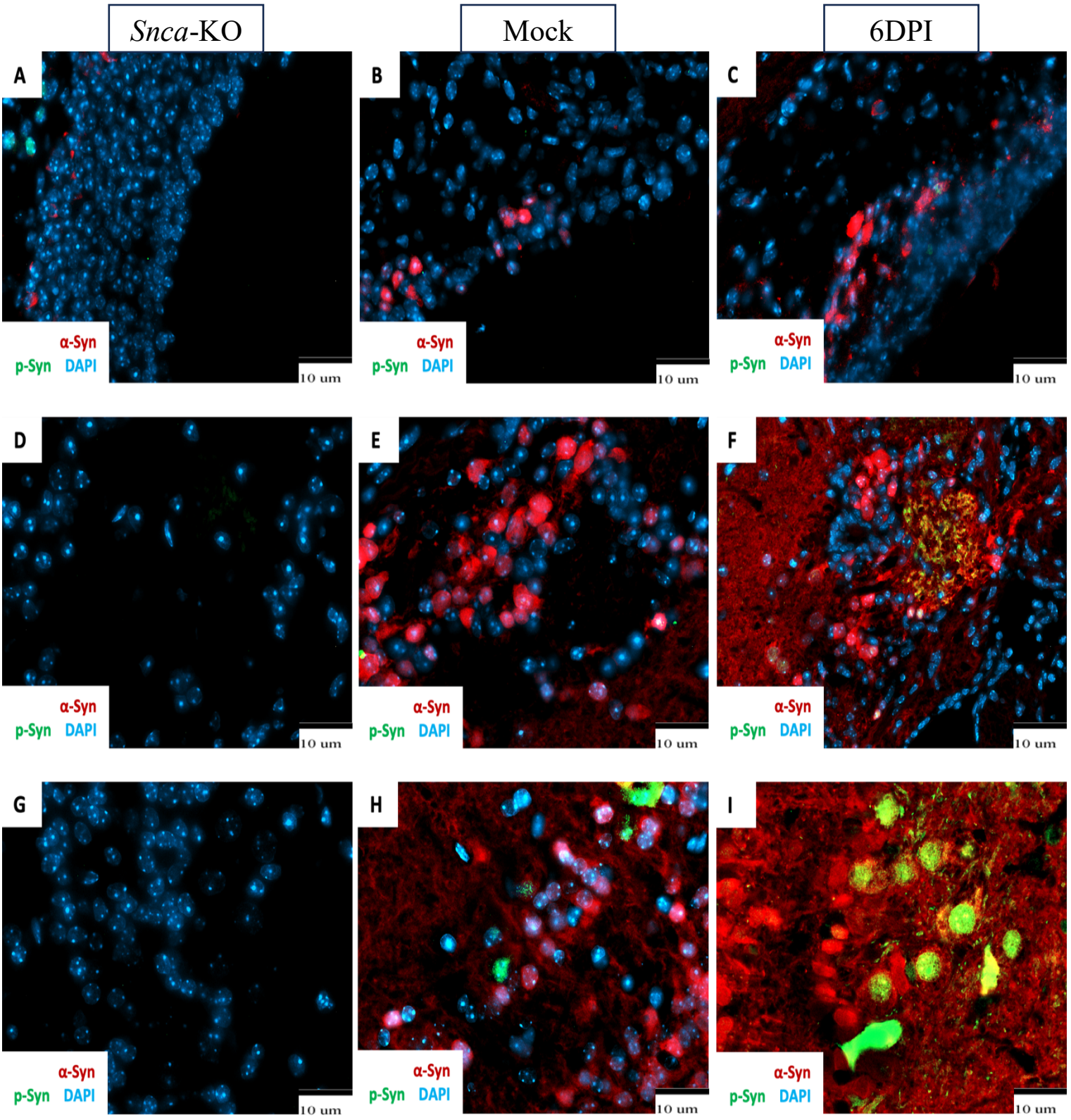
Snca-KO
Mock
6DPI
A
B
C
D
E
F
G
H
I
α-Syn
p-Syn
DAPI
10 um

Figure 16: Detection of Phosphorylated α-Synuclein (Ser129) Appears to be Enhanced by Infection in Select Structures of the Anterior Olfactory Circuitry. Representative indirect immunofluorescence images of anterior olfactory structures of interest including the olfactory epithelium (A, B, and C), glomeruli of the olfactory bulb (D, E, and F), and the mitral cell layer of the olfactory bulb (G, H, and I) showcasing double labeling for α-synuclein in red and pS129-α-synuclein in green. The left lane of images was taken from an *Snca*-KO mice as a control for the expression of α-synuclein and its phosphorylation; no signal was observed in those animals using either antibody, ensuring the credibility of signal observed in mock and infected animals. Note, no S129 phosphorylation of α-synuclein is seen in the epithelium of either mock (B) or 6DPI mice (C) under standardized development conditions used. In (F), specific pS129-α-synuclein signal, partly co-localized with endogenous α-synuclein, was recorded in the glomeruli of 6DPI mice in what represents neuronal synapses and to lesser extent in the cytoplasm of juxtaglomerular cells compared with mock-treated mice (E) that omitted most signal. Mitral cells conveyed an abundance of nuclear S129 phosphorylation of α-synuclein and perinuclear co-localization of signal in 6DPI mice (I) compared with mock-treated mice (H) which lacked that signal overlap and showcased a reduced nuclear staining frequency. One section was stained per (n) mouse, where n=7. Scale bar: 10 um.

Figure 17 displays representative images from 6DPI animals alongside mock-treated mice for a visual comparison of the signal from the overlap of α-synuclein and p62 in the red and green channels, respectively. No p62 knockout animals were used as controls due to the unavailability of such mouse line at our lab. However, the antibody used to detect this protein in mouse tissue was cited in many articles published in respectable journals and claimed to be both specific and sensitive to mouse p62.

In the epithelium, spots of signal co-localization between p62 in green and α-synuclein in red were innumerable and extensive in examined 6DPI mice compared with mock-treated mice (**A: mock, B: 6DPI, C: 6DPI, figure 17**; white arrowheads point to select spots of co-localization). The distribution pattern of α-synuclein in the epithelium was familiar and well-appreciated, where staining was robustly seen in olfactory sensory neurons scattered mid-level but also in basal (progenitor) cells localized to the base of the epithelium, and to a lesser extent, intensity wise, in the dendrites and axonal bundles of the olfactory neurons. Images were captured from mock-infected animals first and settings were kept consistent across the board to bring background signal to a minimum, thus making the technical imaging conditions identical. The first striking observation in epithelium tissue in 6DPI mice was the sheer overlap of signal between α-synuclein in these local cellular and neuronal populations and the ubiquitin-binding scaffold protein, p62, suggesting the ubiquitination of endogenous α-synuclein in those very spots and the marking of it for degradation through autophagy and ubiquitin-proteosome-mediated proteolysis. The overlapping signal appeared to be both nuclear and cytoplasmic, alluding to the ubiquitination of both nuclear and cytoplasmic α-synuclein in infected epithelial cells and their surrounding parenchyma, where mock-treated mice were greatly void of this widespread co-localization of signal. The second observation concerned that of standalone p62

signal; although the mock conveyed a considerable amount of p62 staining, infected animals displayed an increase of it, qualitatively, both in the epithelium itself but also in the islands of olfactory nerves seen underneath the lamina propria of the olfactory epithelium. This implicates other proteins and substrates which have been ubiquinated, possibly viral induced, and are linked to the autophagic machinery to enable their degradation in the lysosome.

Immunohistochemical development from the bulb using the anti-VSV antibody was incorporated to illustrate the intensity of the virus residing inside the glomeruli of 6DPI mice side-to-side with a mock as a negative control (**D: mock**; white arrowheads point to the glomerular structures, **E: 6DPI**; white arrowheads point to staining of viral proteins, **figure 17**). The bulk of staining coincided with connections formed between axonal terminals and dendrites of the different neuronal cell types inside the glomeruli and was seen to a lesser extent in the cellular parenchyma surrounding the one glomerulus in question. Since the coupling of three primary antibodies in indirect immunofluorescence was not feasible due to similar host species, the IHC staining of anti-VSV-GFP (**E, figure 17**) served as a guide as to where the virus resided exactly and fueled the subsequent investigation of possible pathological alterations in α-synuclein in those particular spots. As such, serially cut sections following the IHC-developed sections were used for the proposed investigation to ensure a near-identical distribution of viral particles. Accumulated IIF results suggested that α-synuclein co-localized with p62 cargo protein in the glomeruli where VSV-GFP was seen in immunohistochemical stains and appeared to be especially concentrated inside of the glomeruli where the bulk of anti-VSV-GFP staining was recorded (**H, figure 17**). The co-localization was not detected in all the glomeruli of the glomerular layer, but was rather limited to select or neighboring glomeruli, suggesting a potential influence of VSV-GFP infecting those structures on the proteostasis of endogenous α-synuclein.

This was, in turn, suggestive of localized ubiquitination of α-synuclein – due to homeostasis disturbances – and the ultimate targeting for degradation via p62 in those particular glomeruli. This was in contrast with mock-treated animals (**F, figure 17**), where overlapping signal between anti-p62 anti-α-synuclein antibodies in green and red channels, respectively, was rarely seen in the glomeruli and its immediate parenchyma. There was, however, scattered standalone p62 signal in the mock group, which appeared to be mostly cytoplasmic in juxtaglomerular cells, but was altogether much lower than the standalone p62 signal observed in 6DPI animals. This further suggested that the differences observed in signal overlap – or the greater signal overlap seen in infected 6DPI animals – was either directly influenced by the viral infection, replication, and/ or the incited immune response and inflammation in those olfactory junctional structures, where the latter could trigger a cascade of cellular processes ultimately affecting the homeostasis of α-synuclein.

Lastly, co-labeling of α-synuclein and p62 in the mitral cell layer yielded infrequent signal co-localization in 6DPI animals in comparison with mock-treated mice (**I: mock, J: 6DPI, figure 17**). The overlap of signal, when detected, appeared to be mostly cytoplasmic, although a portion of it was also seen within nuclei of these neurons. When mock animals were studied under identical imaging conditions, signals for the p62 scaffold protein were less frequent and of lesser intensity, in the field of view. There was, however, the occasional signal overlap between α-synuclein and p62 in mock-treated mice, which seemed to be solely nuclear when observed. The overall frequency of signal co-localization in the mock group was consistently lower than that of 6DPIs and omitted any clear cytoplasmic localization.

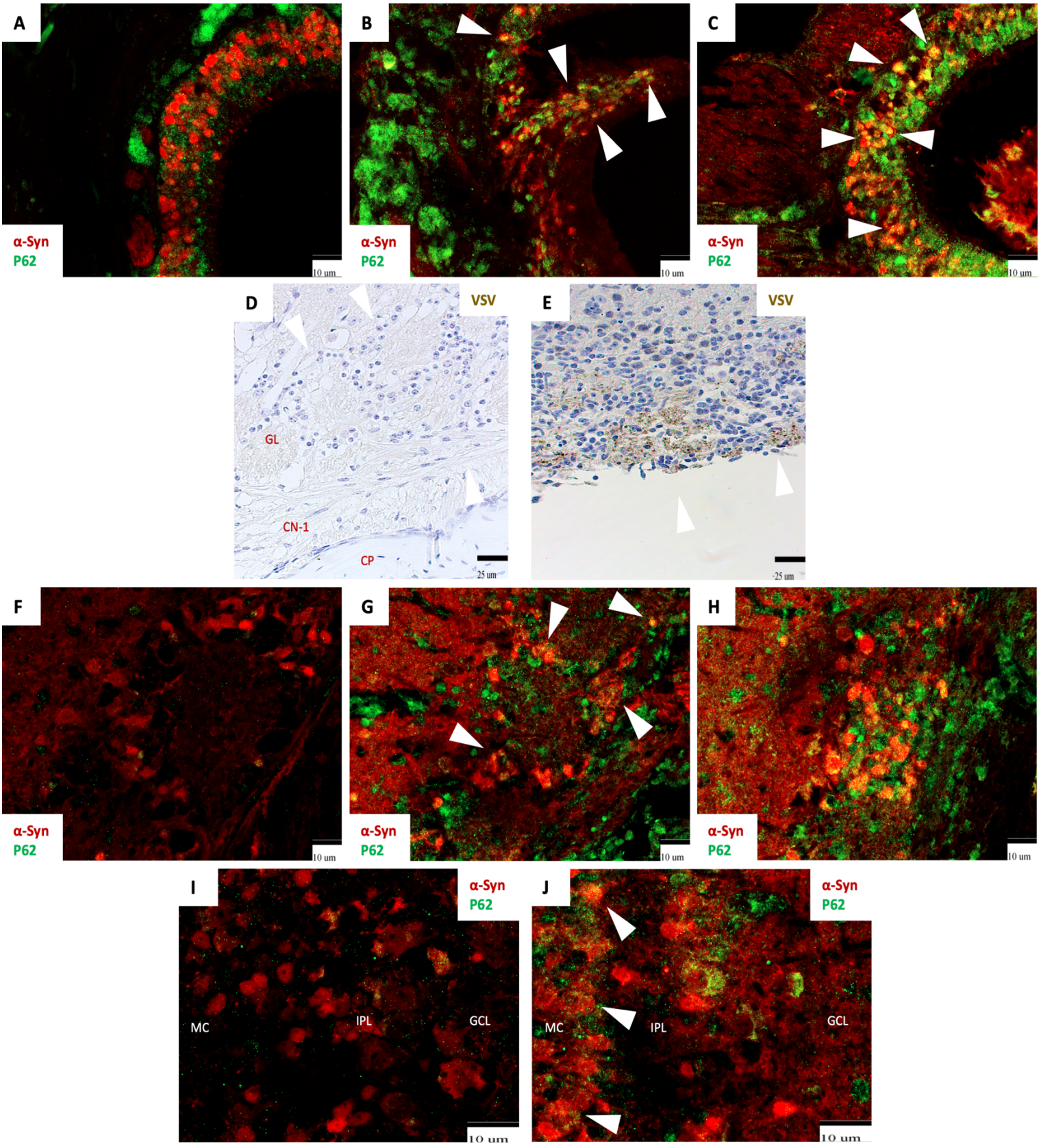
A
α-Syn
P62
10 um
B
α-Syn
P62
10 um
C
α-Syn
P62
10 um
D
VSV
GL
CN-1
CP
25 um
E
VSV
-25 um
F
α-Syn
P62
10 um
G
α-Syn
P62
10 um
H
α-Syn
P62
10 um
I
α-Syn
P62
MC
IPL
GCL
10 um
J
α-Syn
P62
MC
IPL
GCL
10 um

Figure 17: Association of α-Synuclein with the p62 Scaffolding Protein Appears to be Enhanced by Viral Infection of Anterior Olfactory Structures. (A, B, and C) Representative indirect immunofluorescence images of anterior olfactory structures including the olfactory epithelium, (D - H) glomeruli of the olfactory bulb, (I and J) and the mitral cell layer of the olfactory bulb, showcasing double labeling for α-synuclein in red and p62 cargo protein in green. In the epithelial sections, the mock-treated animal (A) exhibits little signal overlap seen mostly in cytoplasmic and perinuclear compartments in contrast with the extensive signal co-localization observed in analyzed 6DPI mice (B and C). Immunohistochemistry-based microscopy images of anti-VSV-GFP staining in mock (D) and 6DPI mice (E) demonstrating robust immunoreactivity and a preference of the virus to localize to nerve terminals inside the glomeruli, where indirect immunofluorescence microscopy revealed abundant co-localization between α-synuclein and p62 (H), but also a number of cytoplasmic signal overlapping spots in juxtaglomerular cells (G), with sparce signal overlap overall in the analyzed mock-treated mice (F) and decreased p62 signal. The mitral cell layer, internal plexiform layer, and the granule layer of (I) mock and (J) 6DPI mice reveal co-localization of α-synuclein and p62 in neuronal bodies of mitral cells and to a lesser extent in granule cells in comparison with mock-treated mice, where signal overlap but also p62 signal itself are minimal. CP: cribriform plate, CN-1: cranial nerve 1, GL: glomerular layer, MC: mitral cells, IPL: internal plexiform layer, GCL: granule cell layer. 1 section was stained per (n) mouse, where n=7. Scale bar A-C, F-J: 10um; D and E: 25um.

As mentioned, the anti-aggregated-α-synuclein antibody (referred to as MJFR14642) was the third choice of suitable antibodies to investigate the state of α-synuclein in light of the introduced infection. Similarly, structures of interest included the epithelium, glomeruli of the bulb, and the mitral cell layer. A lengthy journey of optimizing the conditions and concentration of this antibody resulted in interesting outcomes; there were no distinguishable differences in the olfactory bulb between the 6DPIs and mock-treated mice, which in this case, meant no detection of clear positive staining under set conditions (not shown). Results were cross-validated with an *Snca*-KO mouse that also did not reveal staining in the olfactory bulb, whether be it the glomeruli or the mitral cells (not shown). It is possible that this antibody requires further optimization, concentration, or tweaking of antigen retrieval conditions altogether to pick up aggregated α-synuclein species in the olfactory bulb and its cellular populations. Interestingly, the olfactory epithelium was where this antibody revealed positive staining and striking differences between WT mice (both mock and infected), and *Snca*-KO mice, which were completely blank, staining wise, and devoid of signal in the epithelium (comparison of **A, B, and C, figure 18**). The staining, when seen, emerged as dense, mostly nuclear, and cell-type specific, with an increased localization to parts of the epithelium that were mid-level. Judging from the pattern of staining and the level at which the staining was seen in the pseudostratified olfactory epithelium, the speculation was that those α-synuclein-aggregates resided in olfactory sensory neurons of the epithelium. To verify this, co-labeling utilizing the same anti-aggregated-α-synuclein antibody paired with either an anti-olfactory sensory neuron-marker-protein (OMP), which is a validated antibody to mark mature olfactory neurons in the epithelium, or anti-B-tubulin III (B-tIII), where the B-III isotype of tubulin has been shown to be present in olfactory neurons and respiratory epithelial cells in the microtubule network but not basal cells (Woo et

al., 2002), was performed. Sister sections from select 6DPI animals (n = 2) were analyzed and results from both antibodies were interchangeable. Standalone MJFR14642 signal (**E and H, figure 18**) showcased similar distribution of aggregated α-synuclein within the epithelium. Signal corresponding to the olfactory marker protein nicely labeled the outline of mature olfactory sensory neurons in the epithelium (**F, figure 18**). While staining of the B-tubulin-III also showcased the outline of neurons in the epithelium (**I, figure 18**), the quantity of labeled neurons was overall less. Nevertheless, when the signal representative of aggregated α-synuclein was merged with that of OMP and B-t-III (**G and J,** respectively**, figure 18**), aggregated α-synuclein appeared to be residing in the void inside that labeling of cells' outline seen in the red channel alone: the space which the nucleus inhabits. This helped decipher the exact cellular but also subcellular localization of aggregated α-synuclein within the olfactory epithelium. No quantifications were performed to inquire whether differences in the staining seen, both prevalence and intensity wise, were of significance.

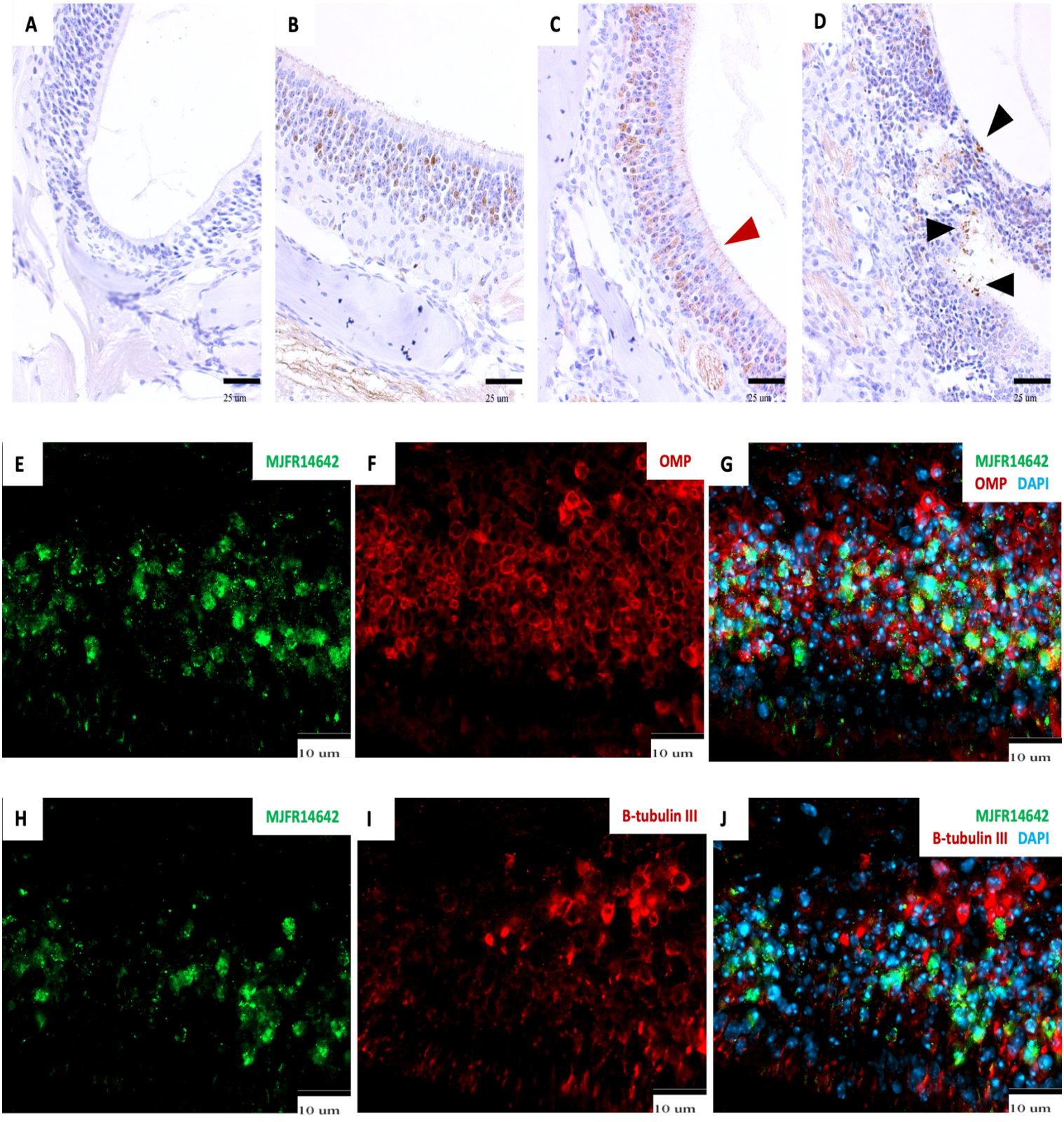
A
B
C
D
25 um
25 um
25 um
25 um
E
MJFR14642
F
OMP
G
MJFR14642
OMP DAPI
10 um
10 um
10 um
H
MJFR14642
I
B-tubulin III
J
MJFR14642
B-tubulin III DAPI
10 um
10 um
10 um

Figure 18: Aggregation of α-Synuclein as Detected by Positive MJFR14642 Staining in the Olfactory Epithelium. (A-D) Representative immunohistochemical images from the olfactory epithelium of (A) an Snca-KO mouse as a control, (B) Mock, and (C and D) 6DPI mice following VSV-GFP inoculation, where red arrows in (C) point to positively labeled dendrites of olfactory sensory neurons extending to the surface of the epithelium and black arrows in (D) point to dense and punctae-like cellular staining where epithelial damage as a result of inflammation was observed. (E-J) Examples of indirect immunofluorescence micrographs from 6DPI mice demonstrating co-labeling of olfactory sensory neurons using antibodies against (E-G) the olfactory marker protein or (H-J) B-tubulin III in red coupled with MJFR14642 against aggregated α-synuclein in green. Notice how the MJFR14642 generated signals representative of aggregated α-synuclein species conveyed a preference to localize to the nucleus in the epithelium of wildtype mice under developing and technical conditions used. OMP: olfactory marker protein. 1 section was stained per (n) mouse, where n=7. Scale bar A-D: 25um; E-J: 10um.

The Total Amount of Endogenous WT Mouse α-Synuclein is Increased in VSV-GFP Infection

This project aimed to examine the impact of neurotropic RNA virus infection on α-synuclein endogenous levels in mice, utilizing Western blot densitometry as a quantitative measure and additional readout to substantiate previous findings. This aided in deciphering the link between the pathological modifications recorded in 6DPI mice and the total amount of protein present in their brains. The investigation focused on hemibrains of 6DPI mice, split into right and left, excluding the olfactory bulbs. The reason of exclusion was the low volume of sample left of olfactory bulbs after completing the plaque assay analysis. It has been shown, both in this project and in the referenced work of Huneycutt et al (1994), how VSV spreads in multiple brain regions and infects structures beyond the olfactory bulb by 6DPI. Hence, if the viral replication and infection of neuronal and glial populations is indeed influencing the total amount of α-synuclein present within the brain, this very phenomenon should be detectable by studying the hemibrains of mice at 6DPI.

The antibody used to probe this was Syn-1 to ensure detecting similar populations of α-synuclein captured in imaging. All samples analyzed belonged to wildtype females of adult age, lysed, and processed identically, ensuring that 40ug of protein total was loaded onto each respective lane in the gel. The analysis of 6DPI hemibrains demonstrated an increase in overall α-synuclein quantity, suggestive of either an increased protein expression at the mRNA level or a halt in its clearance and turnover. The densitometric quantification, carried out according to the protocol outlined in the material and methods section and standardised to ponceau S staining to control for equal loading amounts of protein, revealed a barely significant elevation of α-synuclein ($p = 0.0571$) with a fold change of 1.25 compared to the mock group. However, a trend of enrichment in endogenous α-synuclein detected amounts was well appreciated visually.

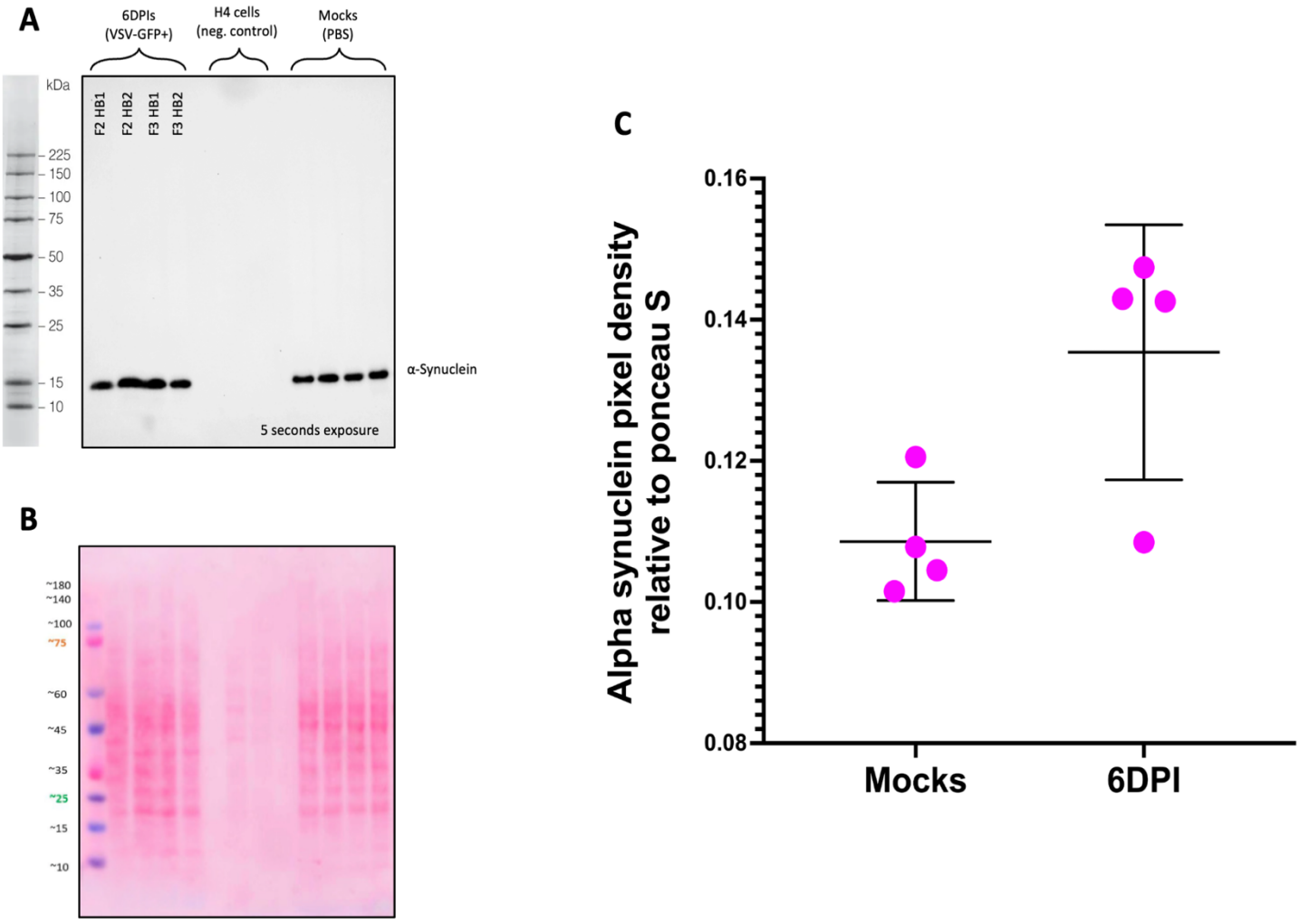

Figure 19: Vesicular Stomatitis Virus Appears to Influence Endogenous α-Synuclein Levels in a Trend of Elevation. (A) Western blot for endogenous mouse α-synuclein in 6DPI hemibrains and mock animals and (B) ponceau S stain as a loading control for each sample. Samples were lysed and run on a 4-12% Bis-Tris gel and immunoblotted with Syn-1. (C) Densitometry analysis from Western blot for detected α-synuclein using whole hemibrains, separated into right and left, from VSV-GFP-inoculated wildtype mice. Each data point represents the calculated band pixel density per each hemibrain blotted. Data are shown as the mean of measurements ± SD of band pixel densities, where the latter is represented as error bars in each respective group. Both 6DPI and PBS-administered mock mice were corrected for ponceau S loading to control for identical protein loading amounts. Difference between the two groups was not significant; P = 0.0571, nonparametric and unpaired Mann-Whitney T test. All samples belonged to female mice.

Discussion

Epidemiological studies link the risk of typical PD and parkinsonism to past viral infections in humans, and emerging scientific evidence suggests a link between experimentally induced viral infections with the initiation of α-synuclein-related pathologies in animals. Researchers have established that viral infections can trigger an inflammatory response in the brain, leading to the activation of microglial cells and the release of pro-inflammatory cytokines. These immune responses may facilitate the misfolding and aggregation of α-synuclein protein, a hallmark of PD. Hence, virally induced neurodegenerative processes could contribute to the initiation and/or progression of PD-like symptoms (Smeyne et al., 2022). However, most studies have either investigated the state of human α-synuclein in overexpression models of rodents in reference to infection or have done so with endogenous mouse α-synuclein but in areas of the brain that exclude the olfactory bulb and its accessories – the initiation site of PD pathology at stage 0 (in the Braak and Del Tredici scheme; Braak et al., 2003). This thesis is to shed light on changes in anterior olfactory structures following the administration of a neurotropic RNA virus in wildtype mice expressing endogenous α-synuclein.

The Tropism and Progressiveness of VSV-GFP in the Mouse Brain

Using a combination of immunochemical and biochemical techniques, I have gained insights into the tropism and progression of vesicular stomatitis virus expressing green fluorescent protein (VSV-GFP) in the brains of mice following their nasal administration. This approach has allowed me to trace VSV-GFP's entry into the central nervous system and its subsequent spread and also assess the viral burden in different anatomical regions at different timepoints post-inoculation. It has been documented in the literature how VSV can enter the brain in a retrograde axonal transport fashion, exploiting the axonal connections of olfactory

sensory neurons to gain access to the brain when introduced to the nasal passage or peripheral nerves (Huneycutt et al., 1994). The same literature reported that VSV-GFP, secondary to swallowing nasal secretions containing the virus, can be transported via the autonomic nervous system, the vagus nerve, or blood circulation into innervated lower brainstem structures, such as the medulla, constituting a secondary, indirect route of entry into the brain. From there, it disseminates along specific neuroanatomical pathways, such as the olfactory bulb, hippocampus, and cortex, leading to the development of encephalitis. Immunochemical staining has facilitated the detection of virally expressed proteins, enabling the pinpointing of their distribution within distinct brain regions. This model proves to be a valuable tool for studying virally-induced neurological disease, but also to examine the occurrence of protein pathologies in cells within anatomical structures, or regions that have seen the infection and its ensuing host inflammation.

The results of the staining utilizing immunohistochemistry and the anti-VSV-GFP and anti-GFP antibodies allowed me to replicate some of the findings that have been published in the literature in regard to viral distribution in a temporal fashion, but also to track the progression of VSV-GFP in diverse anatomical regions of the mouse brain, especially anterior olfactory structures, where the investigation of potentially virus-induced synucleinopathy was an aim. Two days after inoculating wildtype mice with VSV-GFP, immunohistochemical staining revealed a clear distribution of viral particles in the olfactory epithelium that appeared to be heavily infected with robust staining of different cell types in the epithelium, most prominently of olfactory sensory neurons and basal cells, which function as progenitor cells and play a role in the attachment of the columnar epithelium to the lamina propria. The mucosa of the ethmoidal sinuses was also robustly labeled, congruent with the nasal method of VSV-GFP inoculation and virus uptake by non-neural cells as well. Viral staining was also consistently seen in the nerve

bundles (i.e., grouped axons) of the olfactory sensory neurons, stemming from cell bodies in the olfactory epithelium and traversing the lamina propria as well as cribriform plate to innervate the glomeruli and establish connections with dendrites of mitral, tufted, and periglomerular cells. When assessing the infiltration of VSV-GFP into glomeruli at 2DPI, they appear to be devoid of staining for viral reactivity. There are no reports of VSV-GFP being detected in the glomeruli or deeper beyond that in the olfactory tract as early as 48hrs post-inoculation. Additionally, no viral reactivity was seen in mitral cells or the granule cell layer of the bulb, which represent key relay sites within olfaction. Other notable regions of viral reactivity that were seen in 2DPI mice included the caudal part of spinal nucleus of the trigeminal (SPVC) and the spinal vestibular nucleus (SPIV). According to known anatomical connections in the brain, that VSV-GFP is unlikely to have reached the aforementioned nuclei travelling from the olfactory bulb, for I) these nuclei are outwardly distant from immunoreactive olfactory structures making it improbable for the virus to have traveled at an early timepoint to such caudal structures, and II) the SPVC and SPIV are not known to have centrifugal projections into the olfactory bulb, so the notion of viral retrograde transport does not apply to those specific areas reported on in the 2DPI group in the medulla where VSV-GFP-positive staining was seen.

By 4DPI, VSV-GFP had disseminated into select regions of the glomerular layer of the olfactory bulb (i.e., not spread out or seen in the entire layer). This is also in accordance with the work done by Huneycutt et al (1994), who reported viral reactivity in the glomeruli post day 3 of inoculation at the same dose used in this project. The olfactory epithelium and axons of the olfactory sensory neurons forming the CN-I were consistently labeled, albeit the CN-1 was more intensely stained than what was seen in the 2DPI group. This could be attributed to the increased dissemination of the virus from the olfactory epithelium where it first infected and the active

transportation of the virus via anterograde transport along the axons of the neurons in the epithelium and into the bulb to the first real junction of the olfaction route. Other brain regions where VSV-GFP reactivity was seen included the CA2 field in the hippocampus, notably the stratum oriens layer, and the lateral vestibular nucleus (LAV) in the medulla inferior to the superior vestibular nucleus, which is the superior and anterior most structure of the pons and connects with the parabrachial nucleus of the pons via the superior cerebellar peduncle (SCP). Since the hippocampus is a tertiary olfaction structure that plays a role in odor-memory formation where the olfactory bulb receives 'top-down' information from the hippocampus, it is probable that the virus took advantage of the connecting neuronal circuits to migrate to the hippocampus. The olfactory bulb is not only connected to the hippocampus through the entorhinal cortex (Vanderwolf, 1992), but also reciprocally receives direct synapses from the ventral region of the hippocampus (Groen and Wyss, 1990). The presence of VSV-GFP in the LAV at this later timepoint in the infectious course comes as no surprise, especially after recording its presence in more inferior areas in the brain stem in the medulla, namely the SPVC and the SPIV in the 2DPI group, so the notion of VSV-GFP traveling up the brain stem to more superior structures and nuclei via efferent and afferent fibers is of anatomical sense.

Animals in the 6DPI group showed persistent and similar staining patterns to previous timepoint groups, namely the labeling of the olfactory epithelium, lamina propria, CN-1 nerve fibers, and a higher count of glomeruli in the glomerular layer with conspicuous VSV-GFP reactivity. This alludes to the increased delivery of the virus from the olfactory epithelium along the olfactory nerves to the glomerular layer or spread of the virus from select infected glomeruli witnessed at 4DPI to neighboring ones, or both. It is important to note that the majority of reactivity seen within the glomeruli at this timepoint was on the inside of the glomerular spheres,

where the synapses between the terminals of the olfactory nerve and dendrites of mitral, tufted, and periglomerular cells form, with little to no staining seen outside the anatomical borders of infected glomeruli, such as characterised by juxta glomerular cells (JGs). Propagation of VSV-GFP into the deepest layers of the bulb has not only been reported in literature but is also coherent with the development of the lateral olfactory tract, which starts at the rostral–lateral–ventral aspect of the olfactory bulb with the coalescence of mitral and tufted cell axons following their passage through the IPL and islets of granule cells (Walz et al., 2006). Thus, the notion of VSV-GFP traveling anterogradely along the axons of mitral and tufted cells forming the beginnings of the lateral olfactory tract and passing by the granule cells, where the staining is seen in 6DPI mice, makes sense from an anatomical standpoint (Harvey and Heinbockel, 2018).

One other area of clear viral reactivity other than the olfactory structures and olfaction route was the cerebellum, which was not observed in timepoints earlier to 6DPI. There was intense labeling of the uvula of the cerebellum in two mice of this group, confirmed with both anti-VSV and anti-GFP, where the bulk of the labeling was seen in the molecular layers of the pyramus VIII and uvula IX, with staining to a lesser extent in the granule layer underneath. It is described that major afferents, including the locus coeruleus, project from the cerebellum to other parts and regions of the brain, but most notably the nuclei in the pons, to regulate various cognitive and motor functions (Lawrenson et al., 2017). While immunoreactivity of VSV-GFP in the LC was not observed in the cohort of animals studied here, it has been documented in the work of Huneycutt et al (1994). Of note, no positive VSV-GFP staining was observed in any of the mock mice that were administered phosphate buffered saline, as expected.

During the course of CNS infection, anterior olfactory structures in the 10DPI mice revealed labeling of the olfactory epithelium, although much more subtle and faint overall,

indicating possible clearance of viral particles in the cellular populations comprising the epithelium 10 days post inoculation. The same applied to olfactory nerves and the bundles of CN-I seen penetrating the cribriform plate into the bulb; immunoreactivity in those axons was much weaker in all analyzed 10DPI mice than was what observed at earlier timepoints, hinting at a reduced rate of viral trafficking and travel into the bulb from the epithelium. Taken together, this alludes to the possible resolving of the virus and the halting of its replication via the ensuing immune response and the sequential clearance of viral antigens from the epithelium. The glomeruli, however, continued to show positive labeling that had a punctae appearance to it, consistent with the axonal terminals and synapses found inside of the glomeruli, to an extent overall similar to that seen in 6DPI mice. When considering how VSV-GFP did not pierce into the glomerular layer before the 4DPI timepoint all whilst being strongly detectable in the epithelium, its olfactory neurons, and the stemming nerve bundles as soon as 2DPI, it is comprehensible that the immune cells first responded and became 'active' in the aforementioned structures or areas that have seen the virus the earliest to inactivate its proteins in situ, marking them for subsequent clearance and degradation. This temporal pattern of VSV-GFP's infectivity and progressives in the mouse brain demonstrates why various glomeruli in 10DPI mice were still VSV-GFP-positive when the epithelium, lamina propria, and CN-1 nerve fibers showed significantly diminished viral staining, especially when thinking of it from an immune system perspective, where the first immune cells responders are addressed to areas infected first. Furthermore, a novel area of interest for VSV-GFP-reactivity in the olfactory circuitry not seen at earlier timepoints was the olfactory tubercle (OT). The axons of second-order neurons in the olfactory bulb, specifically the mitral and tufted cells, come together to form the lateral olfactory tract. This tract runs along the ventral-lateral part of the brain. Some of the axons from the lateral

olfactory tract enter the molecular layer (layer I) of the OT alongside the PCX, where they are likely to establish synapses (Walz et al., 2006; Harvey and Heinbockel, 2018). This anatomical depiction may help explain how VSV-GFP might have penetrated the olfactory tubercle, especially when viral protein was seen in the granule cell layer in the olfactory bulb at 6DPI, where afferents of mitral and tufted cells are known to traverse the different inner layers of the bulb before making up the lateral olfactory tract and ending up in higher olfactory structures.

An additional and novel area of positive VSV-GFP staining witnessed in the 10DPI group in contrast with earlier timepoints was the SN. However, and since hematoxylin & eosin were used as a counter stain throughout this project to provide a comprehensive picture of the neuroanatomy of the mouse brain, the confident distinction between the SN and other closely associated areas of the midbrain solely using this stain was not feasible. To tackle this, co-labeling of the virus using the anti-VSV antibody and the anti-TH antibody – which labels the dopaminergic neurons in the SNpc and neuronal populations of the ventral tegmental area (VTA) – was employed. Results from immunofluorescence co-labeling studies on two 10DPI mice, where positive staining of viral antigens was seen by IHC in the SN, confirmed the presence of virus surrounding dopaminergic neurons as indicated by positive TH staining, outlining cell bodies of processes of neurons in the compacta part. Not only does the pars compacta project to the striatum and the cerebral cortex, making higher regions of the CNS accessible to the virus via axonal and transsynaptic transmission, but it is also the area affected by the progressive loss of dopaminergic neurons in Parkinson disease that manifests as a typical motor syndrome. It is worth mentioning that in the work of Huneycutt et al (1994) the authors had also reported the presence of VSV-GFP within the VTA, albeit it that was seen at 7DPI, which is the only timepoint where they explored the viral distribution in the whole brain. It is well established that

the SN can be targeted by certain viruses, such as the Herpes Simplex Virus (HSV) and the Japanese Encephalitis Virus (JEV), resulting in encephalitis and movement abnormalities due to neuronal degradation in animal models, both acutely and chronically. As such, the established finding of VSV-GFP making its way to the SN pars compacta, as shown above, adds to the available body of literature of viral RNA neurotropic paradigms to explore the outcomes of infections on dopaminergic neurons, but also to explore endogenous α-synuclein alterations and possible synucleinopathies in the SN. Understanding the role of the SN in this viral tropism context is essential for developing new experimental approaches in PD.

In summary, VSV-GFP appears to utilize more than one route to gain access to brain structures, including afferents of the olfactory sensory neurons in the olfactory epithelium and the autonomic nervous system as well as the vagus nerve which connects to lower structures of the brainstem, such as medulla, but is also possibly transported through the blood stream. The temporal progression of VSV-GFP's immunoreactivity and the staining pattern across the different timepoints provide evidence for the proposition that VSV-GFP infection of olfactory bulb glomeruli leads to its spread through surface structures of the brain, including meninges, and both the anterograde transport along axons of the olfactory sensory neurons and the retrograde transport along axons of neuromodulatory transmitter systems that innervate the olfactory bulb. On the other hand, areas with minimal VSV-GFP antigen presence are unlikely to be involved in VSV-GFP dissemination. Notably, the scarcity of VSV-GFP antigen in certain terminal fields of neuromodulatory systems suggests that anterograde transport is more selective than retrograde transport. Taken together, this viral paradigm and mouse model constitute an appropriate tool to examine the neuropathology of encephalitis associated with the infection and

its associated inflammation, but also to study potential α-synuclein modifications in the distinct cell populations of anterior olfactory structures that are linked to hyposmia in Parkinson disease.

The Viral Burden and Infectivity of VSV-GFP in the Mouse Brain

Measuring the viral concentration in hemibrains, hindbrains, and olfactory bulbs of infected mice played a crucial role in comprehending the progression and determining the viral titer peak of the VSV-GFP-induced infection. This involved quantifying the PFU of infectious virus in brain tissues of mice sacrificed at 2- and 6DPI, yielding valuable insight into VSV-GFP's replication and spread within the central nervous system in complementation to the immunohistological methods. The quantification of viral titers also revealed variance in viral loads of selected brain regions at the two timepoints, which added to our understanding of not only the peak of viral titer in the selected regions, but also pointed at different clearance rates of viral proteins relative to the timepoint examined.

Hemibrains of 6DPI mice excluded the olfactory bulb when excised; this was purposely done to enable the assessment of the transport of VSV-GFP from infected olfactory bulbs into encephalitic structures in measurable units at the predetermined timepoints in the infectious course. The plaque assay unveiled significant variability in viral titers in hemibrains of 6DPI mice, with more than half falling below the sensitivity limit of detection. This phenomenon aligns with expectations, considering that the interferon and immune responses to VSV-GFP intensify after 5DPI, leading to effective viral clearance (Andersson et al., 1993; Bi et al., 1995; Nair et al., 2014). As evident in **figure 4,** the majority of hemibrain samples (5 out of 8) exhibited an absence of detectable virus, falling below the quantifiable threshold of 200 PFU. It is important to note, however, that this lack of detection does not necessarily signify absolute viral protein clearance. It is possible that very low concentrations of replication- and infectious-

competent virus still exist. It is nevertheless generally agreed upon that if a viral titer falls below the set detectable limit, then the infection will be declared as resolved and efficiently cleared. On average, the olfactory bulbs exhibited a higher frequency in revealing VSV-GFP titres, where 3 out of 4 samples showed relatively high PFU counts. This result highlights the olfactory bulbs' fundamental role as the primary portal through which VSV-GFP gains access to the central nervous system, thereby enabling vigorous replication and amplification, which could explain the higher frequency of measuring detectable virus in the bulbs as opposed to the hemibrains. The variance in viral titers between these specific regions accentuates the intricate interplay among viral dissemination, immune reactions, and tissue-selective vulnerabilities at this phase of infection. This confluence of factors further enriches our understanding of the neuroinvasive mechanisms employed by VSV-GFP.

As illustrated in **figure 5**, mice at 2DPI displayed a markedly higher viral titer in their olfactory bulbs compared to the excised hindbrains. The rationale behind the surgical separation of hindbrains in 2DPI mice was to assess the viral infiltration into the rhombencephalon and compare findings to what was established in immunohistological studies, where VSV-GFP+ reactivity could be seen in nuclei of the medulla at this timepoint. The higher measured viral titer in olfactory bulbs versus hindbrains concurs with the notion that the olfactory pathway serves as the primary conduit for the virus to enter the brain (following nasal inoculation). Conversely, replication-competent VSV-GFP was detectable in all hemibrain samples from mice at 2DPI. Thereafter, the decline in the overall viral titers, as seen in olfactory bulbs and hemibrains between 2DPI and 6DPI, signifies effective virus clearance and a proficient ensuing immune response, encompassing innate and possibly adaptive components. Additionally, the distinctive, robust, and closely clustered viral concentration within the hindbrain of mice at 2DPI, consistent

with the medulla staining observed early on via immunohistochemistry, lends support to the engagement of the vagus nerve (CN-X) or alternative routes (such as via cranial nerve IX) in permitting VSV-GFP to the hindbrain. Our findings underscore the mounting of an immune response by WT C57BL/6 adult mice to the nasally administered VSV-GFP by day 6 of its introduction, both in olfactory bulbs separately and hemibrains as a whole.

The Ensuing Proinflammatory Glial Response in the Mouse Brain Following Infection

Immunohistochemical staining yielded valuable insights into the dynamic changes within glial cells in the context of VSV-GFP infection. The staining patterns unveiled the spatial arrangement of both responding and quiescent microglia and astrocytes, illuminating regions of viral replication and the consequent inflammation within the brain. Alongside elucidating the visual response of microglia and astrocytes via microscopic techniques, immunohistochemical staining also offered a valuable comprehension of the connection between activated microglia and astrocytes, as judged by their appearance and transformation from a ‘typical’ outline or profile, and the virus's positioning (i.e., localization) over the course of infection. The combination of VSV-GFP markers with anti-IBA1 and anti-GFAP antibodies made it possible for the investigation of the spatial interplay between sites of viral replication and the dispersion of immune cells reacting to the infection within brain tissue, encompassing the olfactory bulb and its immediate olfactory structures.

Evident indications of microgliosis and astrogliosis were discernible in infected animals when directly contrasted with PBS-inoculated counterparts as seen in **figures 7 and 8**. This was seen by the robust labeling of IBA1-positive microglia and GFAP-positive astrocytes, the augmented migration of glial cells towards the infection site driven by activated microglia, the conspicuous accumulation of glial cells, particularly within olfactory structures, perturbations in

tissue architecture and cellular arrangement, notably pronounced within the olfactory epithelium, and the apparent formation of glial scars, visibly manifesting in the glomeruli of select animals.

Phenotypical specific indicators of microglial activation and the transitioning into an M1 pro-inflammatory state from a resting state were seen and showcased in **figure 7** in multiple regions; this included an enlargement of cells' bodies, the adoption of an ameboid overall shape, retraction and thickening of processes, and a general proliferation of microglia that translated to an increased count. All infected mice exhibited indications of microglial activation within the olfactory epithelium, irrespective of the timepoint of sacrifice, as soon as 2 and extending even as far as 10 days post-inoculation, albeit with some variability. This underscores the acute but ongoing nature of microglial inflammation, persisting even after the infection's resolution and the initiation of the interferon response against VSV-GFP protein from day 5 post-inoculation, reported on by Bi et al., (1995), but also indicated by the apparent reduction in viral titers within infected mice brains at 6 DPI in this project.

In the olfactory epithelium, microglial cells displayed a compact, small, circular, or rod-like morphology across all observation days. Conversely, microglia found along the CN-1 nerve bundles assumed a more elongated and stretched configuration. Notably distinct from their counterparts in the olfactory bulb, microglia in this region of infected animals exhibited an irregular, ameboid, rounded shape, characterized by thicker and generally shorter processes. The intensity of the signal within the cell bodies of microglia also appeared heightened, leading to a more pronounced staining effect and darker appearance under microscopic observation. These morphological differences could potentially stem from anatomical constraints within the observed regions, such as the tightly packed arrangement of the stratified olfactory epithelium and the specific course of the longitudinal nerve fibers. This speculation is based on prior

research that has highlighted various subtypes of microglia within the brain, each displaying distinct intrinsic properties and performing unique functions influenced by the anatomical and physiological features of their residing structures (Li et al., 2022). This underscores the significance of considering both the M state and subtype classification when undertaking comprehensive studies and profiling of microglia. In my project, the focus was placed on examining diverse phenotypic and morphological changes exhibited by microglia upon activation, these being attributed to the inherent plasticity of these cells. As conveyed in **figure 7**, the staining intensity of IBA1+ microglia in the glomeruli were most pronounced on the 6th day post-inoculation. In the 2DPI group, minimal reactivity was observed compared to mock samples, with a noticeable increase at 4DPI and a peak at 6DPI, followed by a subsequent decline in the 10DPI group. Notably, the inner layer of the olfactory bulb, particularly the granule and subependymal layers, exhibited significant reactivity on the 6th day post-inoculation, to a lesser extent on days 4 and 10 post-inoculation. Other olfactory structures, including the olfactory tubercle, displayed indications of microgliosis from 6DPI onward. Visual assessment of microglia in these regions, compared to mock samples, indicated one or more of the aforementioned signs of microgliosis; however, for a quantitative and objective assessment of the microglial response, phenotypical parameters, such the glial body size, percent of IBA1+ signal occupation in the area, circularity and cell solidity were measured in select areas, for these are known to be linked to microgliosis when altered in one direction (Fernández-Arjona et al., 2017; Heindl et al., 2018). As shown in **figure 9**, the standardized percent of area occupied by the IBA1+ signal along with the glial body size exhibited a significant increase in infected mice compared to mock animals. Notably, this increase demonstrated strong significance as early as 2DPI within the olfactory epithelium, a relatively lesser significance in the olfactory bulb at the

same timepoint and presented no substantial difference in the anterior olfactory nucleus during this initial period. This suggests a proliferation of microglia influenced by the presence and infiltration of VSV-GFP proteins. This notion is supported by the heavy VSV-GFP staining observed in the epithelium at 2DPI through immunohistochemistry, the minimal staining in the bulb, and the absence of positive staining in the anterior olfactory nucleus at this early stage of infection. The occupied area percentage, similar to the relative size, appeared to peak at 6DPI across all regions and decreased by the latest timepoint assessed. The difference in IBA1+ signal occupation between infected animals and mock animals became statistically insignificant at 10DPI in the epithelium. This likely suggests the resolution of infection within the olfactory epithelium by this timepoint and a subsequent shift of microglia back towards the M2 anti-inflammatory state. Circularity and solidity values of sampled microglia from the olfactory epithelium and anterior olfactory nucleus followed a similar trend of increase starting at 2DPI and reaching their peak at 6DPI, with a slight decline at 10DPI. Surprisingly, the measured values of these parameters for resident microglia in the olfactory bulb exhibited fluctuations in both directions, recording lower or higher values compared to mock animals. No statistically significant difference was observed with the circularity or density parameters of microglia in the olfactory bulb. This discrepancy could be attributed to either the presence of intrinsic microglial subtypes within the olfactory bulb, each responding with distinct and select morphological changes to a neurotropic infection, or to the large sampling area of the olfactory bulb. This larger area might include microglia that are distant from the site of VSV-GFP replication, hence not being influenced by the signaling pathways triggered by the virus. To address this puzzling observation, a gradient analysis was conducted on representative sections from animals displaying evident viral staining in one or more glomeruli within the glomerular layer (one

animal per timepoint group). As presented in **figure 10**, this analysis spanned four different levels and is outlined in **table 8** in the appendix. Its purpose was to identify more distinct microglial alterations in the measured parameters, particularly circularity and solidity. The analysis involved incrementally increasing the selected area in fixed intervals to track the shifts of these measurements in areas immediately affected by the virus as well as in progressively more distant areas adjacent to the initially selected infected glomerulus. Gradient analysis of size, circularity, and solidity revealed that the highest values of microglial parameters were recorded at level 1, while the lowest values were found at level 4, encompassing microglia distant from the area of viral impact. The 6DPI animals, as analyzed and in line with the quantification conducted on the entire cohort for the size parameter, exhibited the highest values among all animals across different timepoints. The pronounced elevation in circularity and solidity parameters among microglia closest to VSV-GFP staining, and in infected microglia, likely indicates a shift towards the M1 pro-inflammatory state. This transformation involves an increase in cell size, retraction of processes, and the adoption of a more rounded, denser interior shape, particularly among microglia situated in close proximity to viral structures. This deduces that the fluctuation seen in the circularity and solidity parameters were influenced by and sensitive to the sampling of the larger olfactory bulb in comparison with the epithelium and anterior olfactory nucleus, which are more compact.

Non-olfactory regions that displayed VSV+/GFP+ encompassed the spinal nucleus of the trigeminal nerve, the spinal vestibular nucleus, the CA2 hippocampal region, the lateral vestibular nucleus, the cerebellum, and the midbrain across different timepoints. In **figure 11**, quantifications from the cerebellum as an area of reference saw an increase in both cell body size and the percentage of area occupied by the IBA1+ signal. These parameters exhibited higher

values as early as 2DPI and then maintained a plateau until declining at 10DPI. This observation was surprising since VSV-GFP+ staining was not evident in the cerebellum before 6DPI, and the literature has not reported VSV-GFP infiltration into the cerebellum prior to that timepoint (Huneycutt et al., 1994). When quantifying microglial phenotypic parameters in the midbrain, a notable increase in cell body size was apparent on days 4 and 6 post-inoculation, which later decreased at 10DPI to levels comparable to mock animals. This decrease by 10DPI might suggest that the immune response had resolved the infection and contained its effects. VSV-GFP+ staining at 10DPI in areas like the SN might represent residual VSV-GFP proteins that are no longer capable of replication or causing infection. The occupied area percentage of the IBA1+ signal exhibited a gradual increase from 2DPI to 6DPI, albeit insignificantly, and then declined at 10DPI to levels similar to mock animals. However, circularity and solidity parameters from the midbrain did not mirror the inflammatory profiles indicated by cell body size and the percentage of signal occupation, especially on days 4- and 6PI. Circularization and solidity values displayed fluctuations and appeared to drop compared to mock animals at these timepoints, suggesting an adoption of a more irregular shape. This discrepancy could once again be attributed to the sampling of the entire midbrain, a large anatomical structure, and the inclusion of a more diverse population of microglia, including quiescent ones that have not yet transformed into an activated state. Unlike the olfactory bulb, no gradient analysis was conducted on either the cerebellum or midbrain.

The quantification of astrocytes focused on three parameters: cell body size, the percentage of GFAP+ occupied area standardized against mock samples, and perimeter. This decision was made due to circularity and solidity not being known phenotypic changes associated with different physiological states of astrocytes (Yu et al., 2012; Ben Haim et al.,

2015). As presented in **figure 12**, and in the olfactory epithelium, all three parameters showed an increasing trend starting as early as 2DPI with values steadily climbing and reaching their peak at 10DPI. While cell body size and perimeter were not significantly different prior to 6DPI, the area occupied by GFAP+ significantly increased at the 4DPI timepoint. This suggests that astrocytes overexpressed GFAP, linked to astrocyte proliferation and process extension (Yang and Wang, 2016). A similar trend of steady increase was observed in all three parameters within the anterior olfactory nucleus, with significance reached at 6DPI and particularly at 10DPI, where considerable differences in cell body size and perimeter were evident compared to mock samples. The steady increase seen in the olfactory epithelium and anterior olfactory nucleus was mirrored in the olfactory bulb, with peak values reached at 10DPI. This pattern of astroglial reactivity contrasted with microglial activation, which tends to return to normal values after 6DPI in analyzed olfactory structures.

As shown in **figure 13**, in the cerebellum, significant increases in astrocytic size, percent of GFAP+ occupied area, and perimeter were observed as early as 2- and 4DPI. This was intriguing given that VSV-GFP does not enter the cerebellum before 6DPI, as mapped by a study on VSV-GFP tropism in the mouse brain, or at least is undetectable by immunohistochemical techniques prior to 6DPI (Huneycutt et al., 1994). Similar to olfactory structures, parameter measurements reached their highest values at 10DPI, indicating reactive astrogliosis possibly ongoing even after potential resolution of active virus in the cerebellum at 10DPI. In the midbrain, however, these parameters only became significantly different – showing an increase – at 10DPI, with other timepoints fluctuating non-significantly above the calculated mock group average. This suggests that astrocytes might not exhibit morphological or phenotypical changes indicative of astrogliosis in midbrain structures, like the SN, at or before 6DPI, which are

timepoints when VSV-GFP has not visibly penetrated yet midbrain-specific structures. This implies that astrocyte reactivity or the shift to reactive gliosis in assessed areas was potentially influenced by soluble factors (rather than viral particles), such as cytokines and chemokines. For instance, in the olfactory bulb and cerebellum, no viral antigen reactivity was observed via immunohistochemistry at 2DPI, yet significant increases in quantified astrocytic parameters were noted. It is, in conclusion, not entirely clear whether the astrocytic response was influenced in this study by signaling factors or cues other than the mere presence of the viral particles in a given area, such as gliotransmitters, which have the capacity to exert an effect on neuronal and synaptic functions (Brambilla et al., 2013).

Endogenous α-Synuclein Expression and its Interaction with VSV-GFP

The intrinsic expression of α-synuclein in the mouse brain is ubiquitous and widespread rather than being restricted to certain cellular populations or regions. This, given its presynaptic abundance and thus-far established properties, such as in vesicle trafficking, neurotransmitter release and neuronal communication (Taguchi et al., 2014; Taguchi et al., 2019). It is, however, highly concentrated in specific areas, such as the SN, which is integral to motor control, and the hippocampus, responsible for learning and memory (Mak et al., 2009). Other regions with high α-synuclein expression include the cerebral cortex, striatum, thalamus, hypothalamus, and the granule cell layer of the cerebellum (Lein et al., 2007; Taguchi et al., 2019). Within the olfactory bulb, α-synuclein is present in the glomerular layer, mitral cell layer, and granule cell layer in very similar amounts (Ubeda-beñon et al., 2010; Killinger et al., 2023). In the glomerular layer specifically, it resides in the presynaptic terminals of olfactory sensory neurons, establishing connections with mitral and tufted cells. This localization suggests that α-synuclein plays a role in olfactory information transmission and processing, where studies have shown that pathologies

of α-synuclein in the olfactory bulb can lead to disturbed olfaction by impacting synaptic transmission (Chen et al., 2019; Martin-Lopez et al., 2023). Utilizing the holocranohistochemistry technique, previous research from our lab and others demonstrated that α-synuclein is abundant within the olfactory epithelium and especially in olfactory sensory neurons, amongst other cell types (Tomlinson et al., 2017) (Bellani et al., 2010; Burré, 2015). These findings have been replicated in this work using routine immunohistochemistry to study α-synuclein expression patterns in the brains of wildtype mice from the main cohort, both mock and VSV-GFP-infected, as a proof of principle, but also to identify any qualitative or visual differences in the unfolded, monomeric α-synuclein expression within the olfactory epithelium and bulb, as well as to re-evaluate its distribution. The expression of α-synuclein throughout the brains of wildtype animals was consistent with previous findings and literature reports (Li et al., 2002; Tomlinson et al., 2017). α-Synuclein's expression, presented briefly in **figure 14**, seemed to be consistently localized to olfactory sensory neurons in the epithelium, and was occasionally observed in supporting cells and basal progenitor cells in both 2- and 6DPI animals and mock-treated mice analyzed. The staining appeared to be a mix of cytoplasmic and nuclear, with positive labeling extending to dendritic knobs reaching the epithelial surface where cilia are present. The axonal terminals of olfactory sensory neurons, forming the olfactory nerve bundles (CN-1), were also positively stained. These olfactory nerves synapse with dendrites from various cell types around the glomeruli in the bulb. In the bulb, however, α-synuclein's expression seemed more generalized and diffuse compared to the epithelium, maintaining consistent basal expression across different layers and cellular populations, agreeable with numerous previous reports on its ubiquitous endogenous expression in rostral mouse brain (Ubeda-beñon et al., 2010; Killinger et al., 2023).

There is emerging evidence that α-synuclein might interact with RNA viruses, as indicated by several co-localization studies and the subsequent pathogenesis of this protein in the context of infection. Such viruses used in infection paradigms included choices like the West Nile Virus (WNV), Japanese Encephalitis Virus (JEV), Influenza A Virus (IAV), but also the virus responsible for the very novel coronavirus disease, the severe acute respiratory syndrome coronavirus 2 (SARS-CoV-2), where an overlap between α-synuclein and viral proteins was recorded (Beatman et al., 2016; Marreiros et al., 2020; Wu et al., 2022). The olfactory bulb has been postulated as a potential initial site for the onset of alpha-synuclein pathology and the subsequent development of synucleinopathy-related diseases (Braak et al., 2003; Rey et al., 2018). This proposal is substantiated by multiple findings, including the loss of mitral cells in the olfactory bulb observed in PD (Sengoku et al., 2008; Beach et al., 2009; Cave et al., 2016), a notable prevalence of Lewy pathology in the olfactory bulb within synucleinopathy cases (Sengoku et al., 2008; Beach et al., 2010; Ubeda-Banon et al., 2010), and the occurrence of incidental Lewy pathology in the olfactory bulb (Beach et al., 2010). Here, I explored the co-localization of VSV-GFP administered nasally and α-synuclein in the olfactory epithelium, which is the first olfactory structure to see infection and constitutes the entry point of the virus into the brain, and the mammalian olfactory bulb, both of which have been shown to express α-synuclein endogenously and abundantly although never investigated previously in this context. As represented in **figure 15**, α-synuclein was found to co-localize with VSV-GFP in the olfactory nerves of olfactory sensory neurons residing in the olfactory epithelium. Regular staining of anti-VSV-GFP proteins yielded robust reactivity of viral particles in the axons forming the CN-I across different timepoints in infected mice, although it was the strongest in 4- and 6DPI mice. Whether there is a direct physical interaction between viral structures and α-

synuclein, such as seen during sequestration of antigens (or RNA) by host proteins, remains to be elucidated; α-synuclein was further found to co-localize with VSV-GFP in the glomeruli of the bulb, which are the first real synaptic juncture in the olfaction route, relaying odour signals from primary olfactory sensory neurons in the epithelium to secondary neurons in the bulb. This co-localization, once again, could be made possible when considering the native distribution of α-synuclein within the glomeruli and its enrichment in the axonal terminals found inside those spherical structures, but also by the virus' abundance recorded in those very glomeruli starting at 4DPI and onward. The signal overlap in the glomeruli had a punctae-like pattern, consistent with the nature of the axonal terminals and synapses occurring inside each glomerulus and yet again alluding to the manipulation of the CN-I and subsequent olfactory route by VSV-GFP to gain access to deeper brain structures.

α-Synuclein was reported to possess both anti-microbial and anti-viral properties, where an induction of this protein in nerve cells in response to ongoing microbial and viral invasion and an upregulation of its endogenous levels were linked to host immune responses (Park et al., 2016; Barbut et al., 2019). Further, α-synuclein in the enteric neurites of the upper gastrointestinal tract of pediatric patients positively correlated with the degree of acute and chronic inflammation in the intestinal wall (Stolzenberg et al., 2017). This has informed my immunoblotting of α-synuclein in the hemibrains of 6DPI mice and their PBS-administered counterparts to probe the endogenous levels of α-synuclein and see whether those levels possibly correlated (i.e., increased) with the infection at hand as seen with previous reports using different infectious paradigms. As shown in **figure 19**, total α-synuclein levels in the infected hemibrains trended as much as x1.25 fold higher than the mock-treated animals. Although the P value was 0.0571, there was no significance recorded between the two groups using Mann-Whitney test at

6DPI, a timepoint at which the microglial response was at its highest. Beatman et al., (2017) reported an increased expression level of α-synuclein *in vitro* as soon as 24 hours post-inoculation, which was further elevated at the 48-hour mark. It is thus possible that if hemibrains of 10DPI mice were to be analyzed and compared to mock-treated mice then the difference in measured levels between the two would be even more striking and reach significance. Significance could also have been possibly reached with a larger n of mice. On the other hand, when the viral burden was assessed, the 6DPI group returned much lower overall numbers compared to 2DPI hemibrains, indicating an efficient undergoing clearance of VSV-GFP. It is hence also possible that if samples of a higher replication-potent virus were immunoblotted then measured α-synuclein quantities would be even higher. This possibility could be explored in future work, enabling us draw links between levels of α-synuclein *in vivo* and the different timepoints of scarification and ultimately understanding whether α-synuclein is increased in an acute or chronic manner in a VSV-GFP infection. Another avenue that could be explored to delve deeper into the roots of this phenomenon and gain insight into the potential molecular mechanisms driving the observed increase in α-synuclein amounts would be a gene expression analysis using quantitative PCR. Such experimentation could provide pivotal information on mRNA levels of α-synuclein in infected group alongside the mock group at the timepoint of interest studied in the infectious course. If results mirrored the protein-level changes observed in the Western blot analysis, this would indicate an upregulation of the protein expression at the mRNA level rather than an altered rate of protein clearance and degradation.

Pathological Post-Translational Modifications of α-Synuclein are VSV-GFP-Induced

In post-mortem PD brain samples, α-synuclein undergoes various post-translational modifications that are associated with the disease's progression. Among these modifications,

phosphorylation, ubiquitination and the subsequent degradation via the autophagy-lysosome pathway, nitration, and aggregation are some of the most commonly observed (Spillantini et al., 1997, 1998; Lindersson et al., 2004; Arawaka et al., 2006; Oueslati et al., 2010). In PD, α-synuclein becomes abnormally phosphorylated at specific sites, notably serine 129 (Okochi et al., 2000). Phosphorylated α-synuclein has been found to accumulate in Lewy bodies and Lewy neurites, which are protein aggregates commonly associated with PD (Samuel et al., 2016). This informed the exploration of possible pS129-α-synuclein species in VSV-GFP infected mice with a focus on anterior olfactory structures. As conveyed in **figure 16**, there were no signs of phosphorylation in the olfactory epithelium and its immediate accessories in 6DPI and mock mice. The *Snca*-KO, similarly, omitted any positive staining of both α-synuclein and pS129-α-synuclein, ensuring a proper negative control for antibodies used. It is possible that technical conditions used for processing sections were not favourable for capturing phosphorylated species – if they existed – in the epithelium using the anti-pS129-α-synuclein EP1536Y (Abcam). Only one antigen retrieval method (boiling in Citrate buffer of pH = 6) was used to develop all tissues for matters of consistency. A recent study has reported that the detection of phosphorylated α-synuclein populations in the human temporal cortex in post-mortem dementia patients was highly affected by the antigen retrieval method and pre-treatments used, where phosphorylated nuclear species of α-synuclein were significantly more detectable following the pre-treatment with formic acid and the retrieval in an EDTA buffer of pH = 9 (Koss et al., 2022). Further experimentation building on this body of work and incorporating different variations of the epitope unmasking are necessary to investigate such possibility. The glomeruli of the olfactory bulb, however, conveyed a different story. Specific reactivity of pS129-α-synuclein, as indicated by the complete absence of signal in the *Snca*-KO mouse, was detected inside distinct glomeruli

along the glomerular layer. This localized phosphorylation was absent from analyzed mock-treated animals under identical imaging settings, giving extra confidence in ensuring the realness of the signal generated. Moreover, the signal distribution matches the pattern of α-synuclein and VSV-GFP colocalization seen in 6DPI mice, alluding to the possibility of the phosphorylation event either being a protective modification carried out by α-synuclein to combat the infection, or a consequence of the infection itself. Although the phosphorylation of α-synuclein at Ser129 is recognized to be the main post-translational modification in LBs, where more than 90% of its α-synuclein is phosphorylated versus 4% only in a non-diseased, non-LB brain, it is not entirely understood why this hyper-phosphorylation state evolves (i.e., its exact function) (Fujiwara et al., 2002; Anderson et al 2006). It is generally postulated, however, for pS129-α-synuclein to play a key role in the regulation of α-synuclein aggregation and neurotoxicity (Oueslati et al., 2010; Paleologou and El Agnaf, 2012; Tenreiro et al., 2014). Furthermore, phosphorylated S129-α-synuclein populations were recently characterized in the mitral cells of wildtype, non-diseased, mammalian mouse brain, and were spatially associated with proteinase-kinase-resistant α-synuclein, where mitral cells were reported to have a baseline phosphorylation of α-synuclein at Ser129 (Killinger et al., 2023). As such, the incidence rate of phosphorylation was also examined in mitral cells in this project to investigate the likelihood of infection in upregulating those phosphorylated species as seen in the glomeruli (Luk et al., 2012a; Masuda-Suzukake et al., 2013; Karampetsou et al., 2017; Okuzumi et al., 2018; Patterson et al., 2019). Substantial signal co-localization between EP1536Y and Syn-1 was detected in the mitral cell layer in 6DPI mice and to a much lesser extent in mock-treated mice. The greater portion of pS129-α-synuclein signal was nuclear, with occasional perinuclear and cytoplasmic signal co-localization observed which was entirely void from the *Snca*-KO. Of note, incidental LP has been reported in the

olfactory bulb of 30% of autopsied individuals over the age of 65 who did not display any clinical findings of parkinsonism or dementia (Adler et al., 2010). It is thus possible that – given the baseline phosphorylation of α-synuclein in those populations and the increase rate of phosphorylation in light of infection – disease initiation occurs within mitral cells of the olfactory bulb, or a systemic disease process is prominently manifested in the olfactory bulb due to its inherent inclination to accumulate pS129-α-synuclein.

The second investigation concerned the question of α-synuclein's tagging by the p62 cargo protein. The p62 protein possesses roles in various cellular processes, including autophagy, protein degradation, and signaling pathways (Pan et al., 2008; Liu et al., 2016). The interplay between p62 and α-synuclein has raised intriguing questions about their potential collaboration in disease mechanisms and progression (Pan et al., 2008; Watanbe et al., 2012; Tanji et al., 2015). P62 has been shown to accumulate in LBs in PD, which are highly ubiquitinated, suggesting its involvement in the clearance of aggregated proteins (Ebrahimi-Fakhari., 2011). Studies have indicated that p62 can interact with α-synuclein, facilitating its targeting to autophagosomes for subsequent degradation (Webb et al., 2003; Watanabe et al., 2012). This involvement of p62 in such critical aspects of α-synuclein proteostasis justified its use as a tool to indirectly monitor the ubiquitination of α-synuclein and infer about its turnover and degradation. As visually communicated in **figure 17**, the olfactory epithelium showed substantial signal co-localization between α-synuclein and p62 in 6DPI mice which appeared to be localized to olfactory sensory neurons and basal cells. This is indicative of ubiquitination of those α-synuclein populations and the subsequent trafficking for degradation via the lysosome-autophagy pathway. Interestingly, this co-localization of signal was greatly reduced in the mock group, with sparse spots of interactions that appeared to be mostly nuclear. Notably, areas of the epithelium

that demonstrated this signal overlap were ones that were closely related – spatially – to spots of positive viral infection as seen with the mapping of VSV-GFP reactivity in the mouse brain, offering evidence that implicate the VSV-GFP infection in the disturbance of α-synuclein in the epithelium. The same applied to glomeruli and mitral cells of 6DPI mice, where extensive signal overlap was seen in those structures in contrast with mock-treated mice. In glomeruli, there was a mixture of cytoplasmic signal overlap in periglomerular cells and robust intra-glomerular co-localization, which is congruent with the preference of VSV-GFP to localize to those axonal terminals on the inside. Although no infection was recorded in mitral cells in this project, some involvement of mitral cells was reported by Huneycutt et al., (1994) in regard to VSV-labelling, with a much larger involvement of the granule cells of the bulb. It could be possible that the timepoints chosen in this project were not ideal for capturing VSV-GFP when it is most present in mitral cells. This could explain the ubiquitination of α-synuclein and turnover – indirectly inferred from the co-localization observed with p62 – in the mitral cell layer of 6DPI mice. A shortcoming, or rather an area of improvement of such work in the future, would be the quantification of the degree and relative number of overlapping spots in 6DPI mice – with the possible addition of more timepoints in the infectious course as well – and the comparison of those values to mock-treated mice to structure a semiquantitative, more objective method of substantiating the visual impression of an overlap.

Stemming from the wealth of knowledge to date on the post-translational α-synuclein modifications observed in the intracellular fibrillar inclusions (i.e., aggregates) in diseased brains of PD patients, with phosphorylation at various serine residues and ubiquitination being amongst the most commonly observed (Tofaris et al., 2003; Oueslati et al., 2010; Paleologou and El Agnaf, 2012; Tenreiro et al., 2014), it was logical to further examine the aggregation of α-

synuclein in previous olfactory cellular populations. Interestingly, under technical conditions tested, specific reactivity indicative of α-synuclein aggregation was only observed in the olfactory epithelium. The olfactory bulb revealed diffuse, washed out, and dispersed staining that was not specific to any cellular population or intracellular compartment. This may hint that the antibody (MJFR14642, Abcam) requires further optimization of technical and developmental conditions to reveal staining patterns in the olfactory bulb. Nevertheless, as illustrated in **figure 18**, the control *Snca*-KO mouse returned a clean staining profile, omitting any signal symptomatic of cross-reactivity or unspecificity. In the wildtype counterparts, including both mock-treated and 6DPI mice, prevalent reactivity was recorded using the MJFR14642 antibody in what appeared to be olfactory sensory neurons judging from the midlevel-staining seen in the epithelium, which is congruent with the level of olfactory sensory neurons localization in the olfactory epithelium (Choi and Goldstein, 2018). Staining also largely materialized as nuclear staining in wildtype mice as judged by the H&E counterstain. Intriguingly, there were a couple visual remarks in the analyzed 6DPI sections that were not witnessed in the mock group; firstly, the dendrites of the olfactory sensory neurons extending from the cell bodies to the surface of the epithelium – where each ends in a dendritic knob from which around 20 to 35 cilia protrude (McClintock et al., 2020) – were positively labeled in a more extensive and apparent manner in contrast with mock-treated mice. Secondly, stronger MJFR14642 reactivity appearing as darker, denser, and dappled staining along parts of the epithelium where indications of viral-induced damage were recorded, such as the disintegration of cellular populations, mechanical displacement, and edema (Hüttenbrink et al., 2013). It is possible that these visual observations are VSV-GFP-induced and related to the resultant inflammatory processes affecting the epithelium since they are not present in mock-treated animals and completely absent in *Snca*-Ko

sections. Reports of α-synuclein aggregating and pathogenesis with reference to introduced infections, both bacterial and viral – including the most recent outbreak of coronavirus by SARS-CoV-2, are numerous (Labrie et al., 2017; Marreiros et al., 2020; Bantle et al., 2021 ; Kasen et al., 2022; Philippens et al., 2022; Semerdzhiev et al., 2022; Huynh et al., 2023). Studies have additionally shown an increase in detected endogenous amounts of α-synuclein in the brains of patients with acute WNV (Beatman et al., 2016), the SN of patients living with human immunodeficiency virus (HIV) (Khanlou et al., 2019), and the enteric neurites of the upper GI tract of pediatric patients with acute and chronic inflammation in the intestinal wall (Stolzenberg et al., 2017). In a viral model of H1N1 infection in C57BL mice, blocking of autophagosome formation and inhibition of autophagic flux was identified as a cell pathobiological mechanism leading to the formation of α-synuclein aggregates (Merreiros et al., 2020). Nevertheless, overall *SNCA*-mRNA levels were shown to spike up in sporadic PD brains an average of fourfold compared to normal, healthy brains, which is something that was initially observed in early-onset familial cases of the disease, where point mutations in *SNCA* or duplications and triplications in the gene copy number are the cause for the increased expression (Polymeropoulos et al., 1997; Krüger et al., 1998; Zarranz et al., 2004; Chiba-Falek et al., 2006). Hence, the mechanism or pathway responsible for the elevation in protein concentration might be dependent on a complex interaction between genetic factors, environmental exposure to certain toxins, and microbial and viral infections. Therefore, the elevated amounts of endogenous α-synuclein detected in 6DPI hemibrains in comparison with the mock group might be influenced by either a disturbance of proper and efficient protein degradation or an upregulation of the protein at the gene level, or even an interplay of both mechanisms. The aggregation, however, witnessed in the olfactory epithelium in both treatment groups, requires further investigation to determine whether the

VSV-GFP infection is potentially linked to an increased rate and prevalence of aggregated α-synuclein species. The presence of α-synuclein aggregates in the olfactory epithelium in PBS-treated animals might hint at a possible 'healthy' level of aggregation in the epithelium, which may either possess a protective role or is crucial for cellular homeostasis and normal functioning of cells it resides in. Future quantification efforts, including a larger n and the inclusiveness of more timepoints, will be able to decipher the viral infection's influence on aggregation.

To further investigate the speculated cellular and nuclear localization of the MJFR14642 signal to olfactory sensory neurons, co-labeling of aggregated-α-synuclein and either olfactory marker protein (OMP) or B-tubulin-III was performed. The OMP is a soluble acidic protein and has a cytoplasmic localization and is collectively expressed by mature olfactory sensory neurons, constituting a valid and reliable tool to visualize those neurons, whilst B-tubulin-III is found in the microtubule network of generally developing and immature neurons (Menezes and Luskin, 1994; Woo et al., 2002; Dibattista et al., 2021). Both markers revealed the outline of olfactory sensory neurons very clearly, with OMP showing a bigger population of neurons given the selective expression of this markers by mature neurons. Regardless, comparisons of both markers co-labeled with MJFR14642 showed interchangeable results, where merged images captured in separate channels revealed aggregated α-synuclein to be, indeed, both greatly specific to olfactory sensory neurons and have a preference for nuclear localization. The majority of signal representative of aggregates localized to the inside of the cellular outline defined by OMP and B-tubulin-III, which is the space the nuclear compartment inhabits.

The nuclear localization of the MJFR14642 signal was both intriguing and surprising to see, given how much emphasis is usually placed on the pathogenesis and aggregation of α-synuclein in the cytoplasmic compartment since Lewy pathology and inclusion bodies are

prominent and cytoplasmic/ axoplasmic in the brains of PD patients (Lewy J., 1994; Duda et al., 2000; Del Tredici and Braak., 2000-2013). Aggregation of α-synuclein has been recorded recently in the olfactory bulbs of C57BL mice overexpressing the mutated A53T form of human α-synuclein (Liu et al., 2023), but it was never recorded in the olfactory epithelium of rodents before. Although α-synuclein has a primarily presynaptic localization, studies have reported its presence in the nucleus (Maroteaux et al., 1988; Huang et al., 2011), and a recent study further substantiated those findings by confirming its intrinsic nuclear availability but also phosphorylation at serine 129 in investigations of post-mortem tissue obtained from dementia with Lewy body cases using a multidisciplinary approach (Koss et al.,2022). Moreover, intranuclear α-synuclein inclusions are a pathological feature of multiple system atrophy (MSA), alluding to the harmful potential of pathogenic α-synuclein species in human neurodegenerative diseases (Lin et al., 2004).

Research employing both *in vitro* and *in vivo* models indicates that nuclear α-synuclein has a role in controlling several nuclear processes, where it interacts with DNA and histones, thereby influencing gene transcription and DNA repair (Goers et al., 2003; Paiva et al., 2017; Pinho et al., 2019; Schaser et al., 2019; Davidi et al., 2020). Importantly, heightened expression of normal α-synuclein or disease-associated mutants, such as A30P, A53T, or G51D, augments α-synuclein levels; this escalation promotes the creation of intranuclear inclusions and leads to disturbances in gene transcription and nuclear import (Kontopoulos et al., 2006; Saddiqui et al., 2012; Fares et al., 2014; Lázaro et al., 2014; Chen et al., 2020). It is thus reasonable to speculate that the baseline availability of monomeric, unfolded α-synuclein in the nuclei of olfactory sensory neurons in the olfactory epithelium, as indicated by Syn-1 staining in both mock and infected animals in **figure 14**, might possess a physiological role and help regulate gene

transcription. The aggregation, on the other hand, has long been regarded as pathological and a deviation from the healthy, physiological α-synuclein populations found in the non-diseased brains and CNS of healthy patients.

More work needs to be done to investigate its presence in the olfactory epithelium of uninfected, seemingly healthy mice. As discussed, there might be a baseline availability of these aggregated species in olfactory sensory neurons due to a particular physiological role undiscovered yet, or merely an outcome of the constant exposure to foreign elements and pathogens in the nasal cavities as mice breathe. The qualitative observations of dendritic labeling and stronger localized reactivity in areas of damage in the epithelium in infected mice alludes to the possibility of the infection and the ensuing inflammation aggravating this baseline presence of such aggregated α-synuclein populations locally.

While the discovery of nuclear aggregation in these neurons is both intriguing and exciting, confirmatory approaches using tools such immuno-electron-microscopy (IEM) and Z-stacking are necessary as to not overcall the localization of a signal to one organelle. The use of two valid olfactory sensory neurons markers, however, on multiple sections in co-localization studies in this project with interchangeable and similar results is highly suggestive of this nuclear aggregation.

It remains unclear why the neural population of the olfactory epithelium was the only one to reveal these aggregates in anterior olfactory structures. It is possible that, much like the EP1536Y antibody against pS129-α-synuclein, the conditions used to develop and stain with the MJFR14642 antibody were not favourable to detect such aggregates in the olfactory bulb. Further exploration of this possibility utilizing various antigen retrieval methods and a combination of pre- and post-treatment imaging are necessary to determine whether the absence

of pS129-α-synuclein signals in the olfactory epithelium and of aggregated-α-synuclein in the olfactory bulb are due to technical aspects or distinct physiological responses in the context of a neurotropic infection.

Conclusions

Parkinson disease, a well-documented form of neuronal synucleinopathy, occurs due to a combination of genetic risk, environmental exposure(s), and lifestyle elements, as so many other complex, late-onset disorders in humans. Environmental factors, such as viral infections, have been suggested as potential initiators and contributors to the development of this neurodegenerative illness, especially in its sporadic form, where single gene risk factors are rare and fewer than 20 % of all PD cases have been linked to variants with low individual impact at >90 loci throughout the human genome. The dual-hit hypothesis proposed by Braak and Del Tredici envisions microbial (or neurotoxicant) pathogens that may incite disease pathology in neuronal subpopulations of the olfactory bulb and enteric plexus of the gut, congruent with the prodromal symptoms of hyposmia and constipation, respectively, which are seen in the majority of PD patients (Braak et al., 2003; Hawkes et al; 2007). For the purposes of this thesis, I set out to document the tropism and progressiveness of a RNA neurotropic pathogen, VSV-GFP, nasally administered to C57BL/6 mice of the WT background, which constituted the infection model, and the concurrent inflammation concerned with glial cells, whilst investigating major pathological modifications of α-synuclein potentially influenced by this very infection and the ensuing inflammatory response. It appears that VSV-GFP can generate a strong and progressive, but variable, infection in the rhinencephalon and more caudal CNS structures, reaching areas critical in the development of PD, such as the SN, and is accompanied by robust microglial and astrocytic responses that are morphologically pro-inflammatory. This leads to the labelling of α-

synuclein for degradation by the p62 cargo protein in anterior olfactory structures, the S129-phosphorylation of α-synuclein in the glomeruli and mitral cells specifically, and the generation of rare α-synuclein aggregates within olfactory sensory neurons, alongside an increase in endogenous α-synuclein protein in animals 6DPI.

In summary, this thesis describes a viral infection paradigm of VSV-GFP and the ensuing inflammatory response in mouse brain and characterizes select changes in the homeostasis of α-synuclein in affected anterior olfactory circuitry. Future studies will be able to build on this viral model (as well as additional ones) to determine whether alterations in α-synuclein metabolites, including rare aggregates, of infected mice will persist over time, have the capacity to propagate via transsynaptic spread or will be entirely degraded, and whether these synucleinopathy-informed changes can induce neural death. Last but not least, it remains to be seen whether such changes are linked to abnormal olfaction in mice with possible relevance to the hyposmia of PD.

References

Abbott, R. D., Petrovitch, H., White, L. R., Masaki, K. H., Tanner, C. M., Curb, J. D., Grandinetti, A., Blanchette, P. L., Popper, J. S., & Ross, G. W. (2001). Frequency of bowel movements and the future risk of Parkinson's disease. *Neurology*, *57*(3), 456–462. https://doi.org/10.1212/wnl.57.3.456

Abbott, R. D., Ross, G. W., White, L. R., Tanner, C. M., Masaki, K. H., Nelson, J. S., Curb, J. D., & Petrovitch, H. (2005). Excessive daytime sleepiness and subsequent development of Parkinson disease. *Neurology*, *65*(9), 1442–1446. https://doi.org/10.1212/01.wnl.0000183056.89590.0d

Alderson, T. R., & Markley, J. L. (2013). Biophysical characterization of α-synuclein and its controversial structure. *Intrinsically disordered proteins*, *1*(1), 18–39. https://doi.org/10.4161/idp.26255

Allen Reish, H. E., & Standaert, D. G. (2015). Role of α-synuclein in inducing innate and adaptive immunity in Parkinson disease. *Journal of Parkinson's disease*, *5*(1), 1–19. https://doi.org/10.3233/JPD-140491

Andersson, T., Mohammed, A. K., Henriksson, B. G., Wickman, C., Norrby, E., Schultzberg, M., & Kristensson, K. (1993). Immunohistochemical and behaviour pharmacological analysis of rats inoculated intranasally with vesicular stomatitis virus. *Journal of chemical neuroanatomy*, *6*(1), 7–18. https://doi.org/10.1016/0891-0618(93)90003-m

Anderson, J. P., Walker, D. E., Goldstein, J. M., de Laat, R., Banducci, K., Caccavello, R. J., Barbour, R., Huang, J., Kling, K., Lee, M., Diep, L., Keim, P. S., Shen, X., Chataway, T., Schlossmacher, M. G., Seubert, P., Schenk, D., Sinha, S., Gai, W. P., & Chilcote, T. J. (2006). Phosphorylation of Ser-129 is the dominant pathological modification of alpha-synuclein in familial and sporadic Lewy body disease. *The Journal of biological chemistry*, *281*(40), 29739–29752. https://doi.org/10.1074/jbc.M600933200

Arawaka, S., Wada, M., Goto, S., Karube, H., Sakamoto, M., Ren, C. H., Koyama, S., Nagasawa, H., Kimura, H., Kawanami, T., Kurita, K., Tajima, K., Daimon, M., Baba, M., Kido, T., Saino, S., Goto, K., Asao, H., Kitanaka, C., Takashita, E., … Kato, T. (2006). The role of G-protein-coupled receptor kinase 5 in pathogenesis of sporadic Parkinson's disease. The Journal of neuroscience : the official journal of the Society for Neuroscience, 26(36), 9227–9238. https://doi.org/10.1523/JNEUROSCI.0341-06.2006

Atias, M., Tevet, Y., Sun, J., Stavsky, A., Tal, S., Kahn, J., Roy, S., & Gitler, D. (2019). Synapsins regulate α-synuclein functions. *Proceedings of the National Academy of Sciences of the United States of America*, *116*(23), 11116–11118. https://doi.org/10.1073/pnas.1903054116

Baltic, S., Perovic, M., Mladenovic, A. *et al.* α-Synuclein is expressed in different tissues during human fetal development. *J Mol Neurosci* 22, 199–203 (2004). https://doi.org/10.1385/JMN:22:3:199

Bantle, C. M., Rocha, S. M., French, C. T., Phillips, A. T., Tran, K., Olson, K. E., Bass, T. A., Aboellail, T., Smeyne, R. J., & Tjalkens, R. B. (2021). Astrocyte inflammatory signaling mediates α-synuclein aggregation and dopaminergic neuronal loss following viral encephalitis. Experimental neurology, 346, 113845. https://doi.org/10.1016/j.expneurol.2021.113845

Barbut, D., Stolzenberg, E., & Zasloff, M. (2019). Gastrointestinal Immunity and Alpha-Synuclein. Journal of Parkinson's disease, 9(s2), S313–S322. https://doi.org/10.3233/JPD-191702

Bassil, F., Fernagut, P. O., Bezard, E., Pruvost, A., Leste-Lasserre, T., Hoang, Q. Q., Ringe, D., Petsko, G. A., & Meissner, W. G. (2016). Reducing C-terminal truncation mitigates synucleinopathy and neurodegeneration in a transgenic model of multiple system atrophy. Proceedings of the National Academy of Sciences of the United States of America, 113(34), 9593–9598. https://doi.org/10.1073/pnas.1609291113

Beach, T. G., Adler, C. H., Sue, L. I., Vedders, L., Lue, L., White Iii, C. L., Akiyama, H., Caviness, J. N., Shill, H. A., Sabbagh, M. N., Walker, D. G., & Arizona Parkinson's Disease Consortium (2010). Multi-organ distribution of phosphorylated alpha-synuclein histopathology in subjects with Lewy body disorders. Acta neuropathologica, 119(6), 689–702. https://doi.org/10.1007/s00401-010-0664-3

Beatman EL, Massey A, Shives KD, et al. Alpha-Synuclein Expression Restricts RNA Viral Infections in the Brain. Perlman S, ed. *J Virol*. 2016;90(6):2767-2782. doi:10.1128/JVI.02949-15

Bellani, S., Sousa, V. L., Ronzitti, G., Valtorta, F., Meldolesi, J., & Chieregatti, E. (2010). The regulation of synaptic function by alpha-synuclein. *Communicative & integrative biology*, *3*(2), 106–109. https://doi.org/10.4161/cib.3.2.10964

Ben Haim, L., Carrillo-de Sauvage, M. A., Ceyzériat, K., & Escartin, C. (2015). Elusive roles for reactive astrocytes in neurodegenerative diseases. *Frontiers in cellular neuroscience*, *9*, 278. https://doi.org/10.3389/fncel.2015.00278

Bennett, D. A., Schneider, J. A., Wilson, R. S., Bienias, J. L., & Arnold, S. E. (2004). Neurofibrillary tangles mediate the association of amyloid load with clinical Alzheimer disease and level of cognitive function. *Archives of neurology*, *61*(3), 378–384. https://doi.org/10.1001/archneur.61.3.378

Bi, Z., Barna, M., Komatsu, T., & Reiss, C. S. (1995). Vesicular stomatitis virus infection of the central nervous system activates both innate and acquired immunity. *Journal of virology*, *69*(10), 6466–6472. https://doi.org/10.1128/JVI.69.10.6466-6472.1995

Bjørkøy, G., Lamark, T., Pankiv, S., Øvervatn, A., Brech, A., & Johansen, T. (2009). Monitoring autophagic degradation of p62/SQSTM1. *Methods in enzymology*, *452*, 181–197. https://doi.org/10.1016/S0076-6879(08)03612-4

Braak, H., Del Tredici, K., Rüb, U., de Vos, R. A., Jansen Steur, E. N., & Braak, E. (2003). Staging of brain pathology related to sporadic Parkinson's disease. *Neurobiology of aging*, *24*(2), 197–211. https://doi.org/10.1016/s0197-4580(02)00065-9

Brambilla, L., Martorana, F., & Rossi, D. (2013). Astrocyte signaling and neurodegeneration: new insights into CNS disorders. Prion, 7(1), 28–36. https://doi.org/10.4161/pri.22512

Bu, X. L., Wang, X., Xiang, Y., Shen, L. L., Wang, Q. H., Liu, Y. H., Jiao, S. S., Wang, Y. R., Cao, H. Y., Yi, X., Liu, C. H., Deng, B., Yao, X. Q., Xu, Z. Q., Zhou, H. D., & Wang, Y. J. (2015). The association between infectious burden and Parkinson's disease: A case-control study. *Parkinsonism & related disorders*, *21*(8), 877–881. https://doi.org/10.1016/j.parkreldis.2015.05.015

Burré J. (2015). The Synaptic Function of α-Synuclein. *Journal of Parkinson's disease*, *5*(4), 699–713. https://doi.org/10.3233/JPD-150642

Burré, J., Sharma, M., Tsetsenis, T., Buchman, V., Etherton, M. R., & Südhof, T. C. (2010). Alpha-synuclein promotes SNARE-complex assembly in vivo and in vitro. *Science (New York, N.Y.)*, *329*(5999), 1663–1667. https://doi.org/10.1126/science.1195227

Cave, J. W., Fujiwara, N., Weibman, A. R., & Baker, H. (2016). Cytoarchitectural changes in the olfactory bulb of Parkinson's disease patients. NPJ Parkinson's disease, 2, 16011. https://doi.org/10.1038/npjparkd.2016.11

Chen, F., Liu, W., Liu, P., Wang, Z., Zhou, Y., Liu, X., & Li, A. (2021). α-Synuclein aggregation in the olfactory bulb induces olfactory deficits by perturbing granule cells and granular-mitral synaptic transmission. NPJ Parkinson's disease, 7(1), 114. https://doi.org/10.1038/s41531-021-00259-7

Chen, V., Moncalvo, M., Tringali, D., Tagliafierro, L., Shriskanda, A., Ilich, E., Dong, W., Kantor, B., & Chiba-Falek, O. (2020). The mechanistic role of alpha-synuclein in the nucleus: impaired nuclear function caused by familial Parkinson's disease SNCA mutations. Human molecular genetics, 29(18), 3107–3121. https://doi.org/10.1093/hmg/ddaa183

Chiba-Falek, O., Lopez, G. J., & Nussbaum, R. L. (2006). Levels of alpha-synuclein mRNA in sporadic Parkinson disease patients. Movement disorders : official journal of the Movement Disorder Society, 21(10), 1703–1708. https://doi.org/10.1002/mds.21007

Choi, R., & Goldstein, B. J. (2018). Olfactory epithelium: Cells, clinical disorders, and insights from an adult stem cell niche. Laryngoscope investigative otolaryngology, 3(1), 35–42. https://doi.org/10.1002/lio2.135

Ciavarra RP, Machida M, Lundberg PS, et al. Controllable and uncontrollable stress differentially impact pathogenicity and survival in a mouse model of viral encephalitis. *J Neuroimmunol*. 2018;319:130-141. doi: 10.1016/j.jneuroim.2018.02.014

Colpitts, T. M., Conway, M. J., Montgomery, R. R., & Fikrig, E. (2012). West Nile Virus: biology, transmission, and human infection. *Clinical microbiology reviews*, *25*(4), 635–648. https://doi.org/10.1128/CMR.00045-12

Davidi, D., Schechter, M., Elhadi, S. A., Matatov, A., Nathanson, L., & Sharon, R. (2020). α-Synuclein Translocates to the Nucleus to Activate Retinoic-Acid-Dependent Gene Transcription. iScience, 23(3), 100910. https://doi.org/10.1016/j.isci.2020.100910

Del Tredici K, Braak H. Idiopathic Parkinson's Disease: Staging an α-Synucleinopathy with a Predictable Pathoanatomy. In: Madame Curie Bioscience Database [Internet]. Austin (TX): Landes Bioscience; 2000-2013. Available from: https://www.ncbi.nlm.nih.gov/books/NBK6077/

Delic, V., Chandra, S., Abdelmotilib, H., Maltbie, T., Wang, S., Kem, D., Scott, H. J., Underwood, R. N., Liu, Z., Volpicelli-Daley, L. A., & West, A. B. (2018). Sensitivity and specificity of phospho-Ser129 α-synuclein monoclonal antibodies. *The Journal of comparative neurology*, *526*(12), 1978–1990. https://doi.org/10.1002/cne.24468

Diamond, G., Beckloff, N., Weinberg, A., & Kisich, K. O. (2009). The roles of antimicrobial peptides in innate host defense. *Current pharmaceutical design*, *15*(21), 2377–2392. https://doi.org/10.2174/138161209788682325

Dibattista, M., Al Koborssy, D., Genovese, F., & Reisert, J. (2021). The functional relevance of olfactory marker protein in the vertebrate olfactory system: a never-ending story. Cell and tissue research, 383(1), 409–427. https://doi.org/10.1007/s00441-020-03349-9

Doty RL. Olfaction in Parkinson's disease and related disorders. Published online 2013:63.

Duda, J. E., Lee, V. M., & Trojanowski, J. Q. (2000). Neuropathology of synuclein aggregates. *Journal of neuroscience research*, *61*(2), 121–127. https://doi.org/10.1002/1097-4547(20000715)61:2<121::AID-JNR1>3.0.CO;2-4

Ebrahimi-Fakhari, D., Cantuti-Castelvetri, I., Fan, Z., Rockenstein, E., Masliah, E., Hyman, B. T., McLean, P. J., & Unni, V. K. (2011). Distinct roles in vivo for the ubiquitin-proteasome system and the autophagy-lysosomal pathway in the degradation of α-synuclein. The Journal of neuroscience : the official journal of the Society for Neuroscience, 31(41), 14508–14520. https://doi.org/10.1523/JNEUROSCI.1560-11.2011

Fares, M. B., Ait-Bouziad, N., Dikiy, I., Mbefo, M. K., Jovičić, A., Kiely, A., Holton, J. L., Lee, S. J., Gitler, A. D., Eliezer, D., & Lashuel, H. A. (2014). The novel Parkinson's disease

linked mutation G51D attenuates in vitro aggregation and membrane binding of α-synuclein, and enhances its secretion and nuclear localization in cells. Human molecular genetics, 23(17), 4491–4509. https://doi.org/10.1093/hmg/ddu165

Fensterl, V., Wetzel, J. L., Ramachandran, S., Ogino, T., Stohlman, S. A., Bergmann, C. C., ... & Sen, G. C. (2012). Interferon-induced Ifit2/ISG54 protects mice from lethal VSV neuropathogenesis. *PLoS pathogens*, *8*(5), e1002712. https://doi.org/10.1371/journal.ppat.1002712

Ferrer I. (2017). Diversity of astroglial responses across human neurodegenerative disorders and brain aging. *Brain pathology (Zurich, Switzerland)*, *27*(5), 645–674. https://doi.org/10.1111/bpa.12538

Forger, J. M., 3rd, Bronson, R. T., Huang, A. S., & Reiss, C. S. (1991). Murine infection by vesicular stomatitis virus: initial characterization of the H-2d system. *Journal of virology*, *65*(9), 4950–4958. https://doi.org/10.1128/JVI.65.9.4950-4958.1991

Fujiwara H., Hasegawa M., Dohmae N., Kawashima A., Masliah E., Goldberg M. S., et al. (2002). alpha-Synuclein is phosphorylated in synucleinopathy lesions. *Nat. Cell Biol*. 4, 160–164 10.1038/ncb748

Furudono, Y., Cruz, G. & Lowe, G. Glomerular input patterns in the mouse olfactory bulb evoked by retronasal odor stimuli. BMC Neurosci 14, 45 (2013). https://doi.org/10.1186/1471-2202-14-45

Ghanem, S. S., Majbour, N. K., Vaikath, N. N., Ardah, M. T., Erskine, D., Jensen, N. M., Fayyad, M., Sudhakaran, I. P., Vasili, E., Melachroinou, K., Abdi, I. Y., Poggiolini, I., Santos, P., Dorn, A., Carloni, P., Vekrellis, K., Attems, J., McKeith, I., Outeiro, T. F., Jensen, P. H., … El-Agnaf, O. M. A. (2022). α-Synuclein phosphorylation at serine 129 occurs after initial protein deposition and inhibits seeded fibril formation and toxicity. *Proceedings of the National Academy of Sciences of the United States of America*, *119*(15), e2109617119. https://doi.org/10.1073/pnas.2109617119

Goers, J., Manning-Bog, A. B., McCormack, A. L., Millett, I. S., Doniach, S., Di Monte, D. A., Uversky, V. N., & Fink, A. L. (2003). Nuclear localization of alpha-synuclein and its interaction with histones. Biochemistry, 42(28), 8465–8471. https://doi.org/10.1021/bi0341152

Gómez-Benito M, Granado N, García-Sanz P, Michel A, Dumoulin M, Moratalla R. Modeling Parkinson's Disease With the Alpha-Synuclein Protein. *Front Pharmacol*. 2020;11:356. doi:10.3389/fphar.2020.00356

Grosch J, Winkler J, Kohl Z. Early Degeneration of Both Dopaminergic and Serotonergic Axons – A Common Mechanism in Parkinson's Disease. *Front Cell Neurosci*. 2016;10. doi:10.3389/fncel.2016.00293

Guo, Y., Lennon, V. A., Parisi, J. E., Popescu, B., Vasquez, C., Pittock, S. J., Howe, C. L., & Lucchinetti, C. F. (2022). Spectrum of sublytic astrocytopathy in neuromyelitis optica. *Brain : a journal of neurology*, *145*(4), 1379–1390. https://doi.org/10.1093/brain/awab394

Harvey, J. D., & Heinbockel, T. (2018). Neuromodulation of Synaptic Transmission in the Main Olfactory Bulb. *International journal of environmental research and public health*, *15*(10), 2194. https://doi.org/10.3390/ijerph15102194

Hawkes, C. H., Del Tredici, K., & Braak, H. (2007). Parkinson's disease: a dual-hit hypothesis. *Neuropathology and applied neurobiology*, *33*(6), 599–614. https://doi.org/10.1111/j.1365-2990.2007.00874.x

Helwany M, Bordoni B. Neuroanatomy, Cranial Nerve 1 (Olfactory) [Updated 2022 Aug 8]. In: StatPearls [Internet]. Treasure Island (FL): StatPearls Publishing; 2023 Jan-. Available from: https://www.ncbi.nlm.nih.gov/books/NBK556051/

Henderson MX, Trojanowski JQ, Lee VM-Y. α-Synuclein pathology in Parkinson's disease and related α-synucleinopathies. *Neuroscience Letters*. 2019;709:134316. doi:10.1016/j.neulet.2019.134316

Hirsch L, Jette N, Frolkis A, Steeves T, Pringsheim T. The Incidence of Parkinson's Disease: A Systematic Review and Meta-Analysis. *Neuroepidemiology*. 2016;46(4):292 300. doi:10.1159/000445751

Huang, Z., Xu, Z., Wu, Y., & Zhou, Y. (2011). Determining nuclear localization of alpha-synuclein in mouse brains. Neuroscience, 199, 318–332. https://doi.org/10.1016/j.neuroscience.2011.10.016

Huneycutt, B. S., Plakhov, I. V., Shusterman, Z., Bartido, S. M., Huang, A., Reiss, C. S., & Aoki, C. (1994). Distribution of vesicular stomatitis virus proteins in the brain of BALB/c mice following intranasal inoculation: An immunohistochemical analysis. Brain Research, 635(1–2), 81–95. https://doi.org/10.1016/0006-8993(94)91426-5

Hüttenbrink, K. B., Hummel, T., Berg, D., Gasser, T., & Hähner, A. (2013). Olfactory dysfunction: common in later life and early warning of neurodegenerative disease. Deutsches Arzteblatt international, 110(1-2), 1–e1. https://doi.org/10.3238/arztebl.2013.0001

Huynh, V. A., Takala, T. M., Murros, K. E., Diwedi, B., & Saris, P. E. J. (2023). Desulfovibrio bacteria enhance alpha-synuclein aggregation in a Caenorhabditis elegans model of Parkinson's disease. Frontiers in cellular and infection microbiology, 13, 1181315. https://doi.org/10.3389/fcimb.2023.1181315

Jankowsky, J. L., Melnikova, T., Fadale, D. J., Xu, G. M., Slunt, H. H., Gonzales, V., Younkin, L. H., Younkin, S. G., Borchelt, D. R., & Savonenko, A. V. (2005). Environmental enrichment mitigates cognitive deficits in a mouse model of Alzheimer's disease. *The Journal of*

neuroscience : the official journal of the Society for Neuroscience, *25*(21), 5217–5224. https://doi.org/10.1523/JNEUROSCI.5080-04.2005

Kalia LV, Lang AE. Parkinson's disease. *The Lancet*. 2015;386(9996):896-912. doi:10.1016/S0140-6736(14)61393-3

Karampetsou, M., Ardah, M. T., Semitekolou, M., Polissidis, A., Samiotaki, M., Kalomoiri, M., Majbour, N., Xanthou, G., El-Agnaf, O. M. A., & Vekrellis, K. (2017). Phosphorylated exogenous alpha-synuclein fibrils exacerbate pathology and induce neuronal dysfunction in mice. Scientific reports, 7(1), 16533. https://doi.org/10.1038/s41598-017-15813-8

Kasen, A., Houck, C., Burmeister, A. R., Sha, Q., Brundin, L., & Brundin, P. (2022). Upregulation of α-synuclein following immune activation: Possible trigger of Parkinson's disease. Neurobiology of Disease, 166, 105654. https://doi.org/10.1016/j.nbd.2022.105654

Kaur R, Mehan S, Singh S. Understanding multifactorial architecture of Parkinson's disease: pathophysiology to management. *Neurol Sci*. 2019;40(1):13-23. doi:10.1007/s10072-018-3585-x

Khanlou, N., Moore, D. J., Chana, G., Cherner, M., Lazzaretto, D., Dawes, S., Grant, I., Masliah, E., Everall, I. P., & HNRC Group (2009). Increased frequency of alpha-synuclein in the substantia nigra in human immunodeficiency virus infection. Journal of neurovirology, 15(2), 131–138. https://doi.org/10.1080/13550280802578075

Killinger, B. A., Mercado, G., Choi, S., Tittle, T., Chu, Y., Brundin, P., & Kordower, J. H. (2023). Distribution of phosphorylated alpha-synuclein in non-diseased brain implicates olfactory bulb mitral cells in synucleinopathy pathogenesis. *NPJ Parkinson's disease*, *9*(1), 43. https://doi.org/10.1038/s41531-023-00491-3

Kontopoulos, E., Parvin, J. D., & Feany, M. B. (2006). Alpha-synuclein acts in the nucleus to inhibit histone acetylation and promote neurotoxicity. Human molecular genetics, 15(20), 3012–3023. https://doi.org/10.1093/hmg/ddl243

Kordower, J. H., Chu, Y., Hauser, R. A., Freeman, T. B., & Olanow, C. W. (2008). Lewy body-like pathology in long-term embryonic nigral transplants in Parkinson's disease. Nature medicine, 14(5), 504–506. https://doi.org/10.1038/nm1747

Kramer, M. L., & Schulz-Schaeffer, W. J. (2007). Presynaptic alpha-synuclein aggregates, not Lewy bodies, cause neurodegeneration in dementia with Lewy bodies. *The Journal of neuroscience : the official journal of the Society for Neuroscience*, *27*(6), 1405–1410. https://doi.org/10.1523/JNEUROSCI.4564-06.2007

Krüger, R., Kuhn, W., Müller, T., Woitalla, D., Graeber, M., Kösel, S., Przuntek, H., Epplen, J. T., Schöls, L., & Riess, O. (1998). Ala30Pro mutation in the gene encoding alpha-synuclein in Parkinson's disease. Nature genetics, 18(2), 106–108. https://doi.org/10.1038/ng0298-106

Labrie, V., & Brundin, P. (2017). Alpha-Synuclein to the Rescue: Immune Cell Recruitment by Alpha-Synuclein during Gastrointestinal Infection. Journal of innate immunity, 9(5), 437–440. https://doi.org/10.1159/000479653

Lashuel, H. A., Mahul-Mellier, A. L., Novello, S., Hegde, R. N., Jasiqi, Y., Altay, M. F., Donzelli, S., DeGuire, S. M., Burai, R., Magalhães, P., Chiki, A., Ricci, J., Boussouf, M., Sadek, A., Stoops, E., Iseli, C., & Guex, N. (2022). Revisiting the specificity and ability of phospho-S129 antibodies to capture alpha-synuclein biochemical and pathological diversity. *NPJ Parkinson's disease*, *8*(1), 136. https://doi.org/10.1038/s41531-022-00388-7

Lawrenson, C., Bares, M., Kamondi, A. et al. The mystery of the cerebellum: clues from experimental and clinical observations. cerebellum ataxias 5, 8 (2018). https://doi.org/10.1186/s40673-018-0087-9

Lázaro, D. F., Rodrigues, E. F., Langohr, R., Shahpasandzadeh, H., Ribeiro, T., Guerreiro, P., Gerhardt, E., Kröhnert, K., Klucken, J., Pereira, M. D., Popova, B., Kruse, N., Mollenhauer, B., Rizzoli, S. O., Braus, G. H., Danzer, K. M., & Outeiro, T. F. (2014). Systematic comparison of the effects of alpha-synuclein mutations on its oligomerization and aggregation. PLoS genetics, 10(11), e1004741. https://doi.org/10.1371/journal.pgen.1004741

Lee, K. W., Chen, W., Junn, E., Im, J. Y., Grosso, H., Sonsalla, P. K., Feng, X., Ray, N., Fernandez, J. R., Chao, Y., Masliah, E., Voronkov, M., Braithwaite, S. P., Stock, J. B., & Mouradian, M. M. (2011). Enhanced phosphatase activity attenuates α-synucleinopathy in a mouse model. *The Journal of neuroscience : the official journal of the Society for Neuroscience*, *31*(19), 6963–6971. https://doi.org/10.1523/JNEUROSCI.6513-10.2011

Lein, E. S., Hawrylycz, M. J., Ao, N., Ayres, M., Bensinger, A., Bernard, A., Boe, A. F., Boguski, M. S., Brockway, K. S., Byrnes, E. J., Chen, L., Chen, L., Chen, T. M., Chin, M. C., Chong, J., Crook, B. E., Czaplinska, A., Dang, C. N., Datta, S., Dee, N. R., … Jones, A. R. (2007). Genome-wide atlas of gene expression in the adult mouse brain. *Nature*, *445*(7124), 168–176. https://doi.org/10.1038/nature05453

Li, J.-, Henning Jensen, P., & Dahlström, A. (2002). Differential localization of alpha-, beta- and gamma-synucleins in the rat CNS. *Neuroscience*, *113*(2), 463–478. https://doi.org/10.1016/s0306-4522(02)00143-4

Liddelow, S. A., Guttenplan, K. A., Clarke, L. E., Bennett, F. C., Bohlen, C. J., Schirmer, L., Bennett, M. L., Münch, A. E., Chung, W. S., Peterson, T. C., Wilton, D. K., Frouin, A., Napier, B. A., Panicker, N., Kumar, M., Buckwalter, M. S., Rowitch, D. H., Dawson, V. L., Dawson, T. M., Stevens, B., … Barres, B. A. (2017). Neurotoxic reactive astrocytes are induced by activated microglia. Nature, 541(7638), 481–487. https://doi.org/10.1038/nature21029

Lin, W. L., DeLucia, M. W., & Dickson, D. W. (2004). Alpha-synuclein immunoreactivity in neuronal nuclear inclusions and neurites in multiple system atrophy. Neuroscience letters, 354(2), 99–102. https://doi.org/10.1016/j.neulet.2003.09.075

Liu, W. J., Ye, L., Huang, W. F., Guo, L. J., Xu, Z. G., Wu, H. L., Yang, C., & Liu, H. F. (2016). p62 links the autophagy pathway and the ubiquitin-proteasome system upon ubiquitinated protein degradation. *Cellular & molecular biology letters*, *21*, 29. https://doi.org/10.1186/s11658-016-0031-z

Logan, T., Bendor, J., Toupin, C., Thorn, K., & Edwards, R. H. (2017). α-Synuclein promotes dilation of the exocytotic fusion pore. *Nature neuroscience*, *20*(5), 681–689. https://doi.org/10.1038/nn.4529

Logroscino G. The Role of Early Life Environmental Risk Factors in Parkinson Disease: What Is the Evidence? *Environ Health Perspect*. 2005;113(9):1234-1238. doi:10.1289/ehp.7573

Lowe J. Lewy bodies. In *Neurodegenerative Diseases.* Ed. DP Calne. Philadelphia, PA: Saunders, 1994; 51–69

Luk, K. C., Kehm, V., Carroll, J., Zhang, B., O'Brien, P., Trojanowski, J. Q., & Lee, V. M. (2012). Pathological α-synuclein transmission initiates Parkinson-like neurodegeneration in nontransgenic mice. Science (New York, N.Y.), 338(6109), 949–953. https://doi.org/10.1126/science.1227157

Mak, S. K., McCormack, A. L., Langston, J. W., Kordower, J. H., & Di Monte, D. A. (2009). Decreased alpha-synuclein expression in the aging mouse substantia nigra. *Experimental neurology*, *220*(2), 359–365. https://doi.org/10.1016/j.expneurol.2009.09.021

Maroteaux, L., Campanelli, J. T., & Scheller, R. H. (1988). Synuclein: a neuron-specific protein localized to the nucleus and presynaptic nerve terminal. *The Journal of neuroscience : the official journal of the Society for Neuroscience*, *8*(8), 2804–2815. https://doi.org/10.1523/JNEUROSCI.08-08-02804.1988

Marreiros, R., Müller-Schiffmann, A., Trossbach, S. V., Prikulis, I., Hänsch, S., Weidtkamp-Peters, S., Moreira, A. R., Sahu, S., Soloviev, I., Selvarajah, S., Lingappa, V. R., & Korth, C. (2020). Disruption of cellular proteostasis by H1N1 influenza A virus causes α-synuclein aggregation. *Proceedings of the National Academy of Sciences of the United States of America*, *117*(12), 6741–6751. https://doi.org/10.1073/pnas.1906466117

Marques, M., Ramos, B., Soares, A. R., & Ribeiro, D. (2019). Cellular Proteostasis During Influenza A Virus Infection-Friend or Foe?. *Cells*, *8*(3), 228. https://doi.org/10.3390/cells8030228

Martin-Lopez, E., Vidyadhara, D. J., Liberia, T., Meller, S. J., Harmon, L. E., Hsu, R. M., Spence, N., Brennan, B., Han, K., Yücel, B., Chandra, S. S., & Greer, C. A. (2023). α-Synuclein Pathology and Reduced Neurogenesis in the Olfactory System Affect Olfaction in a Mouse Model of Parkinson's Disease. The Journal of neuroscience : the official journal of the Society for Neuroscience, 43(6), 1051–1071. https://doi.org/10.1523/JNEUROSCI.1526-22.2022

Masliah, E., Rockenstein, E., Veinbergs, I., Mallory, M., Hashimoto, M., Takeda, A., Sagara, Y., Sisk, A., & Mucke, L. (2000). Dopaminergic loss and inclusion body formation in alpha-synuclein mice: implications for neurodegenerative disorders. *Science (New York, N.Y.)*, *287*(5456), 1265–1269. https://doi.org/10.1126/science.287.5456.1265

Masuda-Suzukake, M., Nonaka, T., Hosokawa, M., Kubo, M., Shimozawa, A., Akiyama, H., & Hasegawa, M. (2014). Pathological alpha-synuclein propagates through neural networks. Acta neuropathologica communications, 2, 88. https://doi.org/10.1186/s40478-014-0088-8

McClintock, T. S., Khan, N., Xie, C., & Martens, J. R. (2020). Maturation of the Olfactory Sensory Neuron and Its Cilia. Chemical senses, 45(9), 805–822. https://doi.org/10.1093/chemse/bjaa070

McCombs RM, Melnick MB, Brunschwig JP. Biophysical studies of vesicular stomatitis virus. *J Bacteriol*. 1966;91(2):803-812. doi:10.1128/jb.91.2.803-812.1966

Meade RM, Fairlie DP, Mason JM. Alpha-synuclein structure and Parkinson's disease – lessons and emerging principles. *Mol Neurodegeneration*. 2019;14(1):29. doi:10.1186/s13024-019-0329-1

Menezes, J. R., & Luskin, M. B. (1994). Expression of neuron-specific tubulin defines a novel population in the proliferative layers of the developing telencephalon. The Journal of neuroscience : the official journal of the Society for Neuroscience, 14(9), 5399–5416. https://doi.org/10.1523/JNEUROSCI.14-09-05399.1994

Miller IN, Cronin-Golomb A. Gender differences in Parkinson's disease: Clinical characteristics and cognition: Gender Differences in Parkinson's disease. *Mov Disord*. 2010;25(16):2695-2703. doi:10.1002/mds.23388

Mukaetova-Ladinska, E. B., Hurt, J., Jakes, R., Xuereb, J., Honer, W. G., & Wischik, C. M. (2000). Alpha-synuclein inclusions in Alzheimer and Lewy body diseases. *Journal of neuropathology and experimental neurology*, *59*(5), 408–417. https://doi.org/10.1093/jnen/59.5.408

Murphy, D. D., Rueter, S. M., Trojanowski, J. Q., & Lee, V. M. (2000). Synucleins are developmentally expressed, and alpha-synuclein regulates the size of the presynaptic vesicular pool in primary hippocampal neurons. *The Journal of neuroscience : the official journal of the Society for Neuroscience*, *20*(9), 3214–3220. https://doi.org/10.1523/JNEUROSCI.20-09-03214.2000

Nair, S., Michaelsen-Preusse, K., Finsterbusch, K., Stegemann-Koniszewski, S., Bruder, D., Grashoff, M., ... & Kröger, A. (2014). Interferon regulatory factor-1 protects from fatal neurotropic infection with vesicular stomatitis virus by specific inhibition of viral replication in neurons. *PLoS pathogens*, *10*(3), e1003999. https://doi.org/10.1371/journal.ppat.1003999

Okochi, M., Walter, J., Koyama, A., Nakajo, S., Baba, M., Iwatsubo, T., Meijer, L., Kahle, P. J., & Haass, C. (2000). Constitutive phosphorylation of the Parkinson's disease associated alpha-synuclein. The Journal of biological chemistry, 275(1), 390–397. https://doi.org/10.1074/jbc.275.1.390

Okuzumi, A., Kurosawa, M., Hatano, T., Takanashi, M., Nojiri, S., Fukuhara, T., Yamanaka, T., Miyazaki, H., Yoshinaga, S., Furukawa, Y., Shimogori, T., Hattori, N., & Nukina, N. (2018). Rapid dissemination of alpha-synuclein seeds through neural circuits in an in-vivo prion-like seeding experiment. Acta neuropathologica communications, 6(1), 96. https://doi.org/10.1186/s40478-018-0587-0

Olanow, C. W., Savolainen, M., Chu, Y., Halliday, G. M., & Kordower, J. H. (2019). Temporal evolution of microglia and α-synuclein accumulation following foetal grafting in Parkinson's disease. *Brain: a journal of neurology*, *142*(6), 1690–1700. https://doi.org/10.1093/brain/awz104

Omura, T., Kaneko, M., Okuma, Y., Matsubara, K., & Nomura, Y. (2013). Endoplasmic reticulum stress and Parkinson's disease: the role of HRD1 in averting apoptosis in neurodegenerative disease. *Oxidative medicine and cellular longevity*, *2013*, 239854. https://doi.org/10.1155/2013/239854

Oueslati A. Implication of Alpha-Synuclein Phosphorylation at S129 in Synucleinopathies: What Have We Learned in the Last Decade? *JPD*. 2016;6(1):39-51. doi:10.3233/JPD-160779

Oueslati, A., Fournier, M., & Lashuel, H. A. (2010). Role of post-translational modifications in modulating the structure, function and toxicity of alpha-synuclein: implications for Parkinson's disease pathogenesis and therapies. Progress in brain research, 183, 115–145. https://doi.org/10.1016/S0079-6123(10)83007-9

Outeiro TF, Koss DJ, Erskine D, et al. Dementia with Lewy bodies: an update and outlook. *Mol Neurodegeneration*. 2019;14(1):5. doi:10.1186/s13024-019-0306-8

Paiva, I., Pinho, R., Pavlou, M. A., Hennion, M., Wales, P., Schütz, A. L., Rajput, A., Szego, É. M., Kerimoglu, C., Gerhardt, E., Rego, A. C., Fischer, A., Bonn, S., & Outeiro, T. F. (2017). Sodium butyrate rescues dopaminergic cells from alpha-synuclein-induced transcriptional deregulation and DNA damage. Human molecular genetics, 26(12), 2231–2246. https://doi.org/10.1093/hmg/ddx114

Paleologou, K. E., & El-Agnaf, O. M. (2012). α-Synuclein aggregation and modulating factors. Sub-cellular biochemistry, 65, 109–164. https://doi.org/10.1007/978-94-007-5416-4_6

Pan, T., Kondo, S., Le, W., & Jankovic, J. (2008). The role of autophagy-lysosome pathway in neurodegeneration associated with Parkinson's disease. Brain : a journal of neurology, 131(Pt 8), 1969–1978. https://doi.org/10.1093/brain/awm318

Pandey MK, Burrow TA, Rani R, et al. Complement drives glucosylceramide accumulation and tissue inflammation in Gaucher disease. *Nature*. 2017;543(7643):108-112. doi:10.1038/nature21368

Pankiv, S., Clausen, T. H., Lamark, T., Brech, A., Bruun, J. A., Outzen, H., Øvervatn, A., Bjørkøy, G., & Johansen, T. (2007). p62/SQSTM1 binds directly to Atg8/LC3 to facilitate degradation of ubiquitinated protein aggregates by autophagy. *The Journal of biological chemistry*, *282*(33), 24131–24145. https://doi.org/10.1074/jbc.M702824200

Paleologou, K. E., & El-Agnaf, O. M. (2012). α-Synuclein aggregation and modulating factors. Sub-cellular biochemistry, 65, 109–164. https://doi.org/10.1007/978-94-007-5416-4_6

Peretto, P., Merighi, A., Fasolo, A., & Bonfanti, L. (1999). The subependymal layer in rodents: a site of structural plasticity and cell migration in the adult mammalian brain. Brain research bulletin, 49(4), 221–243. https://doi.org/10.1016/s0361-9230(99)00037-4

Park, S. C., Moon, J. C., Shin, S. Y., Son, H., Jung, Y. J., Kim, N. H., Kim, Y. M., Jang, M. K., & Lee, J. R. (2016). Functional characterization of alpha-synuclein protein with antimicrobial activity. Biochemical and biophysical research communications, 478(2), 924–928. https://doi.org/10.1016/j.bbrc.2016.08.052

Patterson, J. R., Polinski, N. K., Duffy, M. F., Kemp, C. J., Luk, K. C., Volpicelli-Daley, L. A., Kanaan, N. M., & Sortwell, C. E. (2019). Generation of Alpha-Synuclein Preformed Fibrils from Monomers and Use In Vivo. Journal of visualized experiments : JoVE, (148), 10.3791/59758. https://doi.org/10.3791/59758

Philippens, I. H. C. H. M., Böszörményi, K. P., Wubben, J. A. M., Fagrouch, Z. C., van Driel, N., Mayenburg, A. Q., Lozovagia, D., Roos, E., Schurink, B., Bugiani, M., Bontrop, R. E., Middeldorp, J., Bogers, W. M., de Geus-Oei, L. F., Langermans, J. A. M., Verschoor, E. J., Stammes, M. A., & Verstrepen, B. E. (2022). Brain Inflammation and Intracellular α-Synuclein Aggregates in Macaques after SARS-CoV-2 Infection. Viruses, 14(4), 776. https://doi.org/10.3390/v14040776

Pinho, R., Paiva, I., Jercic, K. G., Fonseca-Ornelas, L., Gerhardt, E., Fahlbusch, C., Garcia-Esparcia, P., Kerimoglu, C., Pavlou, M. A. S., Villar-Piqué, A., Szego, É., Lopes da Fonseca, T., Odoardi, F., Soeroes, S., Rego, A. C., Fischle, W., Schwamborn, J. C., Meyer, T., Kügler, S., Ferrer, I., … Outeiro, T. F. (2019). Nuclear localization and phosphorylation modulate pathological effects of alpha-synuclein. Human molecular genetics, 28(1), 31–50. https://doi.org/10.1093/hmg/ddy326

Polymeropoulos, M. H., Lavedan, C., Leroy, E., Ide, S. E., Dehejia, A., Dutra, A., Pike, B., Root, H., Rubenstein, J., Boyer, R., Stenroos, E. S., Chandrasekharappa, S., Athanassiadou, A., Papapetropoulos, T., Johnson, W. G., Lazzarini, A. M., Duvoisin, R. C., Di Iorio, G., Golbe, L. I., & Nussbaum, R. L. (1997). Mutation in the alpha-synuclein gene identified in families with Parkinson's disease. Science (New York, N.Y.), 276(5321), 2045–2047. https://doi.org/10.1126/science.276.5321.2045

Ransohoff, R. M., & Brown, M. A. (2012). Innate immunity in the central nervous system. *The Journal of clinical investigation*, *122*(4), 1164–1171. https://doi.org/10.1172/JCI58644

Reeve A, Simcox E, Turnbull D. Ageing and Parkinson's disease: Why is advancing age the biggest risk factor? *Ageing Research Reviews*. 2014;14:19-30. doi:10.1016/j.arr.2014.01.004

Rietdijk, C. D., Perez-Pardo, P., Garssen, J., van Wezel, R. J., & Kraneveld, A. D. (2017). Exploring Braak's Hypothesis of Parkinson's Disease. Frontiers in neurology, 8, 37. https://doi.org/10.3389/fneur.2017.00037

Rizek P, Kumar N, Jog MS. An update on the diagnosis and treatment of Parkinson disease. *CMAJ*. 2016;188(16):1157-1165. doi:10.1503/cmaj.151179

Ross, G. W., Petrovitch, H., Abbott, R. D., Tanner, C. M., Popper, J., Masaki, K., Launer, L., & White, L. R. (2008). Association of olfactory dysfunction with risk for future Parkinson's disease. *Annals of neurology*, *63*(2), 167–173. https://doi.org/10.1002/ana.21291

Sampson, T. R., Debelius, J. W., Thron, T., Janssen, S., Shastri, G. G., Ilhan, Z. E., Challis, C., Schretter, C. E., Rocha, S., Gradinaru, V., Chesselet, M. F., Keshavarzian, A., Shannon, K. M., Krajmalnik-Brown, R., Wittung-Stafshede, P., Knight, R., & Mazmanian, S. K. (2016). Gut Microbiota Regulate Motor Deficits and Neuroinflammation in a Model of Parkinson's Disease. Cell, 167(6), 1469–1480.e12. https://doi.org/10.1016/j.cell.2016.11.018

Samuels, E. R., & Szabadi, E. (2008). Functional neuroanatomy of the noradrenergic locus coeruleus: its roles in the regulation of arousal and autonomic function part I: principles of functional organisation. Current neuropharmacology, 6(3), 235–253. https://doi.org/10.2174/157015908785777229

Schaser, A. J., Osterberg, V. R., Dent, S. E., Stackhouse, T. L., Wakeham, C. M., Boutros, S. W., Weston, L. J., Owen, N., Weissman, T. A., Luna, E., Raber, J., Luk, K. C., McCullough, A. K., Woltjer, R. L., & Unni, V. K. (2019). Alpha-synuclein is a DNA binding protein that modulates DNA repair with implications for Lewy body disorders. Scientific reports, 9(1), 10919. https://doi.org/10.1038/s41598-019-47227-z

Scherer CF, O'Donnell V, Golde WT, Gregg D, Estes DM, Rodriguez LL. Vesicular stomatitis New Jersey virus (VSNJV) infects keratinocytes and is restricted to lesion sites and local lymph nodes in the bovine, a natural host. *Vet Res*. 2007;38(3):375-390. doi:10.1051/vetres:2007001

Schlossmacher, M. G., Tomlinson, J. J., Santos, G., Shutinoski, B., Brown, E. G., Manuel, D., & Mestre, T. (2017). Modelling idiopathic Parkinson disease as a complex illness can inform incidence rate in healthy adults: the PR EDIGT score. The European journal of neuroscience, 45(1), 175–191. https://doi.org/10.1111/ejn.13476

Schulz-Schaeffer W. J. (2010). The synaptic pathology of alpha-synuclein aggregation in dementia with Lewy bodies, Parkinson's disease and Parkinson's disease dementia. *Acta neuropathologica*, *120*(2), 131–143. https://doi.org/10.1007/s00401-010-0711-0

Selkoe D, Dettmer U, Luth E, Kim N, Newman A, Bartels T. Defining the native state of α-synuclein. *Neurodegener Dis*. 2014;13(2-3):114-117. doi:10.1159/000355516

Semerdzhiev, S. A., Fakhree, M. A. A., Segers-Nolten, I., Blum, C., & Claessens, M. M. A. E. (2022). Interactions between SARS-CoV-2 N-Protein and α-Synuclein Accelerate Amyloid Formation. ACS chemical neuroscience, 13(1), 143–150. https://doi.org/10.1021/acschemneuro.1c00666

Sengoku, R., Saito, Y., Ikemura, M., Hatsuta, H., Sakiyama, Y., Kanemaru, K., Arai, T., Sawabe, M., Tanaka, N., Mochizuki, H., Inoue, K., & Murayama, S. (2008). Incidence and extent of Lewy body-related alpha-synucleinopathy in aging human olfactory bulb. Journal of neuropathology and experimental neurology, 67(11), 1072–1083. https://doi.org/10.1097/NEN.0b013e31818b4126

Smeyne, R. J., Eells, J. B., Chatterjee, D., Byrne, M., Akula, S. M., Sriramula, S., O'Rourke, D. P., & Schmidt, P. (2022). COVID-19 Infection Enhances Susceptibility to Oxidative Stress-Induced Parkinsonism. Movement disorders : official journal of the Movement Disorder Society, 37(7), 1394–1404. https://doi.org/10.1002/mds.29116

Nair, S., Michaelsen-Preusse, K., Finsterbusch, K., Stegemann-Koniszewski, S., Bruder, D., Grashoff, M., Korte, M., Köster, M., Kalinke, U., Hauser, H., & Kröger, A. (2014). Interferon Regulatory Factor-1 Protects from Fatal Neurotropic Infection with Vesicular Stomatitis Virus by Specific Inhibition of Viral Replication in Neurons. PLoS Pathogens, 10(3), e1003999. https://doi.org/10.1371/journal.ppat.1003999

Siddiqui, A., Chinta, S. J., Mallajosyula, J. K., Rajagopolan, S., Hanson, I., Rane, A., Melov, S., & Andersen, J. K. (2012). Selective binding of nuclear alpha-synuclein to the PGC1alpha promoter under conditions of oxidative stress may contribute to losses in mitochondrial function: implications for Parkinson's disease. Free radical biology & medicine, 53(4), 993–1003. https://doi.org/10.1016/j.freeradbiomed.2012.05.024

Smeyne RJ, Noyce AJ, Byrne M, Savica R, Marras C. Infection and Risk of Parkinson's Disease. *J Parkinsons Dis*. 2021;11(1):31-43. doi:10.3233/JPD-202279

Sofroniew M. V. (2009). Molecular dissection of reactive astrogliosis and glial scar formation. Trends in neurosciences, 32(12), 638–647. https://doi.org/10.1016/j.tins.2009.08.002

Spencer, B., Valera, E., Rockenstein, E., Overk, C., Mante, M., Adame, A., Zago, W., Seubert, P., Barbour, R., Schenk, D., Games, D., Rissman, R. A., & Masliah, E. (2017). Anti-α-synuclein immunotherapy reduces α-synuclein propagation in the axon and degeneration in a combined viral vector and transgenic model of synucleinopathy. Acta neuropathologica communications, 5(1), 7. https://doi.org/10.1186/s40478-016-0410-8

Spillantini, M. G., Schmidt, M. L., Lee, V. M.-Y., Trojanowski, J. Q., Jakes, R., & Goedert, M. (1997). α-Synuclein in Lewy bodies. Nature, 388(6645), 839–840. https://doi.org/10.1038/42166

Spillantini, M. G., Crowther, R. A., Jakes, R., Hasegawa, M., & Goedert, M. (1998). alpha-Synuclein in filamentous inclusions of Lewy bodies from Parkinson's disease and dementia with lewy bodies. Proceedings of the National Academy of Sciences of the United States of America, 95(11), 6469–6473. https://doi.org/10.1073/pnas.95.11.6469

Stefanis L. α -Synuclein in Parkinson's Disease. *Cold Spring Harbor Perspectives in Medicine*. 2012;2(2):a009399-a009399. doi:10.1101/cshperspect.a009399

Stolzenberg, E., Berry, D., Yang, D., Lee, E. Y., Kroemer, A., Kaufman, S., Wong, G. C. L., Oppenheim, J. J., Sen, S., Fishbein, T., Bax, A., Harris, B., Barbut, D., & Zasloff, M. A. (2017). A Role for Neuronal Alpha-Synuclein in Gastrointestinal Immunity. Journal of innate immunity, 9(5), 456–463. https://doi.org/10.1159/000477990

Su, R., & Zhou, T. (2021). Alpha-Synuclein Induced Immune Cells Activation and Associated Therapy in Parkinson's Disease. *Frontiers in aging neuroscience*, *13*, 769506. https://doi.org/10.3389/fnagi.2021.769506

Taguchi, K., Watanabe, Y., Tsujimura, A., & Tanaka, M. (2019). Expression of α-synuclein is regulated in a neuronal cell type-dependent manner. *Anatomical science international*, *94*(1), 11–22. https://doi.org/10.1007/s12565-018-0464-8

Taguchi, K., Watanabe, Y., Tsujimura, A., Tatebe, H., Miyata, S., Tokuda, T., Mizuno, T., & Tanaka, M. (2014). Differential expression of alpha-synuclein in hippocampal neurons. *PloS one*, *9*(2), e89327. https://doi.org/10.1371/journal.pone.0089327

Tan E-K, Skipper LM. Pathogenic mutations in Parkinson disease. *Hum Mutat*. 2007;28(7):641-653. doi:10.1002/humu.20507

Tanji, K., Odagiri, S., Miki, Y., Maruyama, A., Nikaido, Y., Mimura, J., Mori, F., Warabi, E., Yanagawa, T., Ueno, S., Itoh, K., & Wakabayashi, K. (2015). p62 Deficiency Enhances α-Synuclein Pathology in Mice. Brain pathology (Zurich, Switzerland), 25(5), 552–564. https://doi.org/10.1111/bpa.12214

Tenreiro, S., Eckermann, K., & Outeiro, T. F. (2014). Protein phosphorylation in neurodegeneration: friend or foe?. Frontiers in molecular neuroscience, 7, 42. https://doi.org/10.3389/fnmol.2014.00042

Tofaris, G. K., Razzaq, A., Ghetti, B., Lilley, K. S., & Spillantini, M. G. (2003). Ubiquitination of alpha-synuclein in Lewy bodies is a pathological event not associated with impairment of proteasome function. The Journal of biological chemistry, 278(45), 44405–44411. https://doi.org/10.1074/jbc.M308041200

Tomlinson JJ, Shutinoski B, Dong L, et al. Holocranohistochemistry enables the visualization of α-synuclein expression in the murine olfactory system and discovery of its systemic anti-microbial effects. *J Neural Transm*. 2017;124(6):721-738. doi:10.1007/s00702-017-1726-7

Tulisiak, C. T., Mercado, G., Peelaerts, W., Brundin, L., & Brundin, P. (2019). Can infections trigger alpha-synucleinopathies? *Progress in molecular biology and translational science*, *168*, 299–322. https://doi.org/10.1016/bs.pmbts.2019.06.002

Twelves, D., Perkins, K. S., & Counsell, C. (2003). Systematic review of incidence studies of Parkinson's disease. *Movement disorders : official journal of the Movement Disorder Society*, *18*(1), 19–31. https://doi.org/10.1002/mds.10305

Ubeda-Bañon, I., Saiz-Sanchez, D., de la Rosa-Prieto, C., Argandoña-Palacios, L., Garcia-Muñozguren, S., & Martinez-Marcos, A. (2010). alpha-Synucleinopathy in the human olfactory system in Parkinson's disease: involvement of calcium-binding protein- and substance P-positive cells. Acta neuropathologica, 119(6), 723–735. https://doi.org/10.1007/s00401-010-0687-9

Ubeda-Bañon, I., Saiz-Sanchez, D., de la Rosa-Prieto, C., Mohedano-Moriano, A., Fradejas, N., Calvo, S., Argandoña-Palacios, L., Garcia-Muñozguren, S., & Martinez-Marcos, A. (2010). Staging of alpha-synuclein in the olfactory bulb in a model of Parkinson's disease: cell types involved. *Movement disorders : official journal of the Movement Disorder Society*, *25*(11), 1701–1707. https://doi.org/10.1002/mds.23197

Van Groen, T., & Wyss, J. M. (1990). Extrinsic projections from area CA1 of the rat hippocampus: olfactory, cortical, subcortical, and bilateral hippocampal formation projections. *The Journal of comparative neurology*, *302*(3), 515–528. https://doi.org/10.1002/cne.903020308

Vanderwolf C. H. (1992). Hippocampal activity, olfaction, and sniffing: an olfactory input to the dentate gyrus. *Brain research*, *593*(2), 197–208. https://doi.org/10.1016/0006-8993(92)91308-2

Vargas, K. J., Makani, S., Davis, T., Westphal, C. H., Castillo, P. E., & Chandra, S. S. (2014). Synucleins regulate the kinetics of synaptic vesicle endocytosis. *The Journal of neuroscience : the official journal of the Society for Neuroscience*, *34*(28), 9364–9376. https://doi.org/10.1523/JNEUROSCI.4787-13.2014

Visanji NP, Lang AE, Kovacs GG. Beyond the synucleinopathies: alpha synuclein as a driving force in neurodegenerative comorbidities. *Transl Neurodegener*. 2019;8(1):28. doi:10.1186/s40035-019-0172-x

Walker, P. J., Firth, C., Widen, S. G., Blasdell, K. R., Guzman, H., Wood, T. G., Paradkar, P. N., Holmes, E. C., Tesh, R. B., & Vasilakis, N. (2015). Evolution of genome size

and complexity in the rhabdoviridae. PLoS pathogens, 11(2), e1004664. https://doi.org/10.1371/journal.ppat.1004664

Walz, A., Omura, M., & Mombaerts, P. (2006). Development and topography of the lateral olfactory tract in the mouse: imaging by genetically encoded and injected fluorescent markers. Journal of neurobiology, 66(8), 835–846. https://doi.org/10.1002/neu.20266

Wang, H., Song, G., Chuang, H., Chiu, C., Abdelmaksoud, A., Ye, Y., & Zhao, L. (2018). Portrait of glial scar in neurological diseases. International journal of immunopathology and pharmacology, 31, 2058738418801406. https://doi.org/10.1177/2058738418801406

Wang, W., Nguyen, L. T., Burlak, C., Chegini, F., Guo, F., Chataway, T., Ju, S., Fisher, O. S., Miller, D. W., Datta, D., Wu, F., Wu, C. X., Landeru, A., Wells, J. A., Cookson, M. R., Boxer, M. B., Thomas, C. J., Gai, W. P., Ringe, D., Petsko, G. A., … Hoang, Q. Q. (2016). Caspase-1 causes truncation and aggregation of the Parkinson's disease-associated protein α-synuclein. Proceedings of the National Academy of Sciences of the United States of America, 113(34), 9587–9592. https://doi.org/10.1073/pnas.1610099113

Watanabe, Y., Tatebe, H., Taguchi, K., Endo, Y., Tokuda, T., Mizuno, T., Nakagawa, M., & Tanaka, M. (2012). p62/SQSTM1-dependent autophagy of Lewy body-like α-synuclein inclusions. PloS one, 7(12), e52868. https://doi.org/10.1371/journal.pone.0052868

Webb, J. L., Ravikumar, B., Atkins, J., Skepper, J. N., & Rubinsztein, D. C. (2003). Alpha-Synuclein is degraded by both autophagy and the proteasome. The Journal of biological chemistry, 278(27), 25009–25013. https://doi.org/10.1074/jbc.M300227200

Wilhelm, B. G., Mandad, S., Truckenbrodt, S., Kröhnert, K., Schäfer, C., Rammner, B., Koo, S. J., Claßen, G. A., Krauss, M., Haucke, V., Urlaub, H., & Rizzoli, S. O. (2014). Composition of isolated synaptic boutons reveals the amounts of vesicle trafficking proteins. *Science (New York, N.Y.)*, *344*(6187), 1023–1028. https://doi.org/10.1126/science.1252884

Wu, Z., Zhang, X., Huang, Z., & Ma, K. (2022). SARS-CoV-2 Proteins Interact with Alpha Synuclein and Induce Lewy Body-like Pathology In Vitro. International journal of molecular sciences, 23(6), 3394. https://doi.org/10.3390/ijms23063394

Yang, Z., & Wang, K. K. (2015). Glial fibrillary acidic protein: from intermediate filament assembly and gliosis to neurobiomarker. Trends in neurosciences, 38(6), 364–374. https://doi.org/10.1016/j.tins.2015.04.003

Yu, P., Wang, H., Katagiri, Y., & Geller, H. M. (2012). An in vitro model of reactive astrogliosis and its effect on neuronal growth. *Methods in molecular biology (Clifton, N.J.)*, *814*, 327–340. https://doi.org/10.1007/978-1-61779-452-0_21

Zarranz, J. J., Alegre, J., Gómez-Esteban, J. C., Lezcano, E., Ros, R., Ampuero, I., Vidal, L., Hoenicka, J., Rodriguez, O., Atarés, B., Llorens, V., Gomez Tortosa, E., del Ser, T., Muñoz,

D. G., & de Yebenes, J. G. (2004). The new mutation, E46K, of alpha-synuclein causes Parkinson and Lewy body dementia. Annals of neurology, 55(2), 164–173. https://doi.org/10.1002/ana.10795

Zhou C, Huang Y, Przedborski S. Oxidative Stress in Parkinson's Disease: A Mechanism of Pathogenic and Therapeutic Significance. Published online 2009:14.

Appendix

ID	Sex	Genotype	Treatment	Timepoint	Tissue Processing
F1-R	F	WT	VSV-GFP $3x10^3$ PFU	2DPI	IHC & IIF
F2-2R	F	WT	VSV-GFP $3x10^3$ PFU	2DPI	IHC & IIF
M1-195	M	WT	VSV-GFP $3x10^3$ PFU	2DPI	IHC & IIF
M2-194	M	WT	VSV-GFP $3x10^3$ PFU	2DPI	IHC & IIF
F1-182	F	WT	VSV-GFP $3x10^3$ PFU	4DPI	IHC & IIF
F2-183	F	WT	VSV-GFP $3x10^3$ PFU	4DPI	IHC & IIF
F3-185	F	WT	VSV-GFP $3x10^3$ PFU	4DPI	IHC & IIF
M1-230	M	WT	VSV-GFP $3x10^3$ PFU	4DPI	IHC & IIF
F1-235	F	WT	VSV-GFP $3x10^3$ PFU	6DPI	IHC & IIF
F2-189	F	WT	VSV-GFP $3x10^3$ PFU	6DPI	IHC & IIF
M1-2LR	M	WT	VSV-GFP $3x10^3$ PFU	6DPI	IHC & IIF
M2-LR	M	WT	VSV-GFP $3x10^3$ PFU	6DPI	IHC & IIF
F1-236	F	WT	VSV-GFP $3x10^3$ PFU	6DPI	Viral Titering & Immunoblotting
F2-199	F	WT	VSV-GFP $3x10^3$ PFU	6DPI	Viral Titering & Immunoblotting
F3-237	F	WT	VSV-GFP $3x10^3$ PFU	6DPI	Viral Titering & Immunoblotting
M1-LR	M	WT	VSV-GFP $3x10^3$ PFU	6DPI	Viral Titering & Immunoblotting
F1-202	F	WT	VSV-GFP $3x10^3$ PFU	10DPI	IHC & IIF
F2-209	F	WT	VSV-GFP $3x10^3$ PFU	10DPI	IHC & IIF
F3-203	F	WT	VSV-GFP $3x10^3$ PFU	10DPI	IHC & IIF
M1	M	WT	VSV-GFP $3x10^3$ PFU	10DPI	IHC & IIF
M2-234	M	WT	VSV-GFP $3x10^3$ PFU	10DPI	IHC & IIF
F1-R	F	WT	PBS	Mock	IHC & IIF
F2-LR	F	WT	PBS	Mock	IHC & IIF
M1-131	M	WT	PBS	Mock	IHC & IIF
M2-189	M	WT	PBS	Mock	IHC & IIF
Snca-KO	F	*Snca*-KO	N/A	N/A	IHC & IIF

Table 2: A Comprehensive Descriptor List of Mice Constituting the Main Cohort Including Animal ID, Sex, Treatment Plan, Sacrifice Timepoint, and Subsequent Processing of Tissue. F: Female; M: Male; WT: Wildtype; DPI: Days-post-inoculation; IHC: Immunohistochemistry; IIF: Indirect Immunofluorescence.

ID	Sex	Genotype	Treatment	Timepoint	Region	Tissue Processing
034 R	F	WT	VSV $3x10^3$ PFU	2DPI	OB & HB	Viral Titering
034 L	F	WT	VSV $3x10^3$ PFU	2DPI	OB & HB	Viral Titering
034 LR	F	WT	VSV $3x10^3$ PFU	2DPI	OB & HB	Viral Titering
177 L	F	WT	VSV $3x10^3$ PFU	2DPI	Hemi	Viral Titering
177 LR	F	WT	VSV $3x10^3$ PFU	2DPI	Hemi	Viral Titering
310 R	F	WT	VSV $3x10^3$ PFU	2DPI	Hemi	Viral Titering
310 L	F	WT	VSV $3x10^3$ PFU	2DPI	Hemi	Viral Titering
310 LR	F	WT	VSV $3x10^3$ PFU	2DPI	Hemi	Viral Titering
521 R	F	WT	VSV $3x10^3$ PFU	2DPI	Hemi	Viral Titering
521 L	F	WT	VSV $3x10^3$ PFU	2DPI	Hemi	Viral Titering
522 2R	F	WT	VSV $3x10^3$ PFU	2DPI	Hemi	Viral Titering
522 2L	F	WT	VSV $3x10^3$ PFU	2DPI	Hemi	Viral Titering
522 LR	F	WT	VSV $3x10^3$ PFU	2DPI	Hemi	Viral Titering

Table 3: A Comprehensive Descriptor List of Mice Constituting the Symmetry Cohort Including Animal ID, Sex, Treatment Plan, Sacrifice Timepoint, and Subsequent Processing of Tissue. F: Female; M: Male; WT: Wildtype; DPI: Days-post-inoculation; IHC: Immunohistochemistry; IIF: Indirect Immunofluorescence. OB: Olfactory Bulb; HB: Hindbrain; Hemi: Hemibrain.

Sample	Organ	Tube (mg)	Tube + Organ (mg)	Organ (mg)	Dilution	PBS (uL)
F1 VSV-GFP HB1	Hemibrain	1533.7	1757.3	223.6	1:3 (x2 PBS)	447.2
F1 VSV-GFP HB2	Hemibrain	1533.8	1831.3	297.5	1:3 (x2 PBS)	595
F2 VSV-GFP HB1	Hemibrain	1537.8	1883.2	345.4	1:3 (x2 PBS)	690.8
F2 VSV-GFP HB2	Hemibrain	1540	1725.1	185.1	1:3 (x2 PBS)	370.2
F3 VSV-GFP HB1	Hemibrain	1536.8	1790.7	253.9	1:3 (x2 PBS)	507.8
F3 VSV-GFP HB2	Hemibrain	1538.5	1788.5	250	1:3 (x2 PBS)	500
M1 VSV-GFP HB1	Hemibrain	1534.8	1814.9	280.1	1:3 (x2 PBS)	560.2
M1 VSV-GFP HB2	Hemibrain	1535.6	1780.2	244.6	1:3 (x2 PBS)	489.2
F1 VSV-GFP OB	Olfactory bulb	1537.8	1556	18.2	1:6 (x5 PBS)	91
F2 VSV-GFP OB	Olfactory bulb	1546	1565.2	19.2	1:6 (x5 PBS)	96
F3 VSV-GFP OB	Olfactory bulb	1534.5	1568.5	34	1:6 (x5 PBS)	170
M1 VSV-GFP OB	Olfactory bulb	1540.6	1565.7	25.1	1:6 (x5 PBS)	125.5

Table 4: Measured Weights of Hemibrains and Olfactory Bulbs of 6DPI Mice from the Main Cohort and the Required Dilutions of PBS for Homogenization.

Disease Score	Disease Phenotype
1	Percolated fur but no detectable behavioral differences compared to untreated mice
2	Percolated fur and a huddle reflex but are still active
3	Less active and are relatively passive when handled; hindlimb paralysis
4	Inactive mice that exhibit only limited response when handled = endpoint
5	Moribund mice

Table 5: The Scoring Criterion and Assessment Used to Monitor and Grade the Sickness in Animals Infected with VSV-GFP, Approved by the University of Ottawa Animal Care and Veterinary Services Committee.

Antibody	Provider	Species/ Clonality	Cat #	Application/ Dilution
Anti-α-synuclein-1 (Syn-1)	BD Biosciences	Mouse/	610787	IHC: 1:3000 IIF: 1:250 WB: 1:3000
Anti-α-synuclein (HSA4)	Non-commercial (Recombinant human α-synuclein)	Rabbit/ Polyclonal	N/A	IIF: 1:250
Anti-α-synuclein (LB509)	Zymed; ThermoFisher	Mouse/ Monoclonal	18-0212	IHC: 1:1000
Anti-pS129-α-synuclein (EP1536Y)	Abcam	Rabbit/ Monoclonal	AB51253	IHC: 1:2000 IIF: 1:1000
Anti-aggregated-α-synuclein (MJFR14642)	Abcam	Rabbit/ Monoclonal	AB209538	IHC: 1:10000 IIF: 1:4000
Anti-p62/ SQSTM1	Proteintech Group	Rabbit/ Poly	18420-1-AP	IIF: 1:1000
Anti-GFP	Santa Cruz Biotech	Mouse/ Monoclonal	Sc-9996	IHC: 1:4000 IIF: 1:250
Anti-GFP	Invitrogen	Rabbit/ Monoclonal	A11122	IHC: 1:4000 IIF: 1:250
Anti-VSV	Dr. Earl Brown	Rabbit/ Polyclonal	N/A	IHC: 1:6000 IIF: 1:1000 WB/ 1:6000
Anti-IBA1	Wako	Rabbit/ Polyclonal	019-19741	IHC: 1:2000
Anti-GFAP	Dako	Rabbit/ Polyclonal	Z0334	IHC: 1:4000
Anti-NeuN	Millipore	Mouse/ Monoclonal	MAB377	IIF: 1:500
Anti-OMP	Wako	Goat/ Polyclonal	544-10001	IIF: 1:500
Anti- B-tubulin III	Abcam	Rabbit/ Monoclonal	AB215073	IIF: 1:500

Table 6: Summary of Suitable Primary Antibodies Used to Monitor Microglia, Astrocytes, and Native and Pathological α-Synuclein in Immunohistological Experiments and Western Immunoblotting.

Antibody	Provider	Form	Cat #	Dilution
Goat anti-mouse	Vector Labs	Biotinylated	BA-9200	IHC: 1:225
Goat anti-rabbit	Vector Labs	Biotinylated	BA-1000	IHC: 1:225
Goat anti-mouse	Invitrogen	AlexaFlour 488-conjugated AlexaFlour 594-conjugated	A11029 A11058	IIF: 1:200
Goat anti-rabbit	Invitrogen	AlexaFlour 488-conjugated AlexaFlour 594-conjugated	A11008 A11012	IIF: 1:200
Goat anti-mouse	GE Healthcare	ECL Horseradish-peroxidase-conjugated	NA931V	WB: 1:10000
Goat anti-rabbit	Invitrogen	ECL Horseradish-peroxidase-conjugated	31460	WB: 1:10000

Table 7: Summary of Appropriate Secondary Antibodies, either Biotinylated, Conjugated to a Fluorophore, or Horseradish Peroxidase, Coupled with Primary Antibodies to Enable the Visualization of Target Antigens in Immunohistological Experiments and Western Immunoblotting.

Step-by-Step Demonstration of Quantification Criterion of Glial Phenotypical Parameters in Scanned Mouse Skull Sections:

- Start by choosing the desired file and pick the right "Series" to access the scan: the Bio-Formats plugin will load the selected file in an import window with multiple options for viewing, to which "view stack with: Hyperstack" is selected along with "display OME-XML metadata

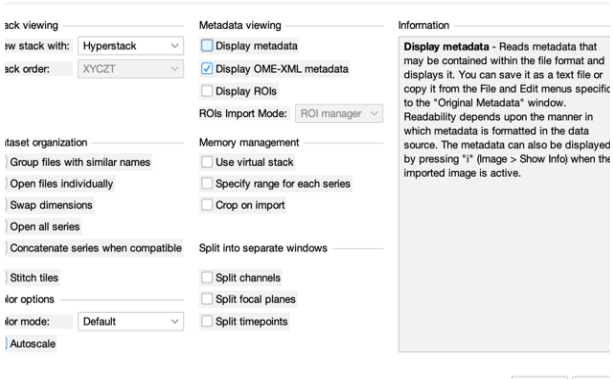

- This opens the scanned image in different "Series": these series are numbered and are of different resolutions, with the first one being of the highest resolution and hence the highest number of pixels. Since the images can be of enormous sizes – upwards of 1GB in some cases – putting a heavy strain on the memory of the device use, Fiji (ImageJ 2) version 2.14.0 offers the possibility of loading these files in lower resolutions for easier and smoother manipulation. On my machine, all scanned files were accessed via "Series 3".

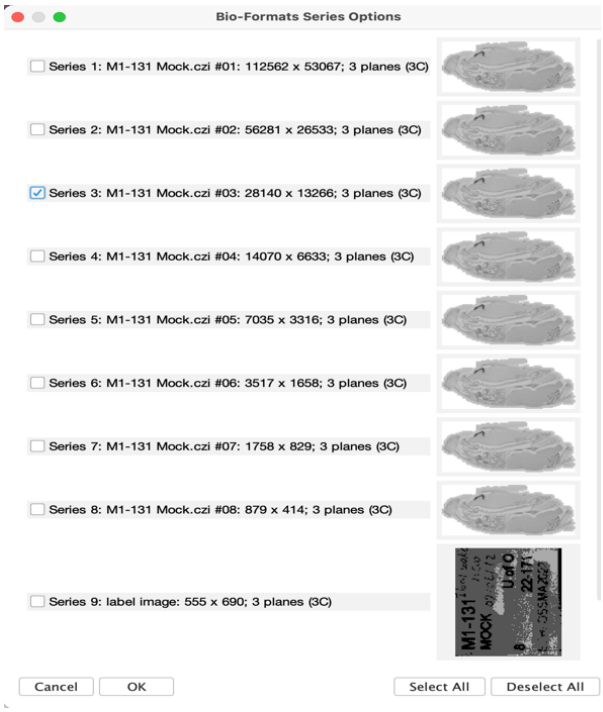

- Once loaded**,** start by cropping the image as needed: this is optional as processing the entire image is theoretically possible, but doing so renders subsequent processing times longer and makes of a less fluid experience.

- Convert the image to RGB: this is necessary to for the software to be able to separate different colors, or more precisely, dyes in the case of staining, for an image loads initially in an 8-bit format.

- Separate the different stains in each image using color deconvolution: this technique is useful to unmix dyes in images where colors mix subtractively (i.e., bright field microscope using histological stains). For my brightfield sections, DAB is used to detect the ABC (Avidin-Biotinylated enzyme Complex), which in turn binds to the biotinylated secondary antibody and gives a brownish-colored deposit corresponding to specific staining. This is subsequently counterstained with H&E before dehydration and mounting. Thus, the filter used in this step to separate stains is titled “H&E and DAB”.

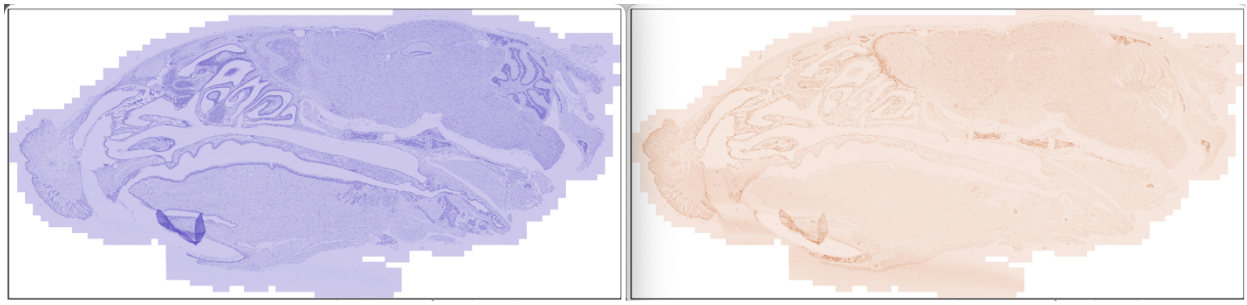

- Select the area you would like to quantify and/ or count from: simply draw a line going over the boundaries of an area of interest forming an enclosed geometric shape. The drawn line does not have to be exactly aligned with the boundaries of the particular structure as the differences in area (pixel^2) selected and number of particles will be standardized across slides accounted for in the area percent calculation step.

- Subtract the background: the pixel value was set to 50 for all; this helps with depressing background staining so as not to interfere with an accurate count and measurement of particles of interest.

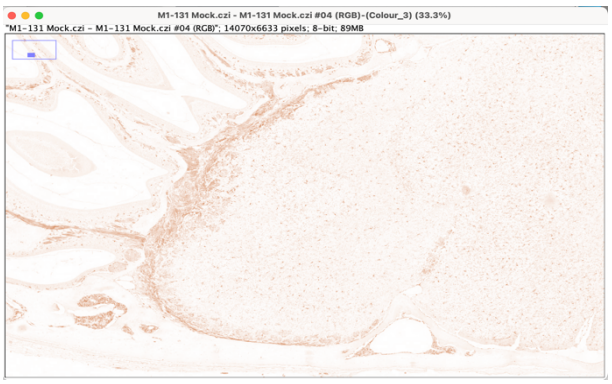

- Set the threshold: this is extremely important as it will be detrimental in picking up specific signal while omitting background as much as possible but also not risking losing specificity. For the sake of consistency, the auto threshold function was used and the MaxEntropy filter was picked analyzing both microglia and astrocytes. This allows for the automatic choosing of a threshold value based on the variable intensity of staining in each section and thus comparable results

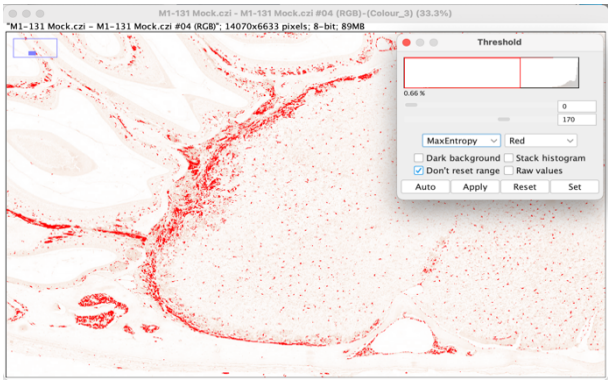

- Set the measurements: configure the measurements that are deemed helpful for the components or signal of interest – explained above for microglia and astrocytes – before proceeding to analyze particles.

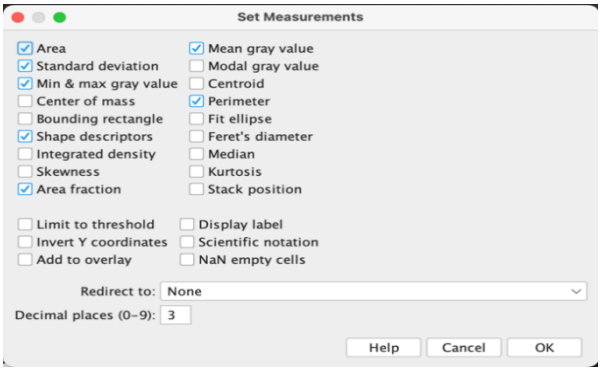

- Analyze particles: the size in pixels^2 was set to: 40 – 250 for both microglia and astrocytes. This value range was chosen after a careful process of trial-and-error to include specific immune cell staining but also exclude unspecific/ background signal while limiting the noise in the greyscale that interferes with accurate signal. Also, the body size of microglia and astrocytes reported in literature happens to fall in that range after the conversion to microns – see last section of this protocol for equation to convert from pixels to microns. The “exclude on edges” option was selected to exclude any possible particle count where the lines forming the boundaries of the selected area lie.

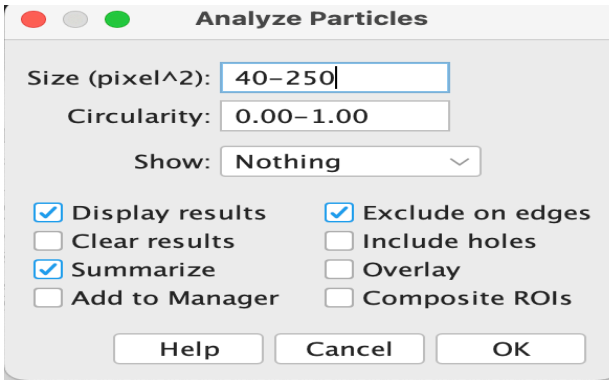

- Save the results window along with the detailed description chart showing the individual values of specified parameters onto the device and use for subsequent quantification and plotting.

- Find the scale: the scale should automatically be recorded in the image's database. Check if that is the case from the text at the top of the image window – the text displays the dimensions of the image. If the image is calibrated, will see dimensions in both pixels and microns.

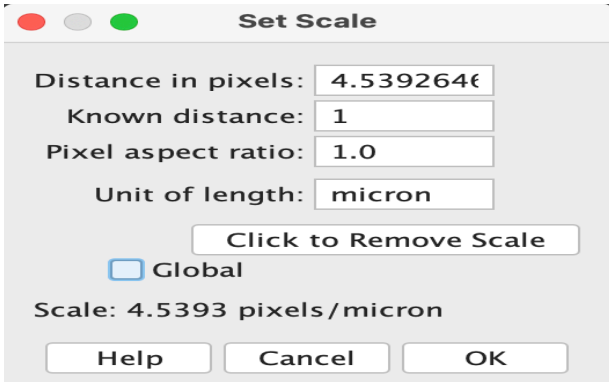

- Determine the real value of each pixel in the scanned image: for this, the metadata will need to be revealed. To do so, open the desired file from scratch and skip any selection required of "Series" upon bypassing the hyper stack. This will unveil the metadata included with the scan but only for Series 1. To figure out the real-life value of each pixel in Series 3 in microns, the calculation in the Excel sheet below was performed:

  For 20x scans, from the metadata, 1 pixel = 0. 2203 um for Series 1.

112562	0.2203	Conversion = 0.2203	Pixels =	4.539264639	to	1	Micron
28140	0.881215657	Conversion = 0.881215657	Pixels =	1.134795996	to	1	Micron

  Where 112562 pixels (Series 1) / 28140 pixels (Series 3) = 4.000071073205402.

  So, while each pixel is 0.2203 microns in Series 1, each pixel in Series 3 is 0.2203 x 4.000071073205402 = 0.881215657 microns. This makes sense considering that there is

less overall pixel in Series 3 (an essentially lower resolution image) compared to Series 1, and so pixels occupy larger areas in Series 3 to compensate for the lower pixel number.

Use this conversion – Series 1 and Series 3 exclusive - to determine the real size of measured particles in microns in Series 3. For example, if the particle size is 50 pixel^2, the real-life micron measurement equals 50 x 0.881215657 = 44.06078285 microns.

Selection Level	Size of Selection	Description of Selection
Level 1	544.173 pixel^2	Selection includes an infected glomerulus only indicated by positive anti-VSV and anti-GFP staining
Level 2	1876.52 pixel^2	Selection includes infected glomerulus selected in level 1 in addition to two immediate neighboring glomeruli
Level 3	18323.912 pixel^2	Selection includes glomeruli previously selected in level 2 in addition to multiple more in the glomerular layer (GL) and expands to include the external plexiform layer (EPL)
Level 4	95241.673 pixel^2	Selection builds on level 3 by including more glomeruli farther out from the infected glomerulus chosen initially for level 1 and expands deeper into the olfactory bulb to include the mitral cell layer (ML) and the internal plexiform layer (IPL)

Table 8: Descriptors of Different Sectioning Levels Selected to Reveal Possible Variations in Measured Parameters of Proximal and Distant Microglia.